

**MACROSCOPIC INVESTIGATIONS OF A  
MICROWAVE GENERATED PLASMA**

**By**

**Duane Weldon Dinkel**

**A THESIS**

**Submitted to**

**Michigan State University**

**in partial fulfillment of the requirements**

**for the degree of**

**MASTER OF SCIENCE**

**Department of Chemical Engineering**

**1991**

# ABSTRACT

## MACROSCOPIC INVESTIGATIONS OF A MICROWAVE GENERATED PLASMA

By

Duane Weldon Dinkel

The Microwave Electrothermal Thruster (MET) has been demonstrated, both theoretically and experimentally, to be a viable substitute for chemical propulsion and to possess lifetime advantages over systems where electrodes are in contact with the propellant. A specially designed resonance cavity transfers energy from the microwave power source to the electrons in the propellant. The electromagnetic field accelerates these electrons to sufficient energies for ionization to occur. The plasma thermalizes the propellant, which undergoes thermodynamic expansion and produces the desired thrust.

The goal of this work is to further the development of the MET concept through assessing the macroscopic influences the plasma has on its surroundings and vice versa. The general diagnostics used include

photographic, calorimetric, and spectroscopic measurements of pure gases and binary mixtures using the  $TM_{012}$  mode in the resonant cavity. The data from these investigations are consolidated in a model that describes the velocity and temperature distributions around and downstream of the plasma. The advantage of modeling these macroscopic properties over microscopic phenomena is that the former can be evaluated experimentally to better assess the modeling assumptions. This model can be used to predict nozzle performance and improve thruster designs.

**With the most sincere appreciation, I dedicate this thesis to  
my wife, Kristin, who has graciously endured this experience with me.**

## **Acknowledgements**

**"Science is nothing but developed perception, interpreted intent, common sense rounded out and minutely articulated."**

**[George Santayana: *The Life Of Reason*: "Reason in Science" V]**

In helping to develop the "perception", the author wishes to thank Dr. Martin C. Hawley for providing an excellent research environment. Acknowledgement is also extended to the folks at NASA - Lewis Research Center, particularly Dr. John Power, for his assistance and support on the project. Additional recognition is given to Dr. Jeff Hopwood, for his patient replies to the many questions asked at most inopportune times, to Scott Haraburda, for providing a solid foundation to build upon, and to Dr. Ted Tsakumis, for his stimulating philosophies and guidance. The author is most of all grateful to Weldon and Hazel Dinkel for their many significant contributions to this project.

Portions of this work was supported by the National Aeronautics and Space Administration - Lewis Research Center.

# TABLE OF CONTENTS

<b>LIST OF TABLES</b> .....	<b>viii</b>
<b>LIST OF FIGURES</b> .....	<b>ix</b>
<b>CHAPTER 1 <i>Introduction</i></b> .....	<b>1</b>
<b>1.1 Research Summary</b> .....	<b>1</b>
<b>1.2 Motivation for Plasma Diagnostic Research</b> .....	<b>2</b>
<b>1.3 Research Objectives</b> .....	<b>4</b>
<b>CHAPTER 2 <i>Theory</i></b> .....	<b>7</b>
<b>2.1 Introduction</b> .....	<b>7</b>
<b>2.2 Equilibrium in Gases</b> .....	<b>10</b>
<b>2.3 Mean Free Path</b> .....	<b>12</b>
<b>2.4 Validity of the Ideal Gas Law</b> .....	<b>13</b>
<b>2.5 Microscopic Plasma Phenomena</b> .....	<b>16</b>
<b>2.6 Microscopic Mass Balances</b> .....	<b>19</b>
<b>2.7 System Thermodynamics</b> .....	<b>23</b>
2.7.1 Chemical Potential .....	<b>26</b>
2.7.2 Saha Equation .....	<b>28</b>
2.7.3 Degree of Ionization .....	<b>32</b>
<b>2.8 Electromagnetic Theory</b> .....	<b>38</b>
<b>CHAPTER 3 <i>Plasma Diagnostic System</i></b> .....	<b>41</b>
<b>3.1 Introduction</b> .....	<b>41</b>
<b>3.2 Microwave Source</b> .....	<b>45</b>
<b>3.3 Gas Flow System</b> .....	<b>47</b>
<b>3.4 Plasma Containment Assembly</b> .....	<b>48</b>
<b>3.5 Microwave Cavity</b> .....	<b>50</b>
<b>3.6 Spectroscopic System</b> .....	<b>54</b>
<b>CHAPTER 4 <i>Plasma Dimensional and Quality Analysis</i></b> .....	<b>61</b>
<b>4.1 Photographic Method of Analysis</b> .....	<b>61</b>
<b>4.2 Plasma Overall Volume</b> .....	<b>62</b>
4.2.1 Pressure Dependence .....	<b>63</b>
4.2.2 Gas Flow Dependence .....	<b>66</b>
4.2.3 Composition Dependence .....	<b>68</b>
4.2.4 Power Dependence .....	<b>71</b>

4.3	Gas-Surface Interactions . . . . .	71
CHAPTER 5	<i>Calorimetric Investigations</i> . . . . .	77
5.1	Macroscopic Energy Balance . . . . .	77
5.2	Energy Distribution . . . . .	80
5.2.1	Pressure Dependence . . . . .	81
5.2.2	Gas Flow Rate Dependence . . . . .	81
5.2.3	Composition Dependence . . . . .	84
CHAPTER 6	<i>Spectroscopic Investigations</i> . . . . .	86
6.1	Introduction . . . . .	86
6.2	Theory . . . . .	87
6.2.1	Spectroscopic Temperature Measurements . . . . .	87
6.2.2	Degrees of Freedom . . . . .	90
6.3	Methods of Analysis . . . . .	96
6.3.1	Single Atomic Line Method . . . . .	96
6.3.2	Two-line Radiance Ratio Method . . . . .	99
6.3.3	Atomic Boltzmann Plot Method . . . . .	100
6.4	Species Concentrations . . . . .	101
6.5	Advanced Methods of Analysis . . . . .	102
6.5.1	Laser-Induced Fluorescence Spectroscopy . . . . .	102
6.5.2	Actinometry . . . . .	104
6.6	Electronic Temperatures . . . . .	106
6.7	Concentrations of Species . . . . .	116
6.8	Conclusions . . . . .	118
CHAPTER 7	<i>Model Formulation</i> . . . . .	123
7.1	Introduction . . . . .	123
7.2	Assumptions . . . . .	125
7.3	Characterizing Dominant Forces . . . . .	128
7.4	Model A - Penetratable Plasma with Plugflow . . . . .	130
7.5	Model B - Penetratable Plasma with Parabolic Velocity Profile . . . . .	134
7.6	Model C - Impenetratable Plasma with No-slip Boundary Conditions . . . . .	137
7.7	Model D - Impenetratable Plasma with Slip Conditions Around the Plasma . . . . .	142
7.8	Summary . . . . .	145
CHAPTER 8	<i>Summary and Conclusions</i> . . . . .	149
CHAPTER 9	<i>Recommendations for Future Research</i> . . . . .	155
REFERENCES	. . . . .	159

## LIST OF TABLES

<b>Table 3.1</b>	<b>Tungsten Calibration Data for Spectral Response . . . . .</b>	<b>60</b>
<b>Table 4.1</b>	<b>Plasma Volume Conditions . . . . .</b>	<b>65</b>
<b>Table 4.2</b>	<b>Inner and Overall Volumes and Color Transformations for Helium/Nitrogen Plasma . . . . .</b>	<b>70</b>
<b>Table 5.1</b>	<b>Calorimetric Conditions . . . . .</b>	<b>80</b>
<b>Table 6.1</b>	<b>Spectroscopic Conditions . . . . .</b>	<b>106</b>
<b>Table 6.2</b>	<b>Observed Transitions . . . . .</b>	<b>107</b>
<b>Table 6.3</b>	<b>Spectroscopic Data for Helium . . . . .</b>	<b>109</b>
<b>Table 7.1</b>	<b>Helium Plasma Dimensions with Pressure . . . . .</b>	<b>124</b>
<b>Table 7.2</b>	<b>Reynolds Number at Varying Conditions . . . . .</b>	<b>129</b>
<b>Table 8.1</b>	<b>Experimental Conditions Used to Evaluate LTE . . . . .</b>	<b>152</b>

## LIST OF FIGURES

<b>Figure 1.1</b>	<b>Proposed MET Concept on Board a Satellite . . . . .</b>	<b>5</b>
<b>Figure 2.1</b>	<b>Mean Free Path as a Function of Pressure . . . . .</b>	<b>14</b>
<b>Figure 2.2</b>	<b>Volumes Obtained by Ideal Gas Law Compared to those Obtained by Peng-Robinson Equation of State . . . . .</b>	<b>17</b>
<b>Figure 2.3</b>	<b>Relative Plasma Deformations Caused by Changes in Pressure . . . . .</b>	<b>20</b>
<b>Figure 2.4</b>	<b>Thermodynamic System for the MET . . . . .</b>	<b>22</b>
<b>Figure 2.5</b>	<b>Helium Plasma Degree of Ionization Obtained from the Saha Equation as Functions of Pressure and Temperature . . . . .</b>	<b>35</b>
<b>Figure 2.6</b>	<b>Helium Plasma Molar Constituents at 76 mTorr Obtained from the Saha Equation . . . . .</b>	<b>36</b>
<b>Figure 3.1</b>	<b>Experimental Configuration . . . . .</b>	<b>42</b>
<b>Figure 3.2</b>	<b>Microwave Source and Peripherals . . . . .</b>	<b>46</b>
<b>Figure 3.3</b>	<b>Plasma Containment Assembly . . . . .</b>	<b>49</b>
<b>Figure 3.4</b>	<b>Top Collar Design . . . . .</b>	<b>51</b>
<b>Figure 3.5</b>	<b>Bottom Collar Design . . . . .</b>	<b>52</b>
<b>Figure 3.6</b>	<b>Microwave Resonant Cavity . . . . .</b>	<b>53</b>
<b>Figure 3.7</b>	<b>Fiber Optic Cable with Terminations . . . . .</b>	<b>55</b>
<b>Figure 3.8</b>	<b>Helium Spectra Obtained With and Without the Fiber Optic Cable . . . . .</b>	<b>57</b>
<b>Figure 3.9</b>	<b>Spectroscopic System . . . . .</b>	<b>58</b>



<b>Figure 4.1</b>	<b>Overall Plasma Volumes for Helium, Nitrogen, and Mixture as a Function of Pressure . . . . .</b>	<b>64</b>
<b>Figure 4.2</b>	<b>Overall Plasma Volumes for Helium, Nitrogen, and Mixture as a Function of Gas Flow Rate . . . . .</b>	<b>67</b>
<b>Figure 4.3</b>	<b>Overall Plasma Volumes as a Function of Composition (by volume) . . . . .</b>	<b>69</b>
<b>Figure 4.4</b>	<b>Overall Plasma Volume for a Helium Plasma at 200 and 300 W as a Function of Gas Flow Rate . . . . .</b>	<b>72</b>
<b>Figure 4.5</b>	<b>Comparison of Wall Recombination Rate Equations for a Helium Plasma as a Function of Gas and Wall Temperatures . . . . .</b>	<b>75</b>
<b>Figure 5.1</b>	<b>Plasma Energy Absorption for Helium, Nitrogen, and Mixture as a Function of Pressure . . . . .</b>	<b>82</b>
<b>Figure 5.2</b>	<b>Plasma Energy Absorption for Helium, Nitrogen, and Mixture as a Function of Gas Flow Rate . . . . .</b>	<b>83</b>
<b>Figure 5.3</b>	<b>Plasma Energy Absorption as a Function of Composition (by volume) . . . . .</b>	<b>85</b>
<b>Figure 6.1</b>	<b>Atomic Energy Levels . . . . .</b>	<b>91</b>
<b>Figure 6.2</b>	<b>Potential Energy Curves for Diatomic Species . . . . .</b>	<b>93</b>
<b>Figure 6.3</b>	<b>Degrees of Freedom for Diatomic Species . . . . .</b>	<b>95</b>
<b>Figure 6.4</b>	<b>Energy Level Diagram for Helium . . . . .</b>	<b>108</b>
<b>Figure 6.5</b>	<b>Helium Plasma <math>T_e</math> as a Function of Pressure . . . . .</b>	<b>111</b>
<b>Figure 6.6</b>	<b>Typical Graph Generated for Single-line Method . . . . .</b>	<b>112</b>
<b>Figure 6.7</b>	<b>Helium Plasma <math>T_e</math> as a Function of Gas Flow Rate . . . . .</b>	<b>113</b>
<b>Figure 6.8</b>	<b>Argon Plasma <math>T_e</math> as a Function of Gas Flow Rate . . . . .</b>	<b>115</b>
<b>Figure 6.9</b>	<b>Helium Plasma Neutral Atom Density as a Function of Gas Flow Rate. . . . .</b>	<b>117</b>



<b>Figure 6.10</b>	<b>Helium Plasma Degree of Ionization as a Function of Gas Flow Rate - number 1 . . . . .</b>	<b>119</b>
<b>Figure 6.11</b>	<b>Helium Plasma Degree of Ionization as a Function of Gas Flow Rate - number 2 . . . . .</b>	<b>120</b>
<b>Figure 7.1</b>	<b>Prandtl Number of Helium with Temperature . . . . .</b>	<b>127</b>
<b>Figure 7.2</b>	<b>Plugflow through Plasma . . . . .</b>	<b>130</b>
<b>Figure 7.3</b>	<b>Parabolic Velocity Distribution through Plasma . . . . .</b>	<b>134</b>
<b>Figure 7.4</b>	<b>Parabolic Velocity Profile Around Annulus, No-slip Conditions at <math>R_0</math> and <math>R_i</math> . . . . .</b>	<b>138</b>
<b>Figure 7.5</b>	<b>Theoretical Pressure Drop for Model C . . . . .</b>	<b>140</b>
<b>Figure 7.6</b>	<b>No-slip along Containment Walls, Slip along Plasma . . . . .</b>	<b>143</b>
<b>Figure 7.7</b>	<b>Theoretical Pressure Drop for Model D . . . . .</b>	<b>144</b>
<b>Figure 7.8</b>	<b>Comparison of <math>\Delta P</math> Obtained for Models C and D . . . . .</b>	<b>146</b>
<b>Figure 7.9</b>	<b>Final Modeled Region. . . . .</b>	<b>147</b>



# CHAPTER 1

---

## *Introduction*

### **1.1 Research Summary**

**The plasma diagnostic research at MSU is a single dimension of a group effort oriented towards realizing and optimizing microwave generated plasma technology for practical and economic industrial use. Though each application may be specifically unique, they are all based on the fundamentals of plasma behavior. The diagnostics of these fundamentals utilize the latest instrumentation and knowledge to evaluate the chemistry, physics, thermodynamics, electrodynamics, and transport properties within the plasma. Some of these methods are used to evaluate the overall system, such as the efficient coupling of energy from the microwave source to the plasma and energy distribution within the cavity. Other methods are used to study the microscopic phenomena that occur within the plasma system, such as surface reactions and collisional processes between species.**

## 1.2 Motivation for Plasma Diagnostic Research

Historically, plasmas have maintained a low profile as a phenomenon solely of academic interest, primarily researched by the physicist, who noted the many disciplines of physics that are combined into the single study of plasmas. In fact, low-density, high-pressure plasmas, where quantum effects are negligible, provide almost all the elements of classical physics<sup>1</sup>. Since the early sixties, however, researchers have found methods of harnessing the abundant potential energy within plasmas and converting it to numerous practical applications. These applications span the engineering disciplines ranging from nuclear fusion to research and diagnostics of medicine and agriculture to environmental tracking of pollutants<sup>2</sup>. In addition to these applications, plasmas can also be used for:

- the low pressure processing of materials
- the use of plasma thermocouples which allow greater extraction of thermoelectric power from nuclear reactors, especially compared to conventional metal combinations<sup>3</sup>
- the fabrication of sophisticated circuitry in the semiconductor industry that possesses higher speeds and densities
- plasma deposition of thin films, growth of oxide layers, and etching
- providing an efficient oxidation medium to make toxic chemical environments benign<sup>4</sup>

- **the propulsion of spacecraft**

**The potential for plasma propulsion as a substitute for chemical propulsion in deep space travel and station keeping has been under evaluation for the past decade. In fact, plasma propulsion has become a reality for the low-thrust, high-specific impulse applications commonly found in gravity-free environments. However, conventional methods of plasma formation and sustainment with high-voltage electrodes possess lifetime limitations due to the erosion of electrode tips. The Microwave Electrothermal Thruster (MET) was developed to eliminate this limitation since it has no electrode in contact with the working fluid. The MET concept has been demonstrated, both theoretically and experimentally, to be a viable substitute for chemical propulsion.**

**The basis of plasma propulsion, in general, lies in the conversion of electrical energy into kinetic energy to generate thrust. With the MET, this is accomplished by interacting electromagnetic radiation with a flowing gas. The free electrons are accelerated in the electromagnetic field to energies sufficiently high to ionize other atoms by collisions. The resulting chain of collisions caused by the released electrons produce the plasma, which is simply a collection of electrons, ions, and neutral species. When the ionized species recombine back to their atomic states they release their energy of dissociation as heat, thus increasing the temperature of the gas as it flows out of the system. This high energy gas is thermodynamically expanded through a nozzle**

to produce thrust. In one version of the MET concept, illustrated in Figure 1.1, the power would be beamed to the spacecraft from a space station or planetary base. Another option would be an on-board microwave frequency oscillator powered by solar or nuclear energy. The conversion from electrical to kinetic energy occurs in the energy absorption chambers.

### 1.3 Research Objectives

Plasma diagnostic research has been conducted for the past decade to better ascertain fundamental principles underlying the plasma process. The goal of this research is to develop a physical understanding of plasma behavior and the effects of plasma interaction on various engineering systems. The objectives are met through analytical investigations of various macroscopic properties governed by microwave generated plasmas over a broad range of operating conditions. These parameters, which include various gases and their gas mixture ratios, gas flow rates, gas pressure, discharge power, electromagnetic resonance modes, and containment geometry are accurately measured and controlled with the latest instrumentation. The empirical observations are coupled with theory to provide models that will accurately predict the effects of plasma behavior. These models will not only enhance the current understanding of plasma processes, they will also describe the flow fields and temperature distributions around the plasma. These distributions can

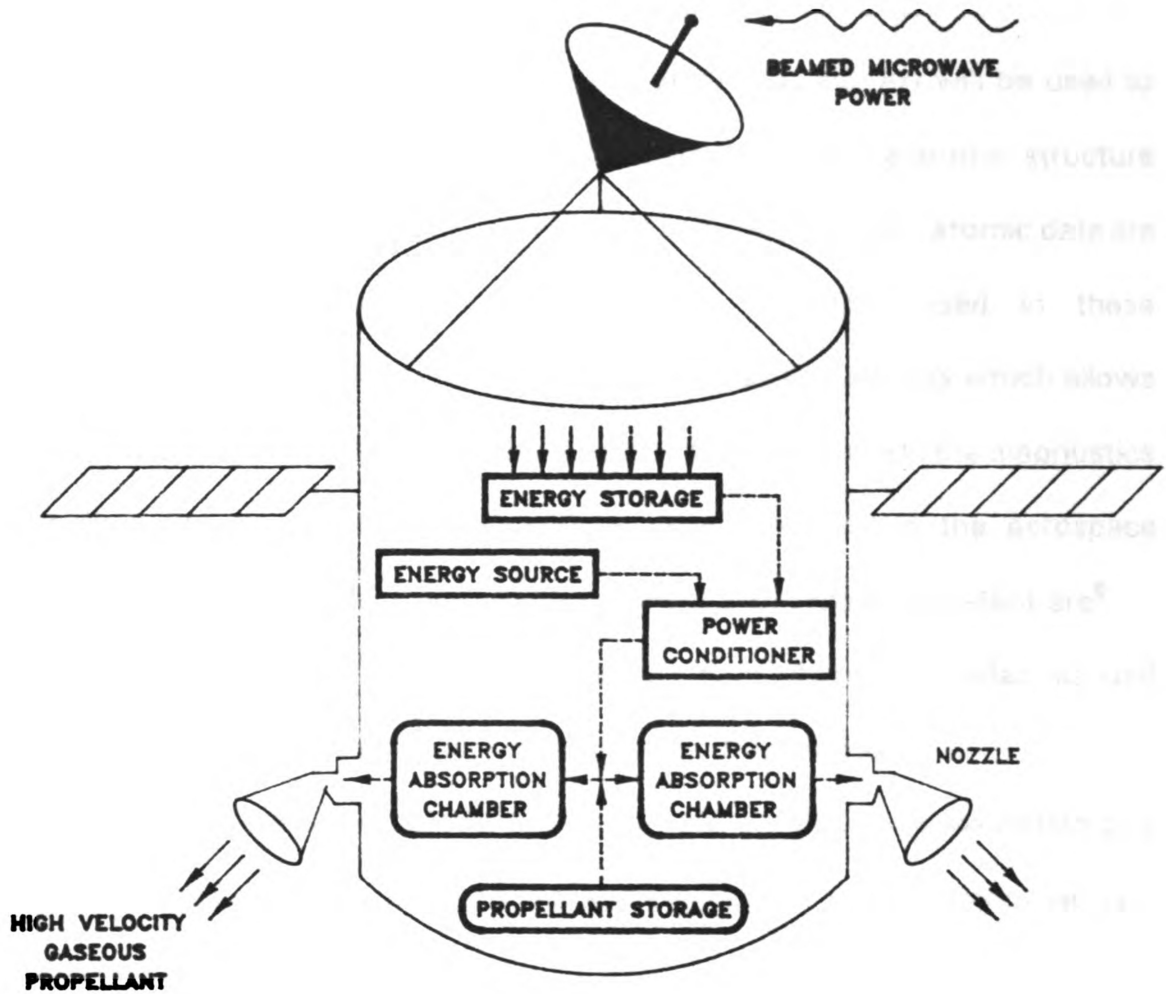


**Figure 1.1 Proposed MET Concept on Board a Satellite**

then be used for boundary conditions in the evaluation of nozzle performance and design.

Though several gases will be used throughout these experiments, helium will be the gas of primary concern and the others ( $N_2$  and Ar) will be used to confirm general trends. Helium was chosen due to its simple atomic structure whereby only two electrons can be detached and consequently, atomic data are widely available. Under the experimental conditions used in these investigations, the helium gas can also be treated as an ideal gas which allows numerous simplifications to be made. Another key advantage in the diagnostics of helium lies in its potential candidacy as a propellant in the aerospace industry. The properties of helium that make it a desirable propellant are<sup>5</sup>

- it is a monatomic gas having no rotational or vibrational modes, as well as no dissociation, which reduces frozen flow losses
- the high ionization potential of helium allows electronic excitation and ionization to occur at much higher temperatures than in any other gas, including hydrogen
- low molecular weight (higher specific impulses,  $I_{sp}$ )
- density is 75% higher than the density of hydrogen which results in a 45% reduction in storage volume and a 32% reduction in surface area
- greater launch safety due to inertness

NASA and other researchers agree that helium will compete favorably with hydrogen systems if adequate efficiencies ( $> 0.7$ ) can be demonstrated.



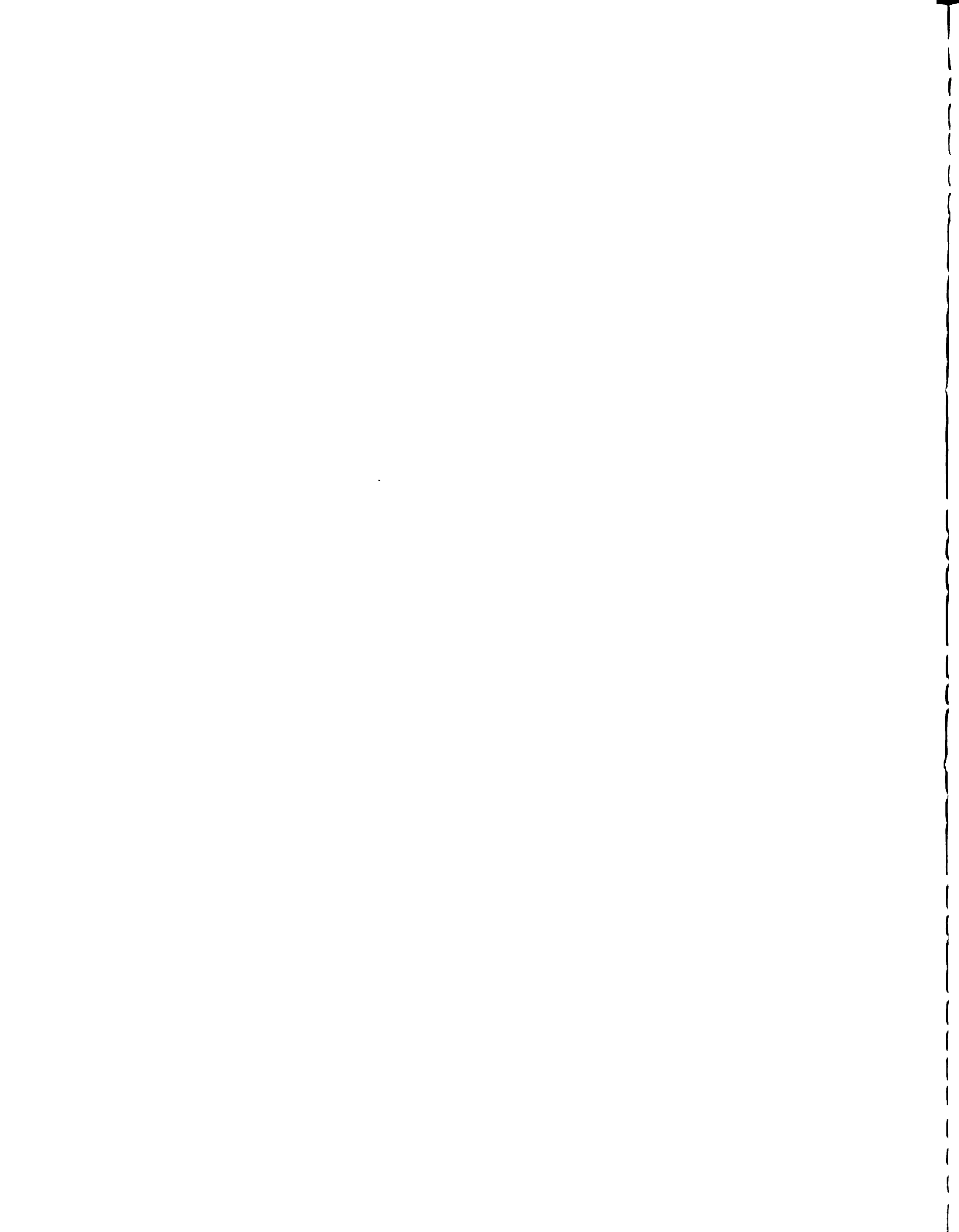
## CHAPTER 2

---

### *Theory*

#### 2.1 Introduction

A gas in its normal state is considered an electrical insulator due to the fact that it contains no free charged particles, only neutral molecules. The gas particles collide with each other in times that are short by comparison with their oscillation periods, and they move an "average" distance, which is short compared with the characteristic wavelengths of the oscillation within the medium. This medium is namely the wavelength of sound and this "average" distance is the mean free path. The internal energy within the gas is transmitted by chains of collisions rather than individual particles<sup>6</sup>. If the gas behaves ideally then the internal energy, and subsequently, the collisional processes, are solely functions of temperature. If a hot gas is in complete thermodynamic equilibrium, its physical state can be completely expressed by a finite number of thermodynamic variables, temperature, pressure, and concentration. The number of particles or "oscillators" can be easily calculated



from these thermodynamic variables.

If electric fields of high intensity are applied across the gas, the free electrons are accelerated to energies sufficiently high to ionize other atoms by collisions, producing a gas discharge. These gas discharges produce an ionized gas containing electrons, ions and neutral particles. When the degree of ionization is equal to unity, the gas is then said to be completely ionized. This collection of free, charged, and neutral particles have a net charge that is small when compared with the charge of either sign. Thus the plasma ensemble may be considered electrically neutral and the high electron mobility makes the plasma a good electrical and thermal conductor. Compared to an unionized gas, the effective collision time within a plasma is long. These unusual characteristics deviate from those of the three known states of matter, and plasmas are consequently referred to as the "4<sup>th</sup> state of matter" <sup>7</sup>.

The three components of a plasma (electrons, ions, neutrals) are characterized by temperature, component pressure, mass (or molar) fraction, and three velocity components. The state of a plasma is also dependent on electric and magnetic field strengths, which are vectors that have three components each. At first, an attempt to thermodynamically characterize the state of a plasma seems hopeless when visualizing the tremendous number of atomic interaction processes which occur among the particles, and between the particles and the photons of the radiation field<sup>8</sup>. This task is indeed tedious when compared to the relatively simple thermodynamic relationships that are

used for an unionized gas. In fact, the local state of a plasma can only be determined if the values of  $6f$  thermodynamic equations and 6 electromagnetic equations are solved, where  $f$  represents the degrees of freedom. Therefore,

$$6f+6 \quad (2.1)$$

equations are needed to thermodynamically describe the local state of a plasma. This expression can be simplified if the plasma is in a state of equilibrium.

The plasma state approaches equilibrium as the number of interactions increases. The closer the plasma is to complete equilibrium the less important it is to know the detailed processes, since individual processes can be grouped together (ie. In equilibrium, particle densities can be calculated from total densities and temperatures). A quantitative description of this process in equilibrium is depicted by Delcroix from a classical mechanics perspective<sup>9</sup>:

"If a great number of systems are enclosed in a container at constant temperature and if, due to their interaction, they reach a state of thermodynamic equilibrium, then each of these systems in this equilibrium state will possess a chaotic energy of thermal motion whose mean value is proportional to the absolute temperature of the container and equal to  $N$  times  $KT/2$ , where  $N$  is the number of degrees of freedom of each of the systems."

Equation 2.1 can be simplified by assuming that the interactions giving

rise to the excitation and ionization of particles is mainly caused by particle impacts and not by radiative processes. Such plasmas are called collision-dominated plasmas. Most plasmas found in the laboratory are collision-dominated and therefore, the above simplification, along with the condition of LTE, appear to be valid<sup>8</sup>. Details of the LTE concept are discussed below.

## 2.2 Equilibrium in Gases

In general, thermodynamic (or thermal) equilibrium utilizes a well-defined temperature as the essential parameter. It is a restrictive concept requiring that<sup>10</sup>:

- Velocity distribution functions of all particles (especially electrons) are Maxwellian.
- Population densities of excited states are Boltzmannian.
- Distribution of molecules and their dissociation products obey the mass action law of Guldberg and Waage.
- Distribution of atoms and ionization products (ions and electrons) obey the Saha-Eggert equation, which is a special case of the mass action law.
- The electromagnetic radiation field has a Planckian distribution, where the radiation temperature equals the kinetic temperature of the reacting particles.

Most laboratory plasmas are optically-thin and the plasma radiation completely escapes from the plasma, thus invalidating the Planckian criterion along with the concept of complete thermal equilibrium<sup>8</sup>. Therefore, the less restrictive concept of local thermal (or thermodynamic) equilibrium is introduced. The basis of LTE lies in the existence of a microreversibility between collisional processes and the assumption that collision-induced transitions and reactions are more frequent than radiative ones. In LTE, all the above criteria hold true for the reacting particles, especially the electrons, but the radiation distribution is allowed to deviate from the Planck function<sup>10</sup>. The assumption of LTE allows all particle densities to be calculated from total densities and temperatures.

For the gas to be in "true" non-equilibrium, different degrees of freedom of the gas must have different temperatures. Furthermore, the energy distribution of an internal degree of freedom must be appreciably different from a Maxwell-Boltzmann distribution and the velocity distribution must be appreciably different from Maxwellian. These conditions may occur when energy is rapidly added to or extracted from a gas at such a high rate that the equilibrium is continuously perturbed or when the different degrees of freedom weakly interact, such as for low density systems where collisions may be too sparse to maintain equilibrium. Non-equilibrium may also be observed when the temperature is measured within a time interval approaching the time required to reach equilibrium.



The equilibrium relation is needed to justify that every atomic process occurs as frequently as its inverse process. Consequently, the relation is invaluable for information concerning collisional and thermodynamic processes. As mentioned earlier, laboratory plasmas normally revolve around the principles of LTE, which differs only slightly from ideal equilibrium. The inner and outer energy state of individual particles in the plasma are populated as in complete thermodynamic equilibrium, but accompanying blackbody radiation, which is created mainly by electronic interactions, is missing or reduced<sup>6</sup>.

The number of unknowns is reduced considerably if various global quantities are introduced that cover, macroscopically, the plasma region. In particular, one temperature is taken for all three components. That is

$$T_P = T_I = T_E = T_N \quad (2.2)$$

where  $T_P$ ,  $T_I$ ,  $T_E$ , and  $T_N$  represent the temperatures of the plasma, ions, electrons, and neutrals, respectively. This simplification is the basis for local thermal equilibrium.

### 2.3 Mean Free Path

As mentioned earlier, the validity of LTE requires that the intensive variable gradients be small over the mean free path. Intuitively, it is then reasonable to expect the mean free path, defined as the average distance traveled by a molecule or atom between successive collisions, to be as small

as possible for this condition to apply. The mean free path,  $\ell$ , is not a directly measurable quantity, but it can be computed by dividing the average molecular (or atomic) velocity by the collision frequency or<sup>6</sup>

$$\ell = \frac{\langle v \rangle}{Z} = \frac{kT}{\sqrt{2}\pi d^2 P} \quad (2.3)$$

where:

$\langle v \rangle$  = average molecular speed  
 $Z$  = collision frequency  
 $k$  = Boltzmann's constant  
 $T$  = temperature  
 $d$  = molecular diameter  
 $P$  = pressure

It is obvious that  $\ell$  is proportional to temperature and inversely proportional to the pressure. Figure 2.1 illustrates the mean free path as a function of pressure for various gases at 1000°K. This figure shows that the mean free path approaches infinity as the pressure approaches zero. Therefore, it is reasonable to expect LTE to become increasingly more valid at higher pressures. This estimation was used to define the pressure range of 0 - 400 Torr for the laboratory experiments of this work.

## 2.4 Validity of the Ideal Gas Law

An assumption that is continuously made throughout these investigations is that the gases in the system behave ideally in the plasma state. Fortunately, this assumption can be objectively confirmed. Wisniewski *et al.* have

## Mean Free Path Function of Pressure for Various Gases

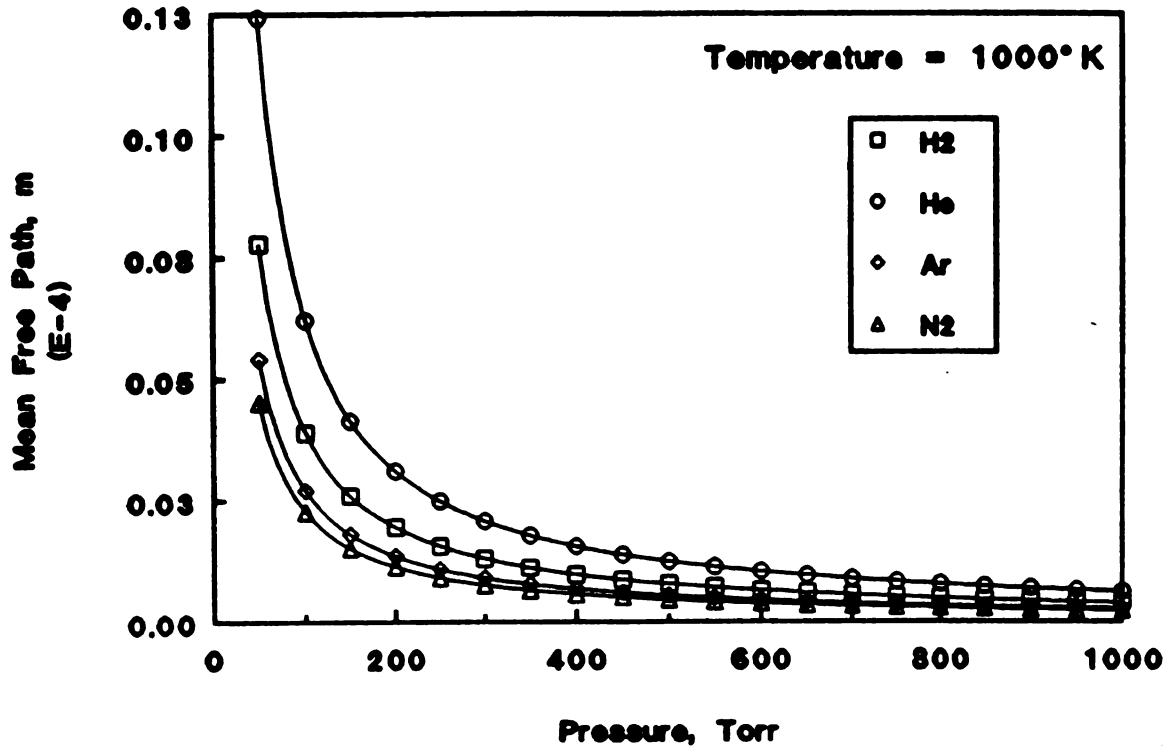


Figure 2.1 Mean Free Path as a Function of Pressure

established the limit from which the ideal gas laws and equations are applicable to the plasma state by the condition<sup>11</sup>:

$$\frac{n_I e^6}{2^{1.5} (kT)^3} \left[ \ln \left( 1 + \left[ \frac{kT}{e^2 n_I^{1/3}} \right]^2 \right) \right]^{1.5} \ll 1 \quad (2.4)$$

where:

$$\begin{aligned} n_I &= \text{number of ions per cm}^3 \\ e &= \text{electron charge} \\ k &= \text{Boltzmann's constant} \\ T &= \text{temperature} \end{aligned}$$

Equation 2.4 is based on the low plasma densities that occur at high temperatures and low pressures. For these conditions, the energies due to van der Waals attractions and Coulomb forces can be neglected and the plasma may be treated as an ideal gas.

The results of this criteria for the helium plasmas at the lower temperatures begin at  $10^{-4}$  and get lower as the temperature and thus, the ion density, is increased. The number of ions per  $\text{cm}^3$  plasma ( $n_I$ ) was conservatively determined, assuming 100% ionization, from the Saha equation and ideal gas law. It therefore validates the assumption that the plasma state is indeed represented as an ideal gas under these conditions.

The ideal gas law was also directly compared to the more accurate Peng-Robinson equation of state to determine if significant changes occurred in the pressure regions of interest. Data was generated for the Peng-Robinson equations using a FORTRAN program to solve the cubic equation. The temperature was held constant at  $1000^\circ\text{K}$  and the pressure was varied from

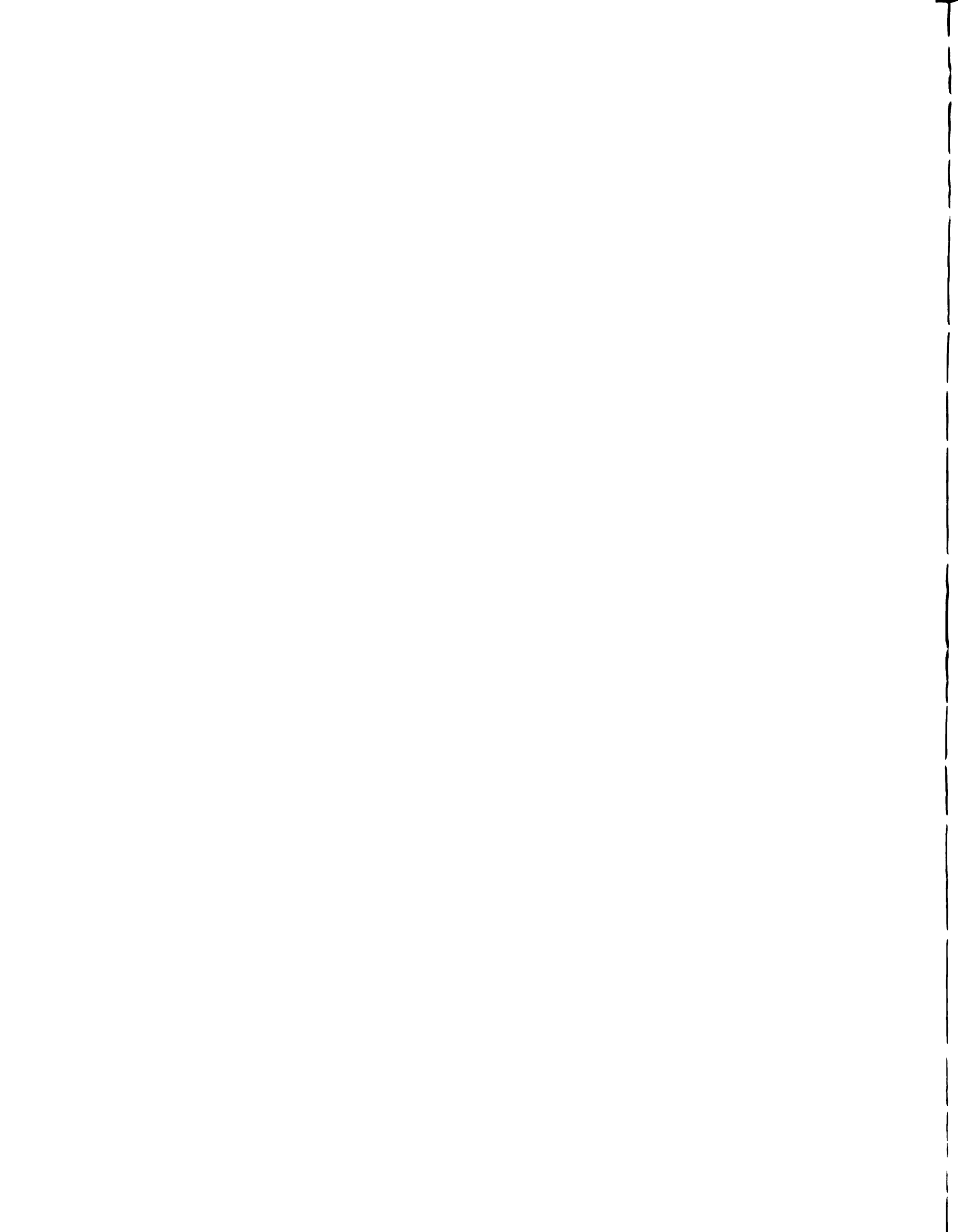
0.01 bar to 20,000 bar. The resulting volumes and compressibilities were compared to that obtained using the ideal gas law. As illustrated in Figure 2.2, the criteria of

$$\frac{V_{Ideal\ Gas}}{V_{Peng-Robinson}} = 1 \quad (2.5)$$

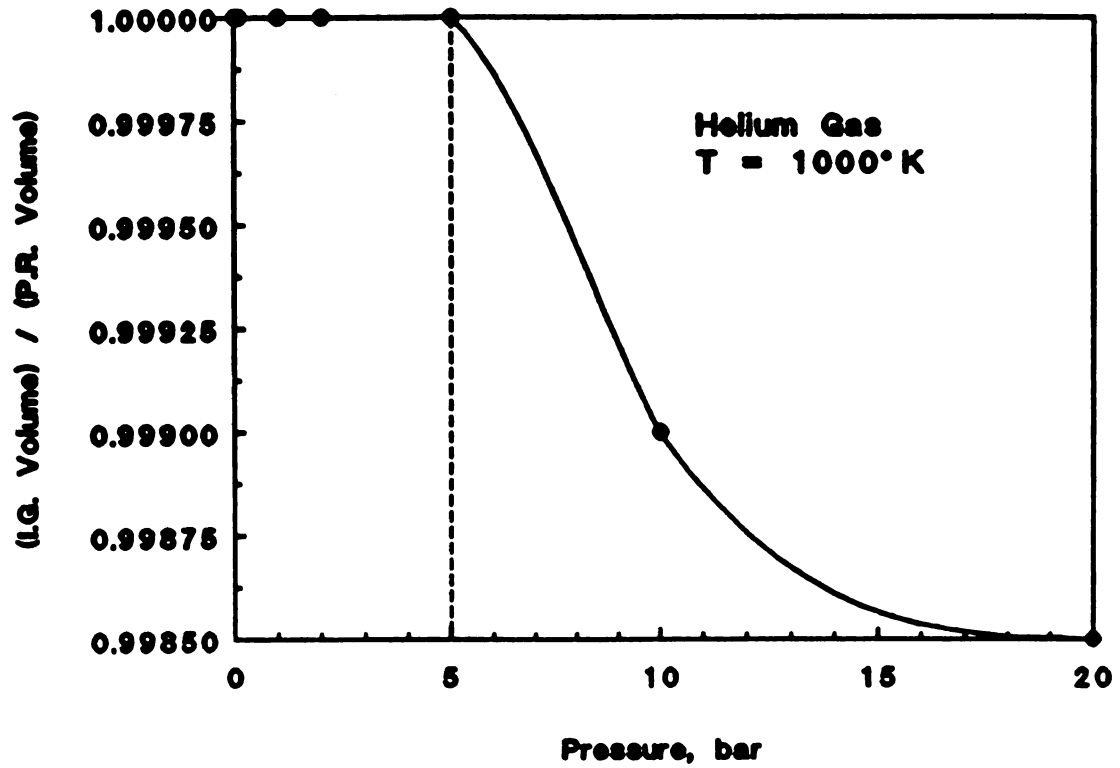
is met for pressures up to 5 bar (3750 Torr). Since the experimental pressures seldom exceed 1000 Torr, this again confirms that the ideal gas law applies to the plasma state in these investigations.

## 2.5 Microscopic Plasma Phenomena

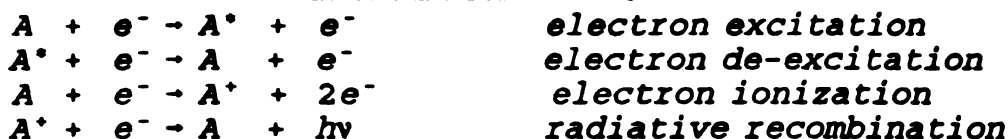
The plasma consists of a collection of electrons, ions, and neutral species continuously interacting through elastic and inelastic collisions. The elastic collisions are important for the transfer of kinetic energy, such as the elastic collision between an electron and a molecule in the presence of an electromagnetic field. The inelastic collisions, which are responsible for the sustainment of the plasma, occur during the ionization processes whereby an electron is made available for further interaction. It is therefore reasonable that the reaction rate around the plasma is the collision rate of the constituent species. In the case of laboratory systems, these collisions are mostly binary and can be generally divided into the following interactions<sup>12</sup>:



**Validity of Ideal Gas Law  
I.G.L. vs. Peng-Robinson E.O.S.**



**Figure 2.2** Volumes Obtained by Ideal Gas Law Compared to those Obtained by Peng-Robinson Equation of State

ELECTRON-NEUTRAL/IONION-NEUTRALNEUTRAL-NEUTRALRADIATION

The radiation group is typically excluded from these investigations due to the assumption that the plasma is collision dominated. This assumption is validated by the fact that most of the emitted radiation is immediately lost to the apparatus<sup>13</sup>. Ion-neutral and neutral-neutral interactions can also be disregarded since they result in either electron transfer or neutral excitation, both of which are incorporated into the electron-neutral/ion interactions. Therefore, only electron-neutral/ion interactions will be of primary concern since they contain the de-excitation and recombination processes that are responsible for the thermal energy generation.

Though single atoms are used in these mechanisms, the relationships apply equally well for gas atoms or molecules due to the thermal dissociation

that occurs at sufficiently high temperatures<sup>11</sup>. At temperatures of the order of 5000°K, it is safe to assume molecular dissociation has occurred and the ionization processes have formed an electronic gas due to the detachment of electrons from the atoms<sup>14</sup>.

The physical attributes of a plasma are also directly related to the local placement of these microscopic phenomena. Concentration gradients are generated in the plasma due to relatively slow surface reactions and fast interior reactions. These gradients induce diffusion of species within the plasma whose rate is primarily pressure controlled. The rate of ion-electron recombination tends to increase dramatically at pressures greater than 400 Torr, which leads to the contraction of the plasma. At low pressures, and hence large interionic distances, expansion of the plasma occurs and approaches the dimensions of the containment due to wall recombination. The relative plasma deformations are illustrated in Figure 2.3. The size of the plasma also effects the density of species, which is proportional to the hatchings in the figure. Variations in plasma dimension are measured through photographic techniques, which are discussed in Chapter 4.

## 2.6 Microscopic Mass Balances

Knowing the exact amount of energy distributed to the plasma from the calorimetry experiments, the microscopic system can be reduced to the plasma



# TYPICAL PLASMA FORMATIONS AT VARIOUS PRESSURES WITHIN QUARTZ CONTAINMENT

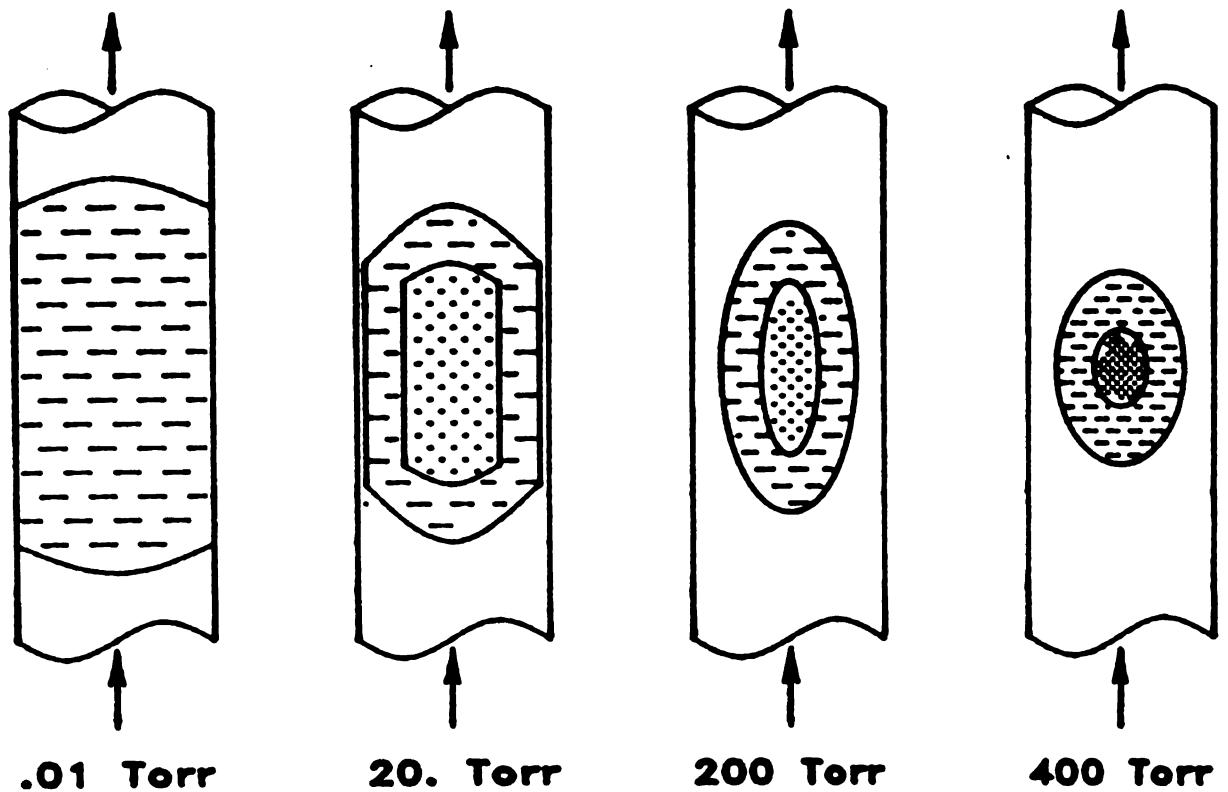


**Figure 2.3** Relative Plasma Deformations Caused by Changes in Pressure

medium which is open to the surroundings with respect to mass and heat flows. The surroundings include the region of recombination. The overall system for the MET concept is found in Figure 2.4. For illustrative purposes, Figure 2.4 shows the direction of flow with gravity but actual experiments are conducted with the gas flow directed against gravity.

The cold propellant entering the quartz discharge tube is coupled with microwave energy "focused" by the specially designed cavity into a specific area to produce the plasma. Radiative, convective, and conductive heat is transferred from the plasma to the immediate surroundings. The radiant energy arises from changes of quantum levels of electrons. One mechanism by which this occurs is by the incoherent emission of photons which causes the blackbody radiation mentioned earlier. The net sums of these energy terms are accounted for from the macroscopic energy balance introduced in Chapter 5. The excited and other charged particles also flow towards the surroundings which through collisional processes recombine downstream with increased kinetic energy. The neutral and recombined species absorbs sufficient energy to detach an outer-shell electron. This energy may come from the collision of the atom with an electron or positive ion, from absorption of a quantum of radiation energy, or from collisions of unionized atoms. Thermodynamic expansion of this highly thermalized propellant generates the desired thrust for the MET application.

The overall mass balance for the MET system is quite simple since it is

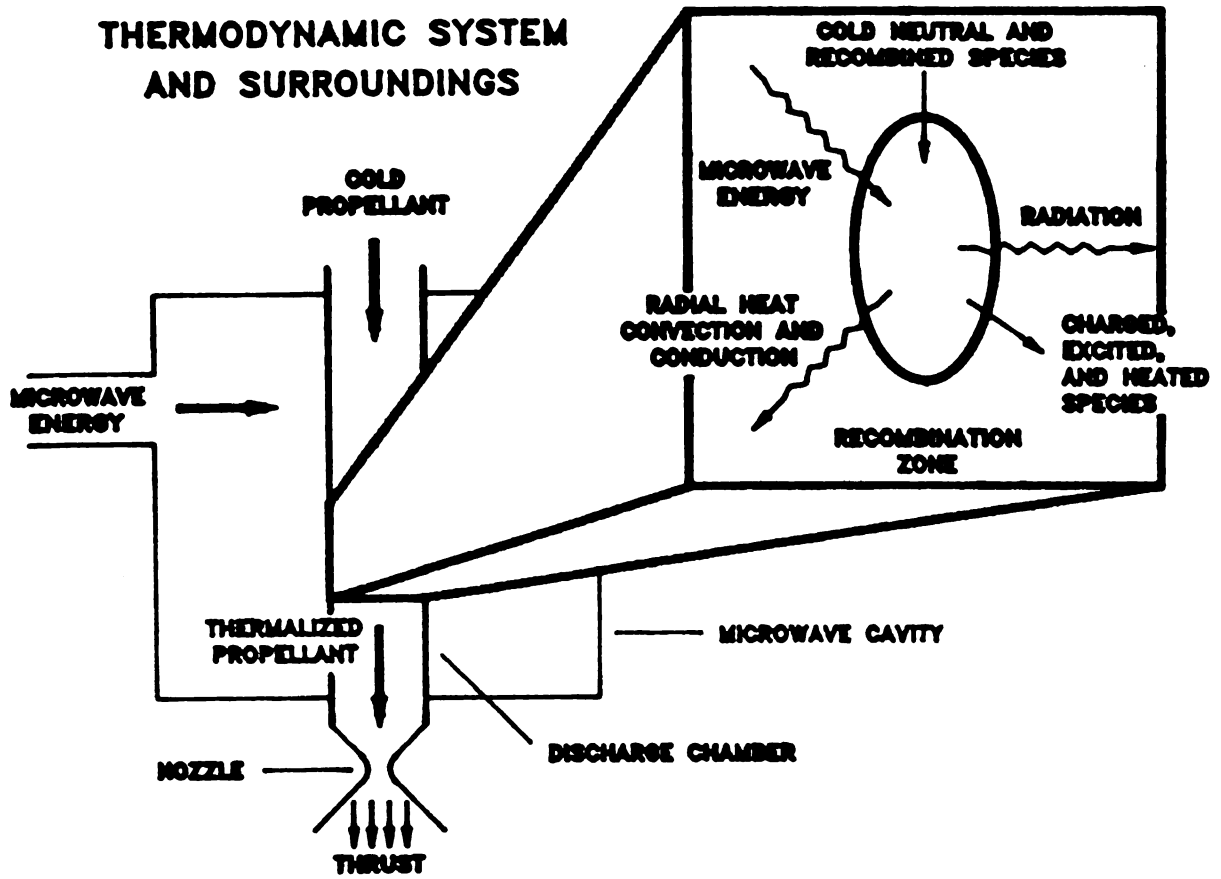


**Figure 2.4** Thermodynamic System for the MET

open to the surroundings, giving

$$M_{in} = M_{out} \quad (2.6)$$

or

$$\begin{aligned} &M_{neutrals} + M_{recombined\ species} \\ &= M_{ions} + M_{electrons} + M_{unionized\ species} \end{aligned} \quad (2.7)$$

The solution to this equation requires experimental data to account for the ionized species and electrons. A solution to this problem can be approximated without experimental data using the Saha equation, which is based on ionization potentials and describes the degree to which neutral species are ionized. Though limited in several respects that will be identified, the Saha equation incorporates many fundamental thermodynamic principles, such as enthalpy, internal energy, and entropy into its derivation. Electrochemical, electrostatic, chemical (or partial molar Gibbs free energy), and ionization potentials of the system(s) under study are used in this equation which makes its popularity widespread in electromagnetic environments.

## 2.7 System Thermodynamics

In general, a local thermodynamic state is used to define individual points of a nonhomogeneous system, that is, a system in which at least some of the intensive variables are functions of time and position. A postulate of LTE states that although a thermodynamic system as a whole may not be in

equilibrium, arbitrarily small elements of its volume are in local thermodynamic equilibrium and have state functions which depend on state parameters through the same relationships as in the case of equilibrium states in classical thermodynamics<sup>11</sup>.

For a system in which this postulate is applicable, the specific entropy and internal energy may be determined at every point in the same way as for substances in equilibrium. The thermodynamic volume, temperature, and pressure can then be defined through the following identity derivation<sup>15</sup>:

$$dU = TdS - PdV \quad (2.8)$$

$$dU = \left(\frac{\partial U}{\partial S}\right)_Y dS - \left(\frac{\partial U}{\partial Y}\right)_S dY \quad (2.9)$$

and therefore

$$T = \left(\frac{\partial U}{\partial S}\right)_Y \quad P = -\left(\frac{\partial U}{\partial Y}\right)_S \quad (2.10)$$

where U and S represent the internal energy and entropy. Under these conditions, the classical thermodynamic equations of state

$$f(Y, P, T) = 0 \quad \text{or} \quad f(U, Y, T) = 0 \quad (2.11)$$

hold at every point, along with the Gibbs and Gibbs-Duhem relations, which are used when considering multicomponent systems and are of particular interest when dealing with the plasma state.

A condition that must be met before this assumption can be accurately

applied is that any gradient that appears among the intensive variables be small over the molecular mean free path<sup>11</sup>. This condition thus requires that all macroscopic variations be sufficiently moderate so that the microscopic collisions are significant. Plainly stated as it relates to plasmas, where the collisional processes tend to dominate over the radiative processes, LTE assumes that the velocity distributions of electrons, atoms, and ions and the degrees of ionization may still be close to those pertaining to a system in complete thermodynamic equilibrium<sup>1</sup>. Local thermal equilibrium then assumes that the temperatures of the electrons, ions, and neutral species equal the temperature of the plasma whole.

The presence of LTE enables critical plasma properties, such as electron number density and electrical conductivity, to be evaluated solely as a function of gas temperature. It is evident that this assumption provides significant simplifications to plasma analysis, but can also provide erroneous conclusions if unjustly applied to systems. Micci *et al.* recognized the questionable validity of LTE in their conclusion which found that the electron densities of their model were not properly accounted for<sup>16</sup>. Another case whereby the assumption of LTE proved incorrect was in a study involving a low power arcjet nozzle conducted by Zube and Myers<sup>17</sup>. Their results concluded that the plasma is actually in nonequilibrium due to the relaxation times exceeding the particle residence times.

It is clear that the plasma state must be represented thermodynamically

as a multicomponent system with the entropy of the system a function of the internal energy, the volume, and the quantity of the individual components,  $N_i$ .

The internal energy can be equated to these variables as well. That is,

$$S = S(U, V, N_i) \quad \text{and} \quad U = U(S, V, N_i) \quad (i=1, 2, 3, \dots, k) \quad (2.12)$$

and the exact differential of the internal energy for an open system is of the form similar to that giving in Equation 2.9,

$$dU = \left( \frac{\partial U}{\partial S} \right)_{V, N_i} dS + \left( \frac{\partial U}{\partial V} \right)_{S, N_i} dV + \sum \left( \frac{\partial U}{\partial N_i} \right)_{S, V} dN_i \quad (2.13)$$

and

$$T = \left( \frac{\partial U}{\partial S} \right)_{V, N_i} \quad -P = \left( \frac{\partial U}{\partial V} \right)_{S, N_i} \quad \mu_i = \left( \frac{\partial U}{\partial N_i} \right)_{S, V} \quad (2.14)$$

### 2.7.1 Chemical Potential

The partial derivative,  $\mu_i$ , is commonly referred to as the chemical potential of the  $i^{\text{th}}$  component. The chemical potential is a useful relation as evidenced by the following derivation. Equation 2.13 can be rearranged to yield the Gibbs relation

$$dU = TdS - PdV + \sum \mu_i dN_i \quad (2.15)$$

Other Gibbs relations can be obtained similarly by utilizing the fundamental definitions of enthalpy,  $H$ , Helmholtz free energy,  $A$ , and Gibbs

free energy, G, which are

$$H = U + PV \quad A = U - TS \quad G = H - TS \quad (2.16)$$

to give

$$\begin{aligned} dH &= TdS + VdP + \sum \mu_i dN_i \\ dA &= -SdT - PdV + \sum \mu_i dN_i \\ dG &= -SdT + VdP + \sum \mu_i dN_i \end{aligned} \quad (2.17)$$

Rewriting the chemical potential to include the above partial derivatives gives

$$\mu_i = \left( \frac{\partial H}{\partial N_i} \right)_{S,P} = \left( \frac{\partial A}{\partial N_i} \right)_{T,V} = \left( \frac{\partial G}{\partial N_i} \right)_{T,P} \quad (2.18)$$

$$= \tilde{U}_i + P\tilde{V}_i - T\tilde{S}_i \quad (2.19)$$

$$= \tilde{G}_i \quad (2.20)$$

From Equations 2.18 - 2.20 it can be seen that the chemical potential is therefore equal to the partial molar Gibbs free energy<sup>11</sup>.

Continuing the assumption that the gas behaves ideally, the molar fraction,  $x_i$  is

$$x_i = \left( \frac{P_i}{P} \right)_{V,T} = \frac{\tilde{V}_i}{V_i} \quad (2.21)$$

and hence

$$\mu_i = \tilde{U}_i + P_i V_i - T\tilde{S}_i \quad (2.22)$$

which can be more precisely defined as

$$\mu_i = \mu_{0i}(T_0, P_0) + \int_{T_0}^T c_{pi}(T) dT - T \int_{T_0}^T c_{pi}(T) \frac{dT}{T} + RT \ln \frac{P_i}{P_0} \quad (2.23)$$

This finalized expression for the partial molar Gibbs free energy, where  $\mu_{0i}$  denotes the chemical potential of component  $i$  in the reference state at temperature  $T_0$  and pressure  $P_0$ , provides the basis for following derivation of the Saha Equation<sup>11</sup>.

### 2.7.2 Saha Equation

Typically, the ionization of a gas atom  $A$  occurs by the following mechanism:



where  $A$  decomposes into positive ions,  $A^+$ , and negative electrons,  $e^-$ . At equilibrium, the summation of chemical potentials for these three components multiplied by their corresponding stoichiometric coefficient is zero

$$\sum_i \nu_i \mu_i = 0 \quad \text{OR} \quad \mu_A - \mu_{A^+} - \mu_e = 0 \quad (2.25)$$

where the subscripts  $A$ ,  $A^+$ , and  $e$  denote the unionized atoms, positive ions, and electrons, respectively. A similar expression can also be derived using the electrochemical potentials, which is a more extensive property that utilizes the chemical potentials as well as the electrostatic potentials and electron charge.

In accordance with Equation 2.19 and the ideal gas assumption whereby Dalton's law

$$\sum_{i=1}^k P_i = P \quad (2.26)$$

holds true, the chemical potential can be expressed as

$$\mu_i = \bar{H}_i - T\bar{S}_i \quad (2.27)$$

or, more specifically

$$\begin{aligned} \mu_i = & C_{pi}T - C_{pi}T \ln T + RT \ln P_i + H_{0i} - C_{pi}T_0 \\ & + (C_{pi} \ln T_0 - R \ln P_0 - S_{0i}) T \end{aligned} \quad (2.28)$$

where  $H_{0i}$  and  $S_{0i}$  are molar enthalpy and entropy of component  $i$  in the reference state. If the reference state is taken at  $T_0 = 0^\circ\text{K}$  Equation 2.28 can be simplified to

$$\mu_i = C_{pi}T - C_{pi}T \ln T + RT \ln P_i + H_{0i} - S_{00i}T \quad (2.29)$$

where:

$$S_{00i} = S_{0i} - C_{pi} \ln T_{00} + R \ln P_0$$

is the reference constant introduced for the entropy at a new reference temperature given by  $T_{00}$ .

Equation 2.29, combined with Equation 2.25 yields the general expression

$$\begin{aligned} & \left( \sum_I \nu_i C_{pi} \right)^T - \left( \sum_I \nu_i C_{pi} \right)^T \ln T + RT \ln \left[ \frac{P_i P_e}{P_a} \right] \\ & + \sum_I \nu_i H_{0i} - \left( \sum_I \nu_i S_{00i} \right)^T = 0 \end{aligned} \quad (2.30)$$

This is an important expression in that it is composed of the vital thermodynamic properties necessary to adequately quantify the plasma state.

The sub-expression

$$\sum_I \nu_i C_{pi} = C_{p(A^*)} + C_{p(e)} - C_{p(A)} \quad (2.31)$$

compensates for any change in the heat capacity that may occur during the ionization reaction at constant pressure.

The sub-expression

$$\sum_I \nu_i H_{0i} = H_{0(A^*)} + H_{0(e)} - H_{0(A)} = I_i \quad (2.32)$$

determines the change in enthalpy that occurs during the ionization reaction at a temperature of 0°K.  $I_i$ , more commonly referred to as the ionization potential, is the work required to remove an electron from its atomic orbit and place it at rest an infinite distance.

The sub-expression

$$\sum_I \nu_i S_{00i} = S_{00(A^*)} + S_{00(e)} - S_{00(A)} \quad (2.33)$$

is used to determine the entropy changes that occur during the reaction.

The general form of the Saha equation can now be derived from

rearranging Equation 2.30 to give

$$\frac{P_{(A^+)} P_{(e)}}{P_{(A)}} = BT^{\frac{1}{R} \sum_I \nu_i c_{pi}} \exp\left[-\frac{I_1}{RT}\right] \quad (2.34)$$

where:

$$B = \exp\left[\frac{1}{R} \sum_I \nu_i (S_{00i} - C_{pi})\right]$$

For the ideal gas in this investigation,

$$c_{pi} = \frac{5}{2}R \quad \text{and} \quad \frac{1}{R} \sum_I \nu_i c_{pi} = \frac{5}{2} \quad (2.35)$$

and the finalized expression for the Saha equation becomes

$$\frac{P_{(A^+)} P_{(e)}}{P_{(A)}} = T^{\frac{5}{2}} \exp\left[\left(\frac{1}{R} \sum_I \nu_i (S_{00i} - C_{pi})\right) - \frac{I_1}{RT}\right] = K_p(T) \quad (2.36)$$

where:

- $K_p(T)$  = equilibrium constant for reaction
- $P_{(A^+)}$  = partial pressure of ions
- $P_{(e)}$  = partial pressure of electrons
- $P_{(A)}$  = partial pressure of unionized atoms
- $I_1$  = ionization potential

Equation 2.36, along with some basic kinetics can be employed to quantitatively solve the mass balance for the experimental investigation, which includes helium gas. Helium is often used in plasma diagnostics since it is a simple gas whereby only two electrons can be detached and consequently, atomic data are widely available.

### 2.7.3 Degree of Ionization

To solve the mass balance, the plasma state must be further characterized by the degree to which ionization occurs. Simply stated, this quantity is the ratio of the number of moles of ionized atoms,  $n_i$ , to the number of moles of atoms before ionization begins,  $n_0$ , or

$$\beta = \frac{n_i}{n_0} \quad (2.37)$$

With the exception of atomic hydrogen, most gases will undergo multiple ionization at temperatures in excess of  $10^4$  °K, therefore, a more general expression must be used for the degree of ionization. The degree of k-fold ionization, that is the number of electrons (k) leaving the electronic shell of the atom, can be defined as

$$\beta_k = \frac{n_k}{n_{(k-1)}} \quad (2.38)$$

The ionization of helium proceeds according to the scheme



that is, the monatomic helium atoms give rise to helium ions and electrons. The resulting gas can then be treated as a mixture of proton gas and electron gas, which are both treated as ideal gases. Since helium has two available electrons to ionize, double ionization can also occur at sufficiently high

temperatures.

In general, the summation of the molar fractions within the gas must equal 1. The number of ions in the plasma must be equal to the number of electrons, since each is responsible for the other. These relations can be written as molar fractions giving

$$x_{(A)} + x_{(A^{\cdot})} + x_{(e)} = 1 \quad \text{and} \quad x_{(A^{\cdot})} = x_{(e)} \quad (2.40)$$

and the total and partial pressures can be defined as

$$P = P_{(A)} + P_{(A^{\cdot})} + P_{(e)} \quad \text{and} \quad P_{(e)} = P_{(A^{\cdot})} \quad (2.41)$$

so

$$P = P_{(A)} + 2P_{(e)} = P_{(A)} + 2P_{(A^{\cdot})} \quad (2.42)$$

where:

$$P_{(A)} = x_{(A)}P \quad P_{(A^{\cdot})} = x_{(A^{\cdot})}P \quad P_{(e)} = x_{(e)}P$$

According to Equation 2.38, at equilibrium,  $He_{(1)}\beta_{(2)}$  out of  $He_{(1)}$  moles of singly-ionized helium has become doubly-ionized, leaving the following concentrations of species remaining in the gas

$$He_{(1)} = He_{(1)}(1 - \beta_{(2)}) \quad (2.43)$$

$$He_{(2)} = He_{(1)}\beta_{(2)} \quad (2.44)$$

$$e^- = He_{(1)}(1 + \beta_{(2)}) \quad (2.45)$$

The total number of moles of components in the helium plasma where

double ionization can occur is

$$\begin{aligned}
 N &= He_{(1)} + He_{(2)} + e^- \\
 &= He_{(1)} (1 - \beta_{(2)}) + He_{(1)} \beta_{(2)} + He_{(1)} (1 + \beta_{(2)}) \\
 &= He_{(1)} (2 + \beta_{(2)})
 \end{aligned} \tag{2.46}$$

The partial pressures of the individual components can be determined from

$$P_{(1)} = \frac{1 - \beta_{(2)}}{2 + \beta_{(2)}} P \quad P_{(2)} = \frac{\beta_{(2)}}{2 + \beta_{(2)}} P \quad P_{(e)} = \frac{1 + \beta_{(2)}}{2 + \beta_{(2)}} P \tag{2.47}$$

Combining Equation 2.47 with Equation 2.36 (Saha equation) allows the degree of ionization for helium to be expressed as

$$K_{p(2)} = \frac{P_{(2)} P_{(e)}}{P_{(1)}} = \frac{(1 + \beta_{(2)}) \beta_{(2)}}{(2 + \beta_{(2)}) (1 - \beta_{(2)})} P \tag{2.48}$$

which upon algebraic manipulation and rearranging gives

$$\beta_{(2)} = -\frac{1}{2} + \sqrt{\frac{1}{4} + \frac{2}{1 + \frac{P}{K_p}}} \tag{2.49}$$

Using Equation 2.49, the degree of ionization for helium is plotted in Figure 2.5 as a function of temperature and pressure. These results correspond well to those obtained by Lick and Emmons, who used a statistical mechanics approach<sup>18</sup>.

The degree of ionization can be used to account for the primary components of the helium plasma, which are the singly- and doubly-ionized atoms and the electrons. The corresponding molar fractions can be relatively determined from the above expressions to give Figure 2.6, which was

## Helium Plasma Degree of Ionization Functions of Temperature and Pressure

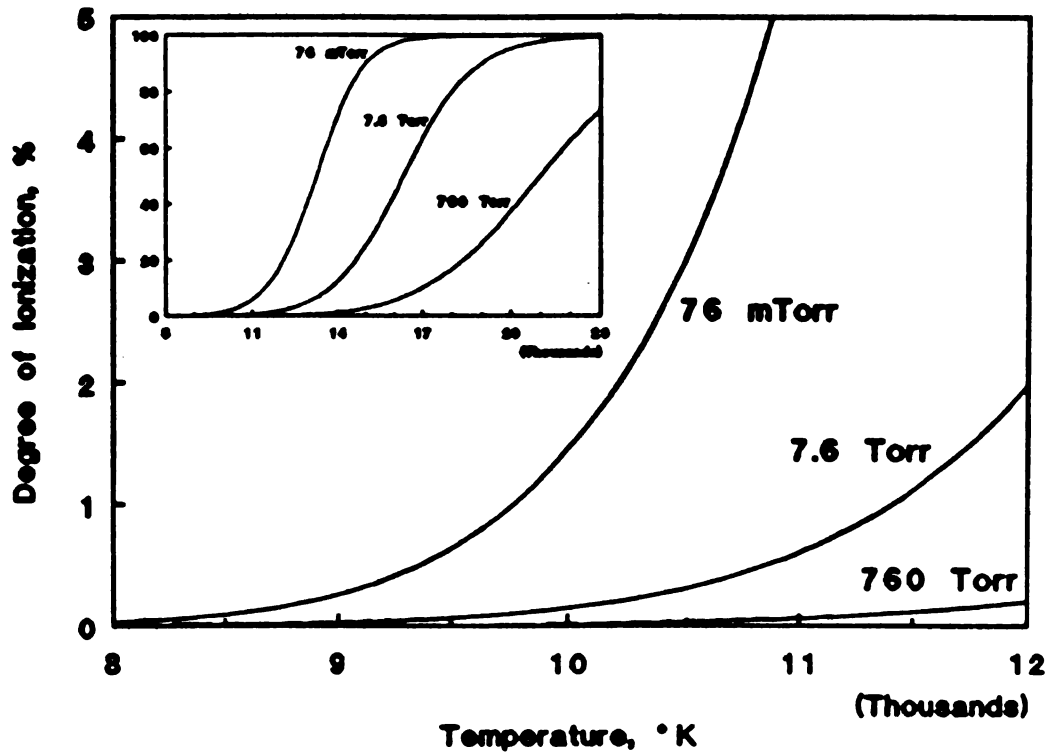


**Figure 2.5** Helium Plasma Degree of Ionization Obtained from the Saha Equation as Functions of Pressure and Temperature

Components of a Helium Plasma  
Function of Temperature,  $P = 76$  mTorr

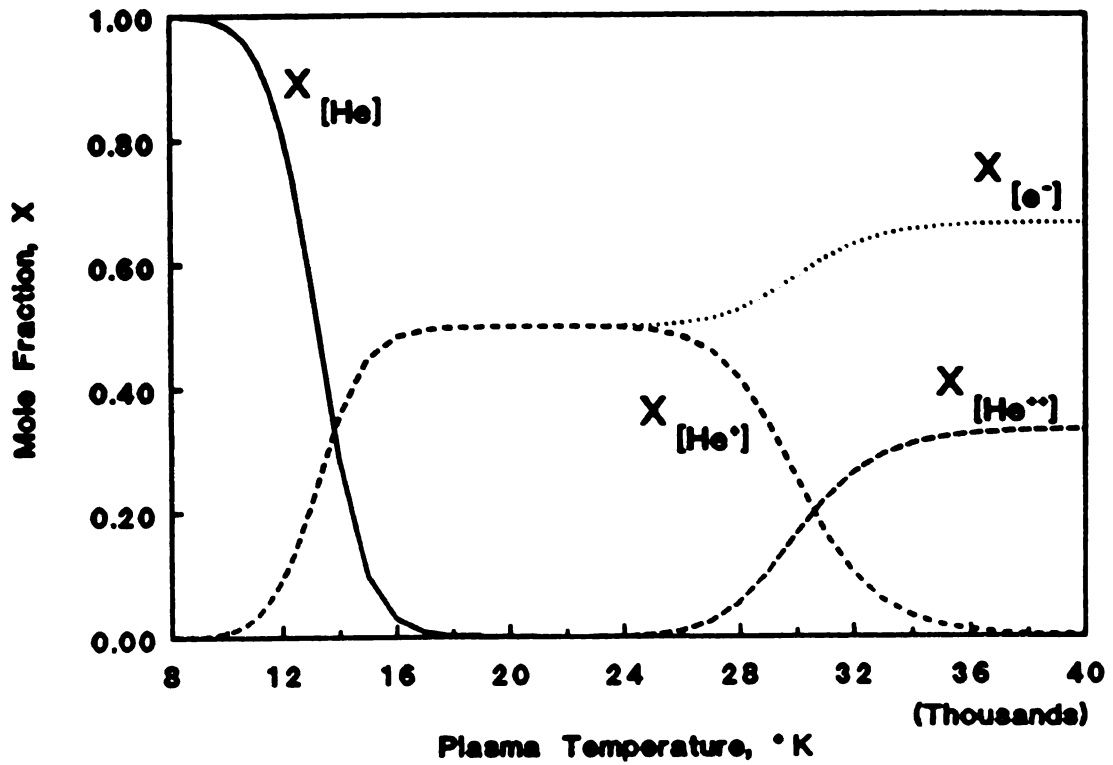


Figure 2.6 Helium Plasma Molar Constituents at 76 mTorr Obtained from the Saha Equation

computed at low pressure as a function of temperature.

As the temperature is increased, the singly-ionized atoms are ionized further, thus producing more electrons to carry on the ionization process. It appears that equilibrium is achieved between the singly-ionized species and electrons up to 20,000°K and above 40,000°K between the singly- and doubly-ionized species and electrons. Current investigations never exceed 20,000°K, so doubly-ionized species normally do not exist.

It is important to note that the Saha equation and thus the degree of ionization is restricted to monatomic gases under conditions such that the solution of unionized gas along with the products of its ionization may be treated as an ideal gas. In accordance with the conditions for thermodynamic equilibrium, all components of an ionized gas should, in the state of equilibrium, be at the same temperature<sup>11</sup>.

It is evident that plasmas can have a high degree of ionization only at low pressures, since the recombination of ions and electrons is directly proportional to the number of molecular collisions and thus to the pressure. At low pressures, and hence large interionic distances, the potential energy of the van der Waals forces, which is inversely proportional to the sixth power of the interionic distances, is negligible in comparison to the other components of the internal energy.

The potential energy of Coulomb electrostatic forces which occur between electrons and oppositely charged ions is another component of the

internal energy of the plasma. This energy is directly proportional to the first power of the distance between ions and electrons. At high temperatures and low pressures, that is, for low plasma densities, the energy of the van der Waals attractions and of the Coulomb forces may be neglected and the plasma treated as an ideal gas<sup>12</sup>.

## 2.8 Electromagnetic Theory

The theory behind electromagnetism as it relates to plasma formations has been presented in detail by previous researchers<sup>19</sup>. To avoid redundancy and still maintain the topic thoroughness, only the finalized derivations of important equations will be presented here.

The electromagnetic field is composed of the electric and the magnetic field vectors. These vector fields satisfy four classic equations known as Maxwell's equations<sup>20</sup>

$$\begin{aligned}
 \nabla \cdot \vec{D} &= \rho \\
 \nabla \times \vec{E} &= -\frac{\partial \vec{B}}{\partial t} \\
 \nabla \times \vec{H} &= \vec{J} + \frac{\partial \vec{D}}{\partial t} = \frac{\partial(\epsilon \vec{E})}{\partial t} \\
 \nabla \cdot \vec{B} &= 0
 \end{aligned}
 \tag{2.50}$$

where:

$\vec{D}$  = electric induction  
 $\rho$  = charge density  
 $\vec{E}$  = electric field  
 $\vec{B}$  = magnetic induction  
 $\vec{H}$  = magnetic field  
 $\vec{J}$  = current density  
 $\epsilon$  = absolute permittivity

The electric induction is a function of the electric field, polarization density, and the permittivity of free space ( $\epsilon_0$ )

$$\vec{D} = \epsilon_0 \vec{E} + \vec{P} \quad (2.51)$$

where:

$\epsilon_0$  = permittivity of free space  
 $\vec{P}$  = polarization density

The polarization density can be eliminated from this expression if the electric susceptibility ( $\chi_e$ ) is known. Furthermore, the dielectric constant ( $\kappa_e$ ) is one plus  $\chi_e$ . The electric induction can be rewritten as

$$\vec{D} = \epsilon_0 (1 + \chi_e) \vec{E} = \epsilon_0 \kappa_e \vec{E} = \epsilon \vec{E} \quad (2.52)$$

The magnetic induction is a function of the magnetic field, the magnetization density, and the permeability of free space ( $\mu_0$ )

$$\vec{B} = \mu_0 (\vec{H} + \vec{M}) \quad (2.53)$$

where:

$\mu_0$  = permeability of free space  
 $\vec{M}$  = magnetization density

Once again, the magnetization density can be dropped from this term if the

magnetization susceptibility ( $\chi_m$ ) is known. The relative permeability ( $\kappa_m$ ) is one plus  $\chi_m$ . The magnetic induction can be rewritten as

$$\vec{B} = \mu_0 (\chi_m + 1) \vec{H} = \mu_0 \kappa_m \vec{H} = \mu \vec{H} \quad (2.54)$$

The current density is a scalar multiple of the electric field plus the velocity of the media crossed with the magnetic induction. That scalar function is the electrical conductivity ( $\sigma$ ). The current density is given as

$$\vec{J} = \sigma \vec{E} + \vec{v} \times \vec{B} = n_e \vec{v} \quad (2.55)$$

where:

$$\begin{aligned} \sigma &= \text{electrical conductivity} \\ \vec{v} &= \text{velocity of media} \\ n_e &= \text{electron density} \end{aligned}$$

## CHAPTER 3

---

### *Plasma Diagnostic System*

#### 3.1 Introduction

The plasma diagnostic system is designed to generate a stable plasma in an isolated environment so various fundamental properties of the plasma may be evaluated. These properties are studied through dimensional, calorimetric, and spectroscopic analyses. In order to provide accurate and reliable measurements, the system must allow for various parameters to be fixed relative to one another and all active experimental components must be calibrated independently.

The current system has been significantly modified from previous systems to allow for flexibility in the research program along with the physical enhancement of data measurements. The majority of the system components are now digitalized or integrated to the computer data acquisition. These changes will be explained in detail in the appropriate sections of this chapter. An overview of the current plasma diagnostic system is illustrated in Figure 3.1

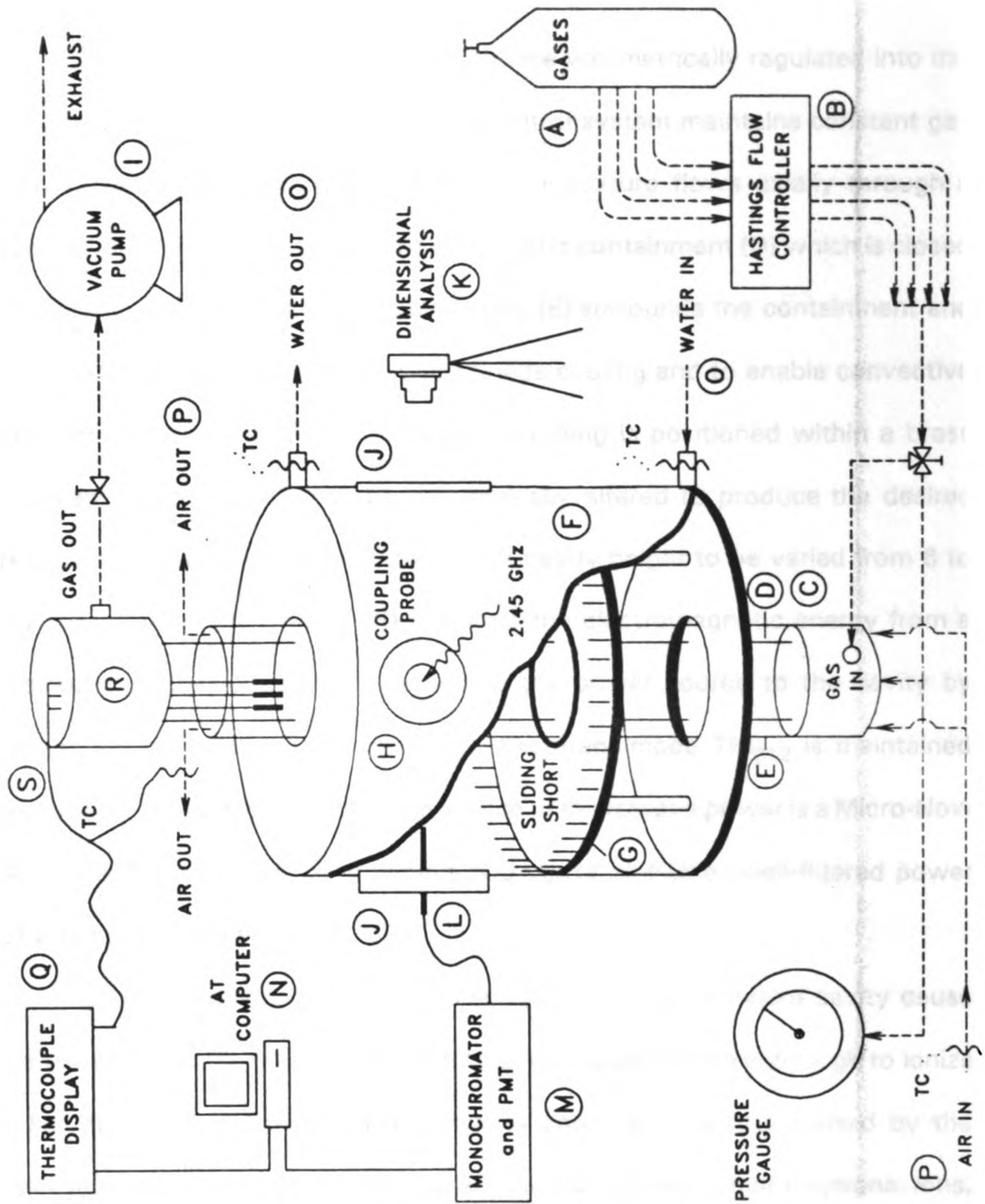


Figure 3.1 Experimental Configuration

and summarized below.

High-purity experimental gases (A) are volumetrically regulated into the system by a digital controller (B). This control system maintains constant gas flow rates and mixture ratios. The gas or mixture flows axially through a specially designed collar (C) and into the quartz containment (D) which is closed to the environment. A second quartz tube (E) surrounds the containment and air is passed through the annulus to provide cooling and to enable convective heat losses to be measured. The quartz tubing is positioned within a brass resonant cavity (F) that can be mechanically altered to produce the desired resonance. A sliding short (G) allows the cavity height to be varied from 6 to 16 cm. The coupling probe (H) transfers the electromagnetic energy from a bidirectional coaxial cable connected to the power source to the cavity by means similar to that of an antenna. Resonant mode  $TM_{012}$  is maintained throughout these experiments. The source of microwave power is a Micro-Now 420B oscillator capable of providing 400 watts of stable, well-filtered power at a fixed frequency of 2.45 GHz.

The electromagnetic fields generated within the resonant cavity cause free electrons in the gas to be accelerated to energies sufficiently high to ionize other atoms by collisions. The resulting chain of collisions caused by the released electrons produce the plasma, which is a collection of electrons, ions, and neutral species. In order to initialize the plasma, the system must be evacuated to pressures less than 1 Torr. This creates the large mean free paths

and thus, the sufficient electron energies required for ionization. An NRC vacuum pump (I) provides a low pressure environment but is limited to 1 Torr.

The resonant cavity contains two open ports (J) positioned  $90^\circ$  on either side of the coupling probe. These ports allow photographic and spectroscopic investigations to be conducted. The size, shape, and color of the plasma are macroscopically characterized by photographic techniques (K) over various operating conditions. These measurements provide necessary data used in heat and mass transport models.

The optical spectroscopy system is used to measure the line intensity and widths of the plasma emission. A fiber optic cable (L), specially designed to withstand the heat and microwave interactions, is positioned within the cavity at various points along the plasma. The fiber optic is connected to the spectroscopic system (M), which consists of a monochromator, photomultiplier tube, power supply, and electrometer. The processed output is sent to a data acquisition system where it is recorded on an AT computer (N). The electron density, plasma frequency, percent ionization, atomic electronic temperature, and molecular rotational and vibrational temperatures of the plasma are determined as functions of absorbed power, pressure, and flow rate.

The experimental system is designed to allow for calorimetric investigations to accurately measure energy inputs, outputs, and distribution within the cavity. Energy lost to the cavity walls is calculated by measuring temperature changes of water (O) circulating around the cavity. At low

pressures, wall recombination processes dominate the system and consequently, convective heat transfer from the discharge tube wall back into the plasma occurs. Convective heat losses out of the plasma is calculated by measuring the temperature difference of the air (P). Type T thermocouples connected to an Omega 400B Digicator (Q) measure the inputs and outputs of the air and water streams. The rate of energy that is transferred to the experimental gas as it flows through the plasma system is determined as a function of absorbed power, pressure, and flow rate from an energy balance around the system.

The highly thermalized gas exits through the top collar (R) and is exhausted through the pump. The top collar allows for the radial placement of four additional thermocouples (S). This design enables temperature profiles of the exiting gas stream to be made over various operating conditions. It also allows for the time measurement of thermal equilibrium when parameters are adjusted.

### 3.2 Microwave Source

The microwave source assembly is illustrated in Figure 3.2. The microwave frequency oscillator is a Micro-Now Model 420B1 (A) that provides 50 to 400 watts of stable, well-filtered microwave power at a fixed frequency of 2.45 GHz to the cavity input probe. The maximum rating for the source is

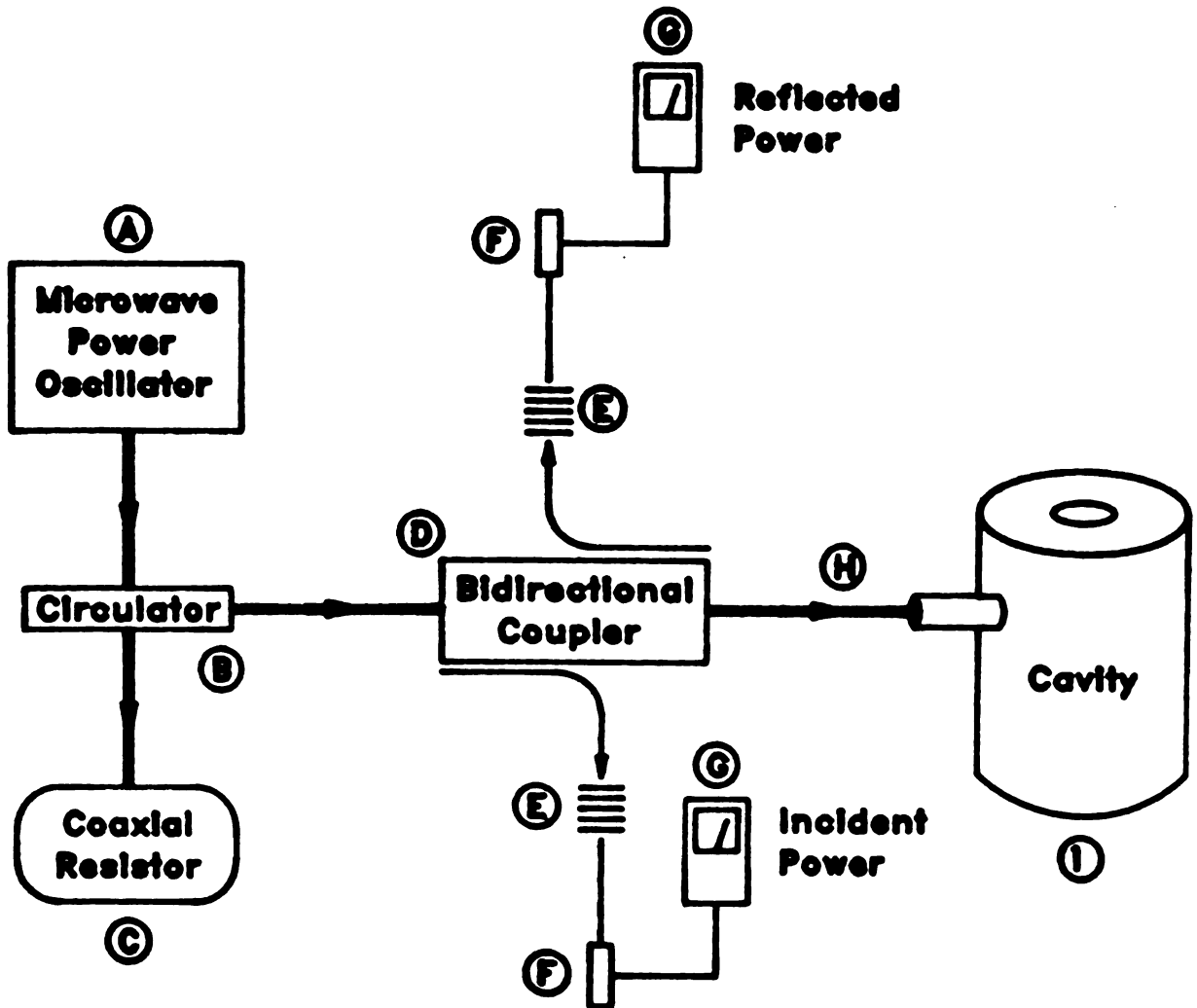


Figure 3.2 Microwave Source and Peripherals

500 watts but losses incurred from the microwave coaxial cable, circulator, and bi-directional coupler reduces the maximum input to 400 watts. A Ferrite 2620 circulator (B) is connected to the oscillator and protects the magnetron from reflected signals and increases the accuracy of the power measurements (B). This is accomplished by providing the incident and reflected power sensors with 20 Db of isolation. The system is further protected by reflected power with a 50Ω Termaline 8201 coaxial resistor, or dummy-load (C). The incident and reflected power levels are sampled by a 500 watt, 20 dB bidirectional coupler (D). These power samples are further diminished by 20 dB attenuators (E) and are measured by Hewlett-Packard Model 8481A sensors (F) and Model 435A analog power meters (G). The coaxial transmission line (H) transfers the microwave energy to the microwave resonant cavity (I).

### 3.3 Gas Flow System

Ultra-pure "five-9" gases (99.999%), including nitrogen, helium, and argon, are used in these investigations. Contamination found in spectroscopic analyses prevented the use of conventional "four-9" gases (99.99%). The gas flow rates and mixture ratios are controlled by Hastings 202A Flow Controllers powered by a CPR-4A digital source. These gases flow axially through the plasma containment assembly and are exhausted out of the building.

The pressure within the system is controlled with an NRC vacuum pump

from 0.25 - 1000 Torr. The pump was completely disassembled and refurbished, including filter, oil, and fitting changes, to achieve the 250 mTorr pressures. The flow system accommodates both low- and high-pressure environments by means of a reduced pressure regulator for fine adjustments coupled with a course adjustment for higher pressures. The high pressures are measured with a Heise gauge (0-1600 Torr) and an analog Hastings SV-1 gauge (0-200 mTorr) accurately measures the low pressures.

### 3.4 Plasma Containment Assembly

The plasma region is sustained in a cylindrical quartz tube having an outer diameter of 33 mm. This "inner" tube is surrounded by a 50 mm O.D. "outer" quartz tube which enables air to be passed through the annulus for cooling and calorimetric studies (ie.  $T_{\text{air out}} - T_{\text{air in}} = \Delta T$ ). Quartz is used for the containment since it is transparent to microwave energy and to visible light, thus enabling spectroscopic and photographic diagnostics to be performed on the plasma. The plasma containment assembly is illustrated in Figure 3.3.

Aluminum collars are epoxied to the ends of the quartz tubing and have historically simply provided the connections for the entering and exiting gas streams. Design modifications of the collars have provided additional diagnostic capabilities. The old collars prevented the quartz tubing from being replaced or cleaned once inside the cavity. The modified collars can be easily

## COLLAR ASSEMBLY

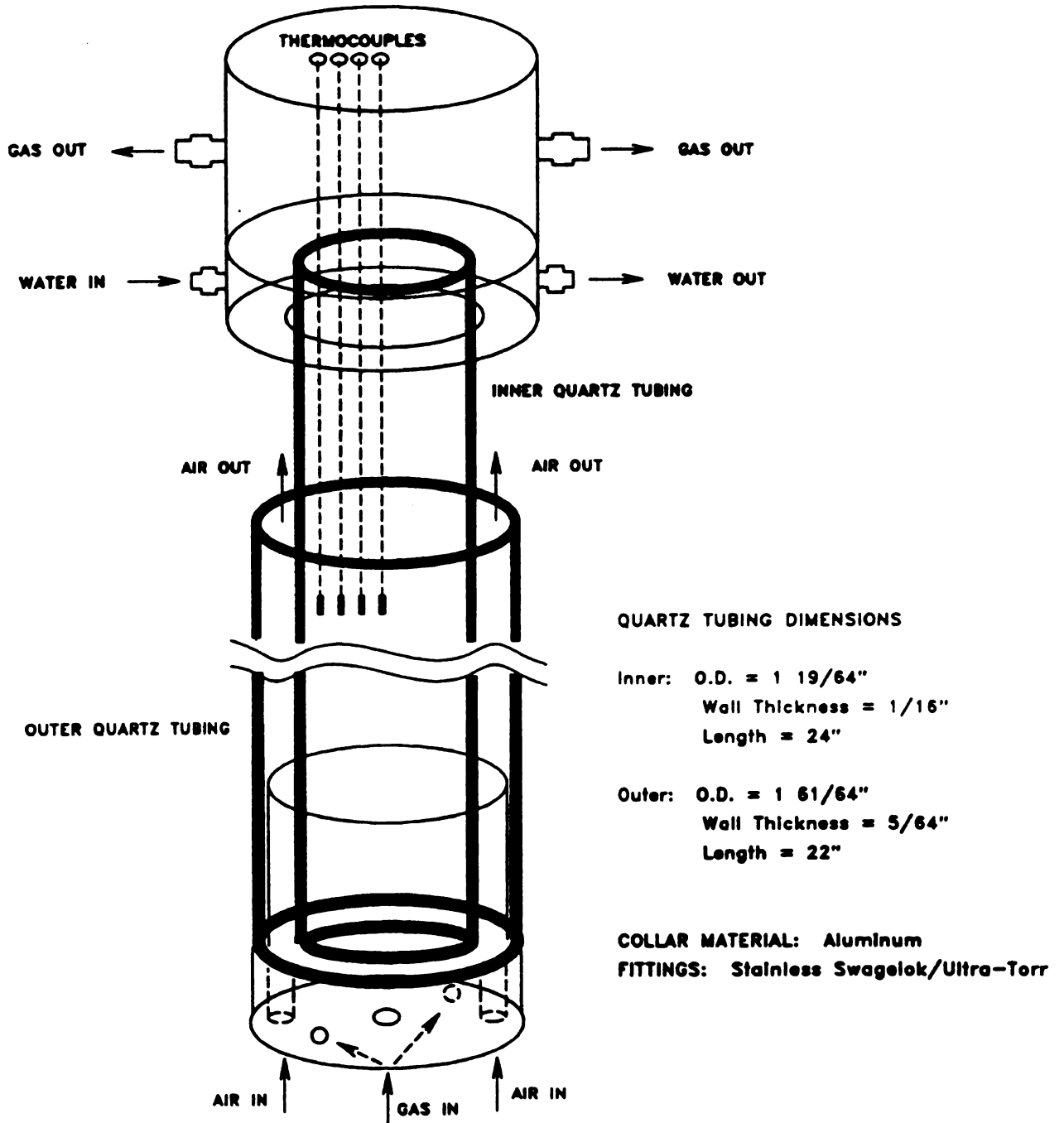


Figure 3.3 Plasma Containment Assembly

removed from the cavity. The design modifications for the top and bottom collars are illustrated in Figures 3.4 and 3.5.

The modified bottom collar contains two radial inlet ports, positioned 180° from each other, in addition to the axial inlet port. These ports allow for swirling gas flows through the containment, which has been determined to aid in plasma stability<sup>21</sup>. Swirling gas flows also provide angular velocity terms to the equations of motion. The top collar contains four "Cajon" ultra-torr fittings that allow solid Type K subminiature thermocouples to be lowered directly into the exiting propellant stream. This configuration is used to determine radial, as well as axial, temperature profiles of the thermalized gas. The top collar is also water cooled to prevent the high temperatures from damaging the epoxy seal.

### 3.5 Microwave Cavity

As depicted in Figure 3.6, the plasma containment assembly (A) is positioned vertically within a brass resonant cavity, which can be mechanically altered to produce the desired electromagnetic field to maintain the plasma. The cylindrical cavity has a fixed 178 mm inner diameter and a length,  $L_g$ , that can be adjusted with a sliding short from 60-160 mm (B). The sliding short simply consists of an inner base plate that is connected to an adjustable screw (C). The coupling probe, which actually directs the microwave energy into the cavity, is also an adjustable parameter (D). The probe distance into the cavity

**TOP COLLAR**

COLLAR MATERIAL: Aluminum

FITTINGS: Stainless Swagelok and Ultra-Torr

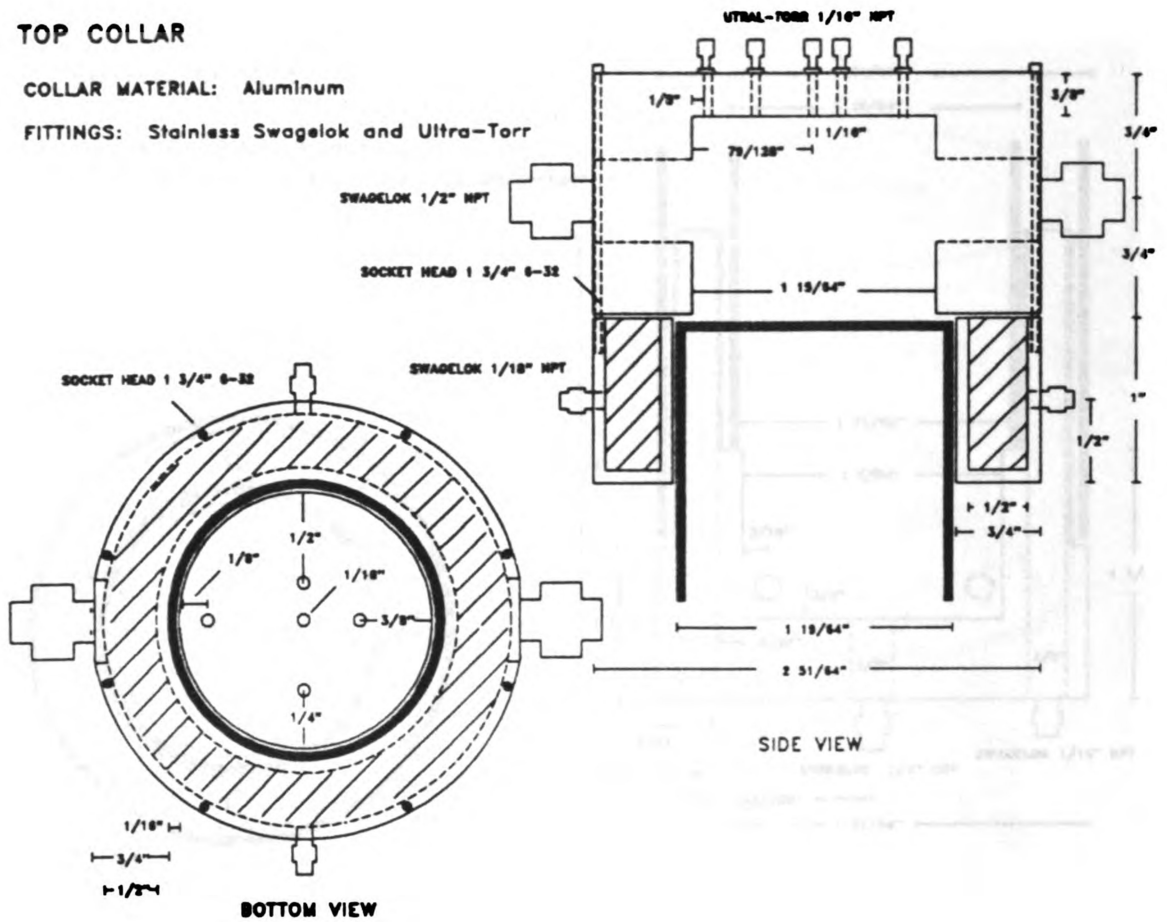


**Figure 3.4 Top Collar Design**

**BOTTOM COLLAR**

**COLLAR MATERIAL:** Aluminum  
**FITTINGS:** Stainless Swagelok and Ultra-Torr

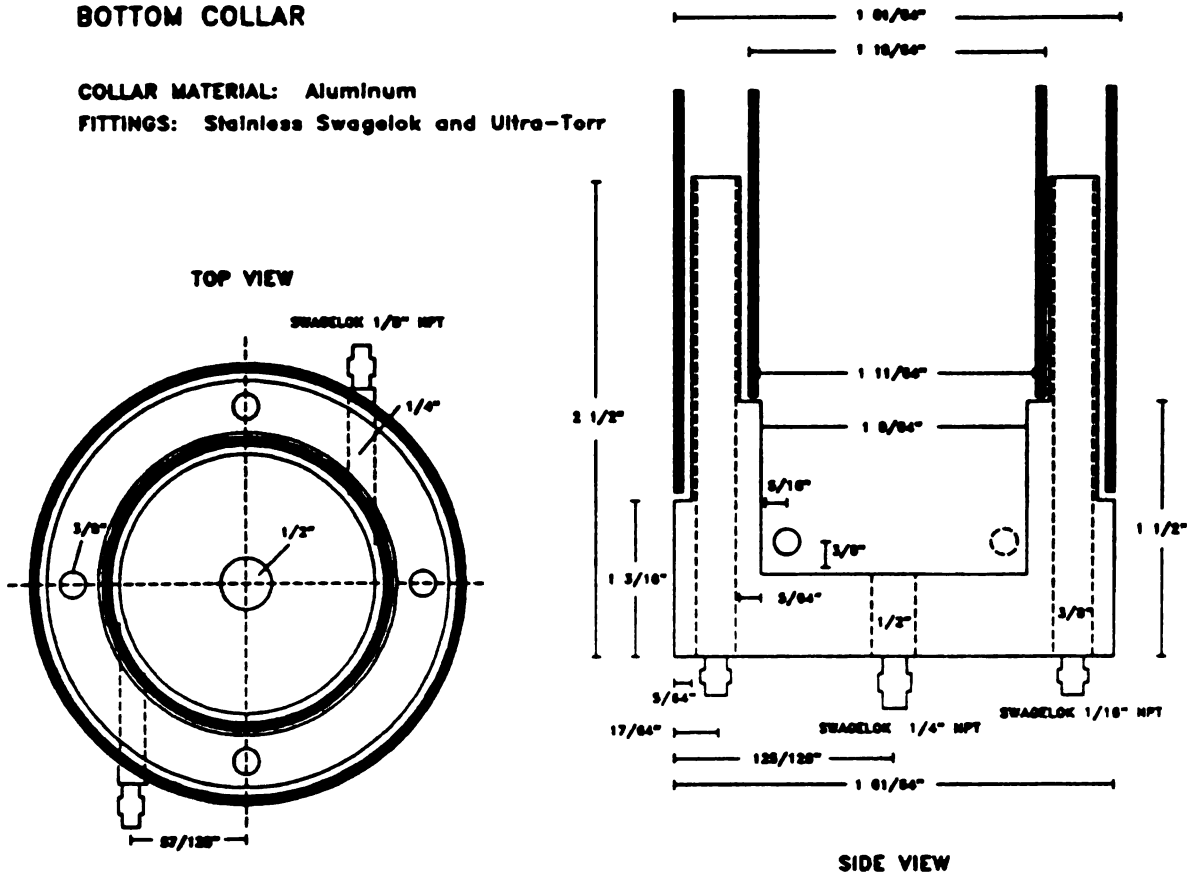


**Figure 3.5 Bottom Collar Design**

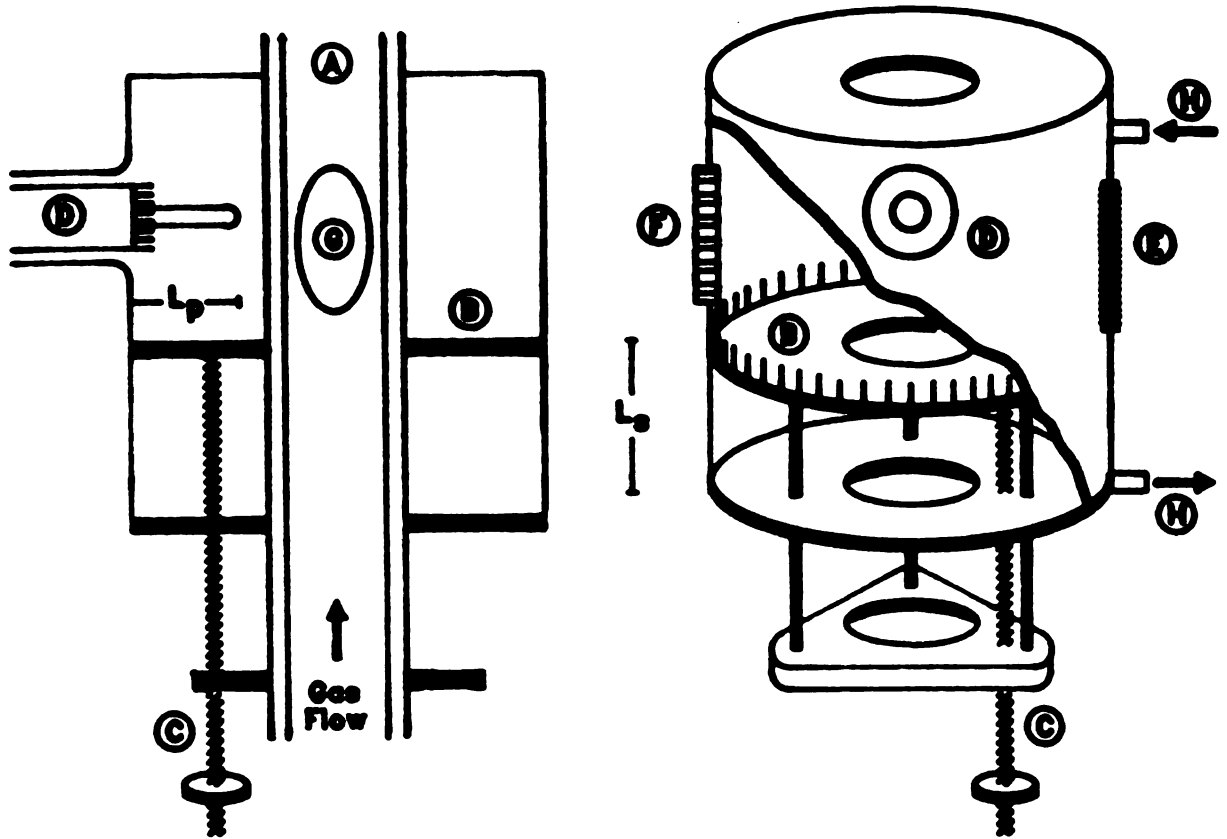


Figure 3.6 Microwave Resonant Cavity

is represented by  $L_p$ . By adjusting the sliding short and coupling probe, several resonance modes can be supported. The resonance modes represent eigenvalues of the solution to Maxwell's equations<sup>22</sup>. The  $TM_{012}$  resonant mode was exclusively used in these investigation.

The resonant cavity must be completely free from microwave leakage, but must also contain ports for diagnostics. Two ports are positioned  $90^\circ$  from the coupling probe to allow for photographic and spectroscopic investigations. The photographic port (E) uses fine mesh screen to prevent the propagation of microwave energy. The spectroscopic port (F) consists of holes drilled within a brass block that are small enough to stop microwave leaks but large enough for the fiber optic placement. These ports are designed to allow for visible access to the plasma region (G) in the  $TM_{012}$  mode. Copper tubing is welded around the top, bottom, and sides of the cavity for calorimetric investigations (H).

### 3.6 Spectroscopic System

The spectroscopic system consists of a 1 m fiber optic cable, illustrated in Figure 3.7, with a specially fabricated Macor ferrule to withstand the heat and microwave interactions. This termination is 15 mm from the plasma region (separated by annulus), which produces approximately 3 mm of plasma cross-section to be observed. The exiting termination is stainless steel and is

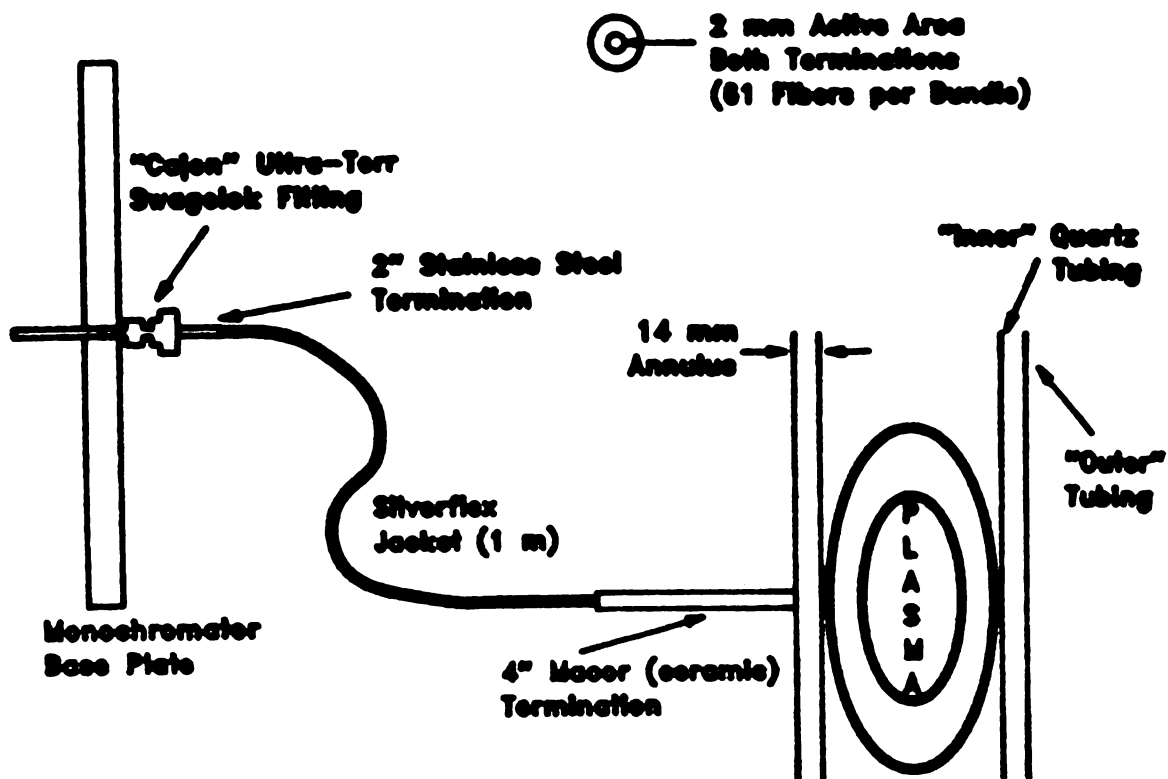


Figure 3.7 Fiber Optic Cable with Terminations

connected to the monochromator by a "Cajon" ultra-torr fitting. The sheath is made from Silverflex and contains a 1 mm active area of quartz fibers. The cable can be positioned at various radial and axial points within the cavity. This fiber optic system greatly improved spectral resolution and sensitivity over the glass lenses previously used to focus the emissions by reducing signal noise. A comparison of a helium plasma spectra obtained with and without the fiber optic system, found in Figure 3.8, illustrates the noise reduction.

As illustrated in Figure 3.9, a port (A) within the microwave cavity houses the Macor termination of the fiber optic (B). The stainless steel termination is connected to a McPhearson Model 216.5 Half Meter Scanning Monochromator (C) and photomultiplier detector (D). The entrance and exit slits were optimized at 0.1 and 0.15 mm, respectively. Most of the spectral observations were made between 3000-7000 Å. A Hewlett-Packard Model 6110A DC power supply (E) provided a high voltage of 900 volts to the photomultiplier tube. The PMT output was processed through a Keithly Model 616 digital electrometer (F), sent to a Metrabyte data acquisition and control system (G), and recorded on an AT computer (H).

The spectroscopic system was calibrated by two different methods. The proper alignment of the monochromator is critical for the desired spectral resolution and location of obscure emission lines. This was accomplished with a mercury source whose spectrum is accurately known. A second calibration procedure was required to develop a numerical constant for the photomultiplier

## Helium Plasma Spectra Generated With and Without Fiber Optic Attachment

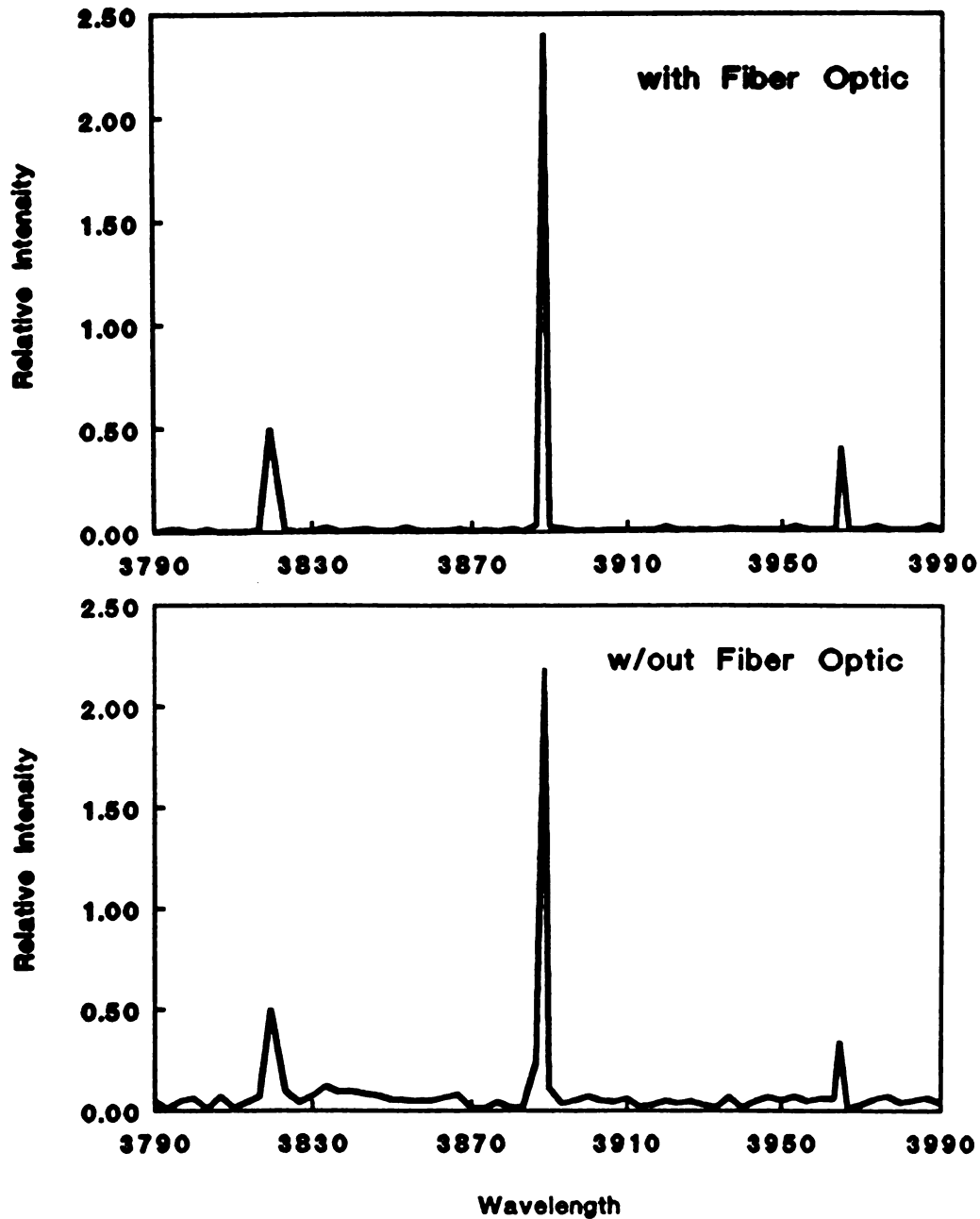
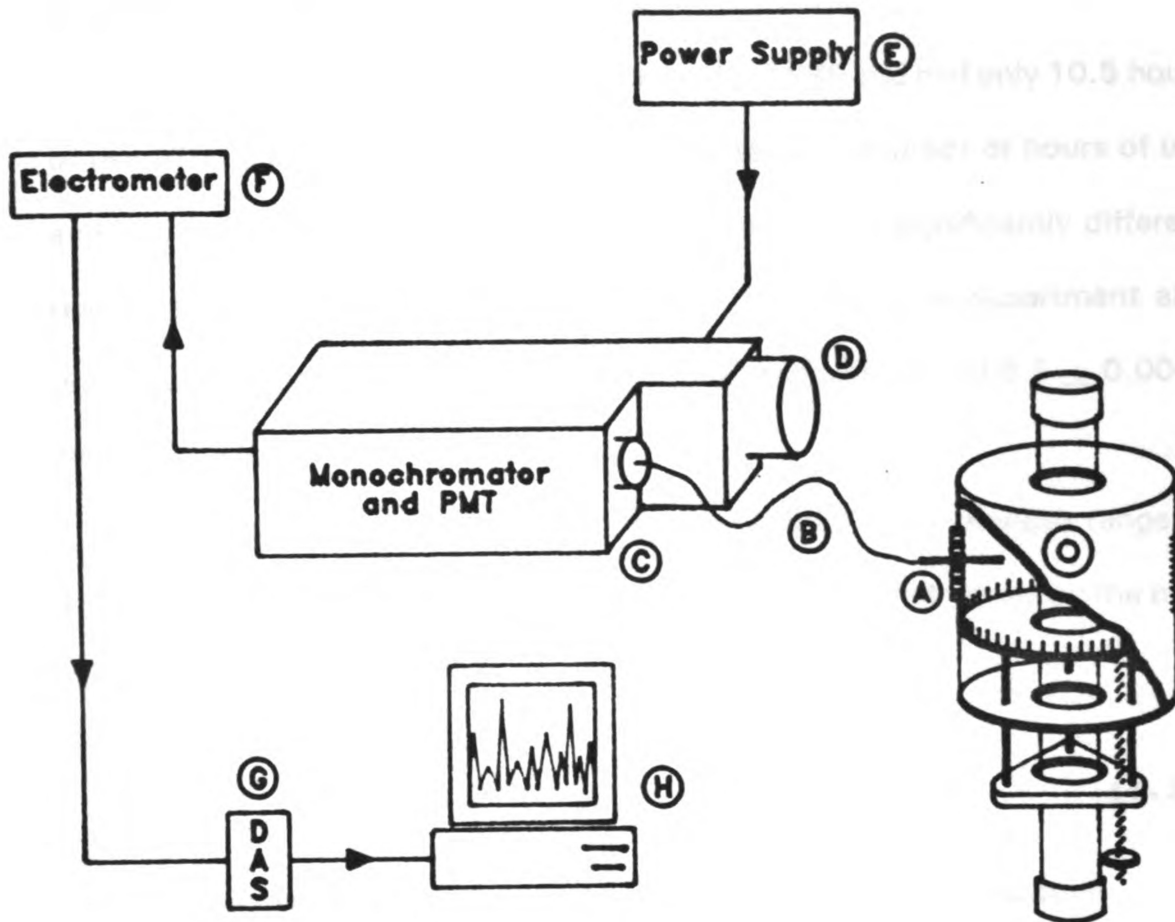


Figure 3.8 Helium Spectra Obtained With and Without the Fiber Optic Cable



**Figure 3.9** Spectroscopic System

response. The constant is referred to as the spectral response function and requires the use of a precisely calibrated tungsten source.

An NBS calibrated tungsten lamp was borrowed from the chemistry department as a standard of spectral irradiance. The lamp, made by Optronics Laboratories, Inc. Model 245C, was calibrated in 1989 and had only 10.5 hours of use. The tungsten lamp normally used contained hundreds of hours of use and was last calibrated in 1982. The older lamp had a significantly different response function than did the new lamp. The chemistry department also provided a dedicated power supply that maintained a current of  $6.5 \pm 0.0001$  amps.

The response calibration was conducted over a wavelength range of 2500-8000 Å. The spectral response function,  $R_\lambda$ , was determined by the non-dimensionalized equation

$$R_\lambda = \left[ \frac{I_{measured}}{I_{known}} \right]_{\lambda=5900 \text{ Å}} \times \left[ \frac{I_{known}}{I_{measured}} \right]_\lambda \quad (3.1)$$

The spectral response function was extended with linear interpolation

$$P_1(x) = f_o + (x - x_o) \left[ \frac{f_1 - f_o}{x_1 - x_o} \right] \quad (3.2)$$

to calculate the spectral response function for specific wavelengths. The results of this calibration procedure are listed in Table 3.1. The wavelength,  $\lambda$ , is in angstroms and the known and measured intensities,  $I_k$  and  $I_M$ , are in nanoamps. This function is incorporated into all spectroscopic calculations.

Table 3.1 Tungsten Calibration Data for Spectral Response

$\lambda$	$I_K$	$I_M$	$R_\lambda$	$\lambda$	$I_K$	$I_M$	$R_\lambda$
2500	0.389	489	0.1405	5300	303.6	227571	0.2358
2600	0.684	489	0.2470	5400	326.8	184259	0.3134
2700	1.190	734	0.2865	5500	350.0	146331	0.4227
2800	1.950	979	0.3521	5600	375.0	125042	0.5300
2900	3.010	1468	0.3623	5700	400.0	109870	0.6434
3000	4.430	2447	0.3199	5800	425.0	94210	0.7973
3100	6.750	4405	0.2708	5900	450.0	79528	1.0000
3200	9.070	7341	0.2184	6000	475.0	64846	1.2945
3300	13.21	10767	0.2168	6100	497.2	50898	1.7264
3400	17.36	15906	0.1929	6200	519.4	38173	2.4046
3500	21.50	23002	0.1652	6300	541.6	27162	3.5239
3600	27.85	32056	0.1535	6400	563.8	18353	5.4292
3700	34.20	42578	0.1420	6500	586.0	11501	9.0047
3800	43.83	56036	0.1382	6600	607.2	7096	15.122
3900	53.47	72187	0.1309	6700	628.4	4160	26.697
4000	63.10	87847	0.1269	6800	649.6	2447	46.916
4100	77.28	108647	0.1257	6900	670.8	1468	80.744
4200	91.46	131649	0.1228	7000	692.0	979	124.94
4300	105.6	152693	0.1222	7100	709.0	489	256.03
4400	119.8	175695	0.1205	7200	726.0	489	262.17
4500	134.0	196494	0.1205	7300	743.0	489	268.31
4600	154.0	211910	0.1284	7400	760.0	489	274.44
4700	174.0	225369	0.1364	7500	777.0	489	280.58
4800	194.0	231976	0.1478	7600	788.8	489	284.84
4900	214.0	238093	0.1588	7700	800.6	489	289.11
5000	234.0	242742	0.1704	7800	812.4	489	293.37
5100	257.2	242498	0.1874	7900	824.2	489	297.63
5200	280.4	243232	0.2037	8000	836.0	489	301.89

## CHAPTER 4

---

### *Plasma Dimensional and Quality Analysis*

#### 4.1 Photographic Method of Analysis

One of the simplest and most useful methods of observing plasma behavior is through photography. Conventional snapshot photography is particularly useful in the study of plasmas where rapid changes in luminosity, size, and shape occur. These measurements can aid in the modeling of heat transfer and chemical processes within the plasma region<sup>23</sup>.

The plasma dimensions and quality (which refers to the plasma stability, shape, and color) were determined by photographing the discharge at a known distance with 35 mm color slide film. The image was then projected against a 100x100 mm grid, also photographed from the same distance, and analyzed for size, color, and shape.

A Pentax MX 35 mm camera, mounted on a tripod, was used in these investigations. It was found that low-speed film (100 ISO) combined with a rapid shutter speed (1/250 s) and f1.7 aperture, produced the clearest slides.

Further improvement was made by mounting three Hoya dioptic lenses (sizes +1, +2, and +4) to the camera lens. The total distance from the end of the dioptic lenses to the plasma was 88 mm. Each analysis was conducted in triplicate for improved accuracy.

#### 4.2 Plasma Overall Volume

Previous researchers have devoted considerable effort to understanding deviations in the size and shape of single-component plasmas with pressure, power, and gas flow rate. These characteristics have been monitored in both the inner and outer regions of the plasma which are referred to as the strong and weak ionization regions, respectively. Leonard and other researchers, however, suggests that caution be exercised in this interpretation of the luminosity gradients of the plasma as distinct boundaries<sup>24</sup>.

The dimensional analyses conducted most recently have utilized the single-component gases used previously with additional emphasis directed towards overall volumes compared to those of a binary mixture. The cavity system, quartz containment, and dimensional measuring technique has also been altered to improve sensitivity and accuracy.

The binary mixture used in these investigations consisted of 50% (by volume) helium and nitrogen. All experiments were conducted by mixing the gases prior to interacting with the microwave energy. Observations revealed

that when the composition was altered following plasma formation there was only slight apparent volume change. This possibly indicates that the plasma acts as a control volume with well-defined boundaries that allow little, if any, mass transport into or out of the system.

The nitrogen and argon plasmas in these investigations were shaped similarly to an oblate ellipsoid. Assuming axial symmetry the volumes were easily found by the equation

$$V_e = \frac{4\pi}{3} \left(\frac{L}{2}\right) \left(\frac{W}{2}\right)^2 \quad (4.1)$$

where:

$$\begin{aligned} V_e &= \textit{ellipsoidal volume} \\ L &= \textit{plasma length} \\ W &= \textit{plasma width} \end{aligned}$$

Helium plasmas exhibited an indentation at their center and the volume,  $V_d$ , was therefore calculated as two dumbbells connected to a cylinder or

$$V_d = 2 \left[ \left( \frac{4\pi}{3} \right) \left( \frac{W}{2} \right)^3 \right] + \pi \left( \frac{W}{2} \right)^2 \left( \frac{L}{2} \right) \quad (4.2)$$

#### 4.2.1 Pressure Dependence

Single component and binary mixture plasmas were generated and evaluated as a function of pressure from 20 - 1000 Torr. The results are illustrated in Figure 4.1. The parameters held constant are listed in Table 4.1

### Plasma Overall Volume Function of Pressure

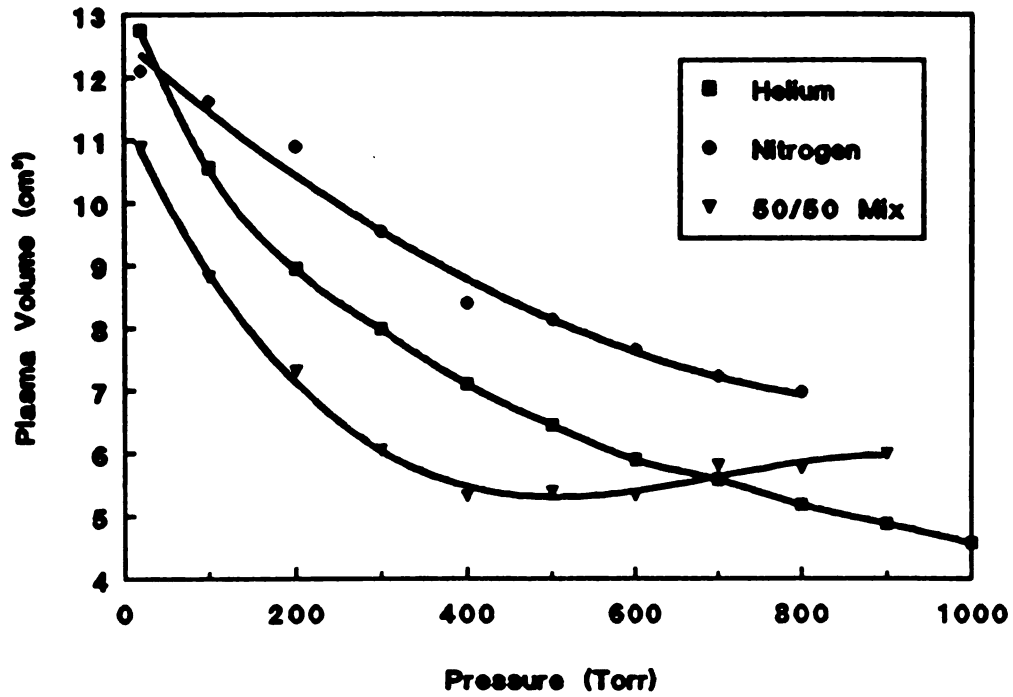


**Figure 4.1** Overall Plasma Volumes for Helium, Nitrogen, and Mixture as a Function of Pressure

below.

**Table 4.1 Plasma Volume Conditions**

<b>Net Power Input</b>	<b>= 240-250 W</b>
<b>Total Gas Flow Rate</b>	<b>= 500 sccm</b>
<b>Equilibration Time</b>	<b>= 15 min.</b>
<b>Air Coolant Rate</b>	<b>= 2 scfm</b>
<b>Water Coolant Rate</b>	<b>= 5.75 mL/s</b>
<b>Film Speed</b>	<b>= 100 ISO</b>
<b>Shutter Speed</b>	<b>= 1/250 s</b>
<b>Aperture</b>	<b>= f1.7</b>
<b>Resonance Mode</b>	<b>= TM<sub>012</sub></b>

The overall volumes of the single-component plasmas coincide well with previous work<sup>23,25</sup>. A simple polynomial was used to represent the trends for these plasmas. The volume decreases exponentially with increasing pressure. This phenomenon is expected in theory since the mean free path at the lower pressures is large enough to allow high-energy interactions between the neutral and electron species. Though the collisional frequency increases linearly with pressure, the mean free path decreases exponentially thus preventing sufficient energy exchange at the higher pressures. Consequently, the rate of ion-electron recombination and the percent of ionization decreases with the higher pressures forming a smaller volume.

The nitrogen plasma decreases at a slower rate than does the helium plasma. This is in part due to the sluggish nature of the larger molecule and thus, shorter mean free path. The other reason for this slow response to the

pressure change is the diatomic structure of nitrogen. The additional energy modes require greater energy for ionization and the plasma is thus not as susceptible to environmental alterations, with the exception of power input.

The binary mixture exhibited interesting characteristics indigenous to both components and was fitted to a spline for better representation. At lower pressures, the same abrupt change occurred as with helium but the volume was slightly smaller than that of helium which contradicts logic for this mixture. The slope approaches unity at moderate pressures and increases towards the nitrogen curve at higher pressures. This unusual trend is difficult to explain theoretically since the slow evolution of the nitrogen ions would be expected to occur at the lower pressures where the mean free paths would be at their maxima. Perhaps the helium species obstruct the collisional processes necessary for the molecular dissociation of nitrogen.

#### 4.2.2 Gas Flow Dependence

The overall volumes were determined as a function of gas flow rate from 50 - 500 sccm maintaining the same parameters as those found in Table 4.1, with the exception of power (275 W). The pressure was held constant at 400 Torr. As revealed in Figure 4.2, the flow rate has less influence on the volume that does the pressure. The volume decreases with increased flow rate which indicates that the smaller number of atoms allow greater energy and mass

### Plasma Overall Volume Function of Gas Flow Rate

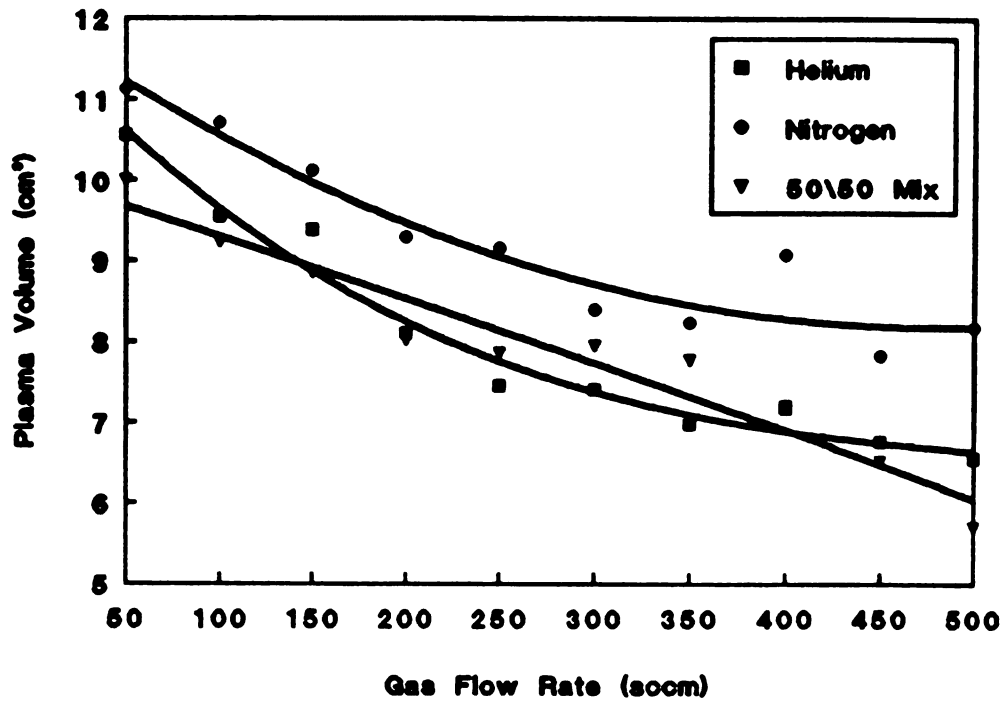


**Figure 4.2** Overall Plasma Volumes for Helium, Nitrogen, and Mixture as a Function of Gas Flow Rate

transfer due to fewer obstructions. In other words, fewer collisions take place but each collision occurs with greater energy than would occur with an increased number of atoms.

As with the pressure dependence results, the diatomic nitrogen plasma undergoes a much more gradual volume change than does the monatomic helium plasma. The mixture exhibited the same gradual change as that of the pure nitrogen but the magnitudes in volume were closer to those in the helium plasma.

#### 4.2.3 Composition Dependence

Earlier experiments with mixtures of helium and nitrogen revealed an inflection occurring at 70% helium suggesting that the 1:2 (33%/67%) atom ratio was the cause. If this was indeed the case, then two monatomic elements would fail to show this inflection. Argon was introduced into the experiment to better assess the relationships between monatomic/diatomic and monatomic/monatomic mixtures. These results are illustrated in Figure 4.3.

In general, the maxima occurred for the pure component extremes with the minima in between. Pure argon exhibited the largest plasma volume, followed by nitrogen and helium. The argon/helium mixture lost its definite ellipsoidal shape at 70% and was transformed into a mass of filaments but its trend seemed to be similar to that of nitrogen/argon.

### Plasma Overall Volume Function of Composition (by % volume)

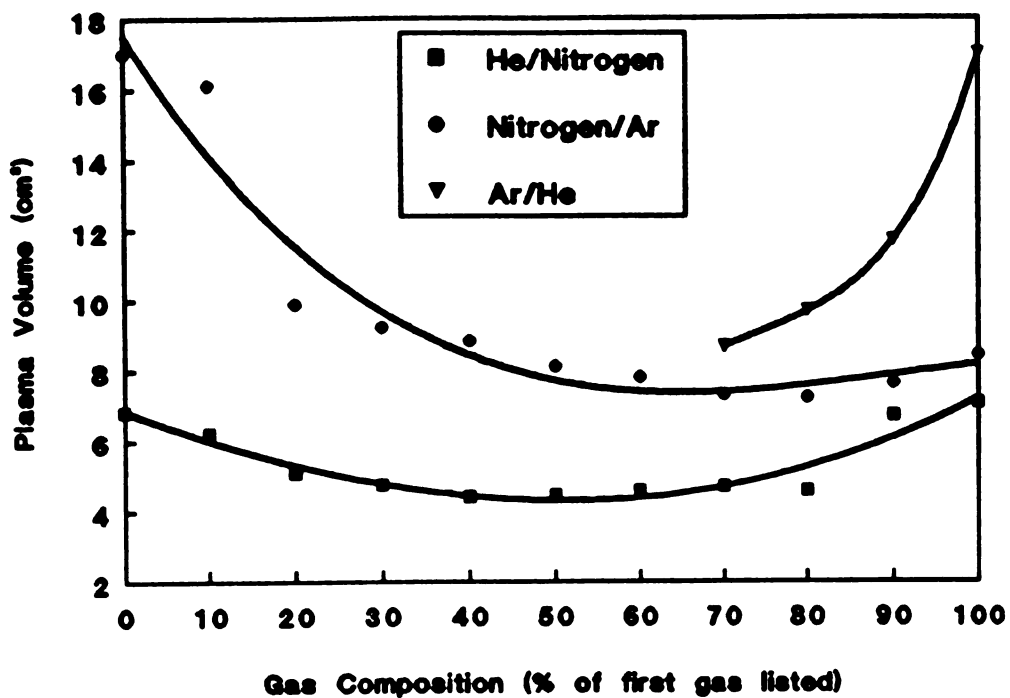


Figure 4.3 Overall Plasma Volumes as a Function of Composition (by volume)

The inner volumes of the plasma mixtures followed the same general trend as the overall volumes. These volumes, along with the plasma color transformations, are summarized in Table 4.2 for a helium and nitrogen plasma.

**Table 4.2** Inner and Overall Volumes and Color Transformations for Helium/Nitrogen Plasma

Gas Composition	$V_0$ ( $\text{cm}^3$ )	$V_1$ ( $\text{cm}^3$ )	$V_1$ (%)	Plasma Color	
				Outer	Inner
100% He	9.35	2.58	27.6	blue	white
90% He/10% N <sub>2</sub>	3.87	0.12	3.1	blue/pink	white/pink
80% He/20% N <sub>2</sub>	2.91	0.17	6.0	bright pink	light pink
70% He/30% N <sub>2</sub>	2.03	0.24	11.8	bright orange	light orange
60% He/40% N <sub>2</sub>	3.68	0.76	20.7	orange	light orange
50% He/50% N <sub>2</sub>	3.81	1.17	30.8	orange	light pink
40% He/60% N <sub>2</sub>	4.26	1.01	23.6	light pink	light pink
30% He/70% N <sub>2</sub>	4.81	1.02	21.1	light pink	light pink
20% He/80% N <sub>2</sub>	6.08	1.32	21.7	light pink	pink/white
10% He/90% N <sub>2</sub>	7.26	1.89	26.0	pink	white
100% N <sub>2</sub>	7.96	2.31	29.0	pink	white

The behavior of these mixtures suggests that the ionization potentials,  $I_A$ , for the three components do not contribute significantly to deviations of the plasma volume ( $I_{N_2} > I_{He} > I_{Ar} > I_N$ ). The size of neutral species, however, seem to be the controlling factor which again goes back to mean free path and the collisional processes.

#### 4.2.4 Power Dependence

The dependence of microwave power on plasma volume was determined as a function of gas flow rate maintaining identical conditions as those found in Table 4.1. This investigation was conducted on pure helium gas at a net power of 200 and 300 W. These results are found in Figure 4.4.

Helium plasma volume decreases with increased flow rate at higher power inputs as with above experiment. However, at lower power levels the volume decreases slightly. This confirms the hypothesis that power "saturation" does occur with the helium plasma. This investigation confirms that power levels have a significant influence over plasma size.

#### 4.3 Gas-Surface Interactions

The effects of recombination greatly influence variations in the size and shape of the plasma region. The recombination of ions can be catalyzed by virtually all species and surfaces to which the ions are exposed. At low pressures, this recombination is dominated by interactions with the containment walls, which results in the plasma expansion of Figure 2.3. The ability of a surface to catalyze recombination can be expressed as the fraction of atoms striking the surface that recombine, known as the wall recombination coefficient (WRC). Metals have the highest wall recombination coefficient with

### Plasma Overall Volume Functions of Gas Flow Rate and Power

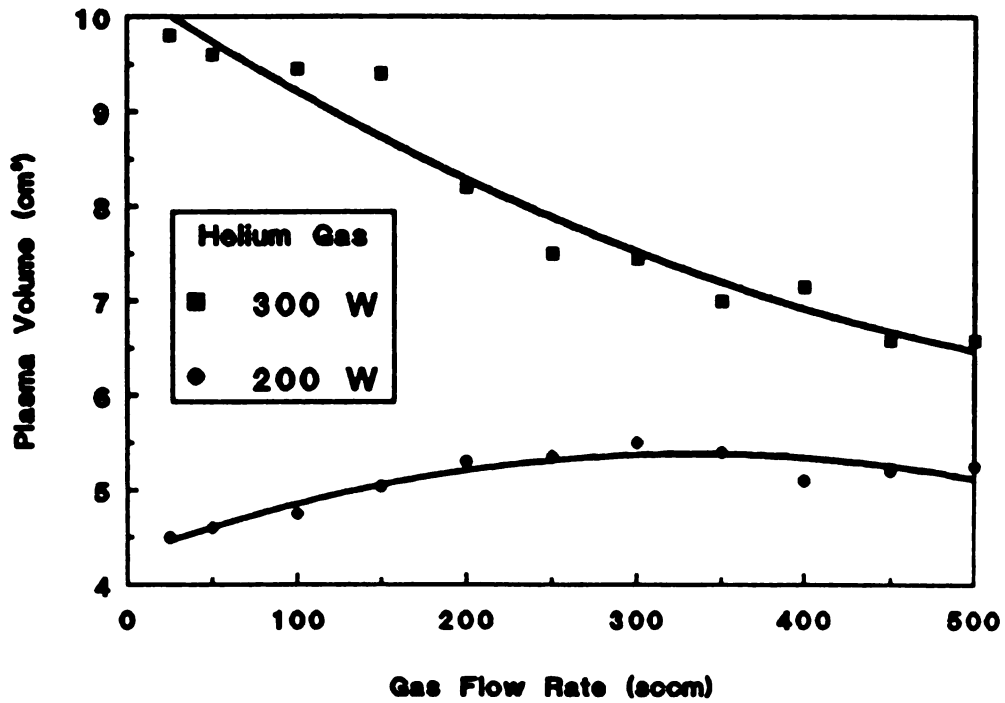


**Figure 4.4** Overall Plasma Volume for a Helium Plasma at 200 and 300 W as a Function of Gas Flow Rate

platinum equal to 1. Quartz and pyrex glass have a WRC of approximately  $10^{-3}$  and  $10^{-4}$ , respectively<sup>26</sup>.

There are several expressions that describe the rate at which this wall recombination occurs. Chapman, Finzel, and Hawley recommend the following<sup>27</sup>:

$$r_v = A_p k_s [C] \quad (\text{mol/s}) \quad (4.3)$$

where the plasma surface area and molar concentration are represented by  $A_p$  and  $C$ , respectively. The surface reaction rate constant,  $k_s$ , is related to the wall recombination coefficient by

$$k_s = WRC \left[ \frac{V_m}{4} \right] \quad (4.4)$$

where  $V_m$  is the average velocity of the gas molecule. The WRC for fused quartz can be accurately determined from a fit to an Arrhenius plot as a function of wall temperature,  $T_w$ , by the expression

$$WRC = 0.0566 \exp\left(\frac{-1148.3}{T_w}\right) \quad (4.5)$$

Using this expression, the assumption of thermal equilibrium must be made so that the wall temperature is the same as the gas temperature. Since the temperature of the wall is primarily due to the highly exothermic recombination reactions that occur at the wall, it is unlikely that the gas temperature equals the wall temperature<sup>12</sup>. It appears that the energy transfer due to these wall reactions increase with an increase in pressure and a decrease in gas flow rate.

This is easily explained through the long residence times which creates a more intense plasma.

The measured size of the plasma has been incorporated into Equation 4.3, which complicates the computations since the plasma area changes as a function of pressure. The effects of the plasma area can be determined by using a constant value in Equation 4.3 and comparing its results with those obtained with another expression. This will be accomplished by using the equation derived from Wareck for the wall recombination rate, which includes the random velocity term from kinetic theory,  $V_r$ ,<sup>28</sup>

$$r_w = WRC \left[ \frac{V_r}{2D} \right] \quad (\text{collisions/s}) \quad (4.6)$$

where:

$$V_r = \left[ \frac{8kT}{\pi m} \right]^{\frac{1}{2}} \quad (m/s)$$

Equation 4.6 excludes the wall temperature, so the assumption made in the former expression that  $T_w = T_g$  is eliminated. Another advantage of Wareck's equation is that it doesn't incorporate the plasma area, so a comparative analysis can be made between the various gases under evaluation. However, Wareck's equation does place a strong dependence on the speed of the gas molecules which is influenced by the pressure. The random velocity values are only slightly different from the average velocities used in Equation 2.3. Figure 4.5 compares Equations 4.3 and 4.6 on the theoretical wall recombination rate

## Wall Recombination Rate vs. Temperature Effects of Area on WRR

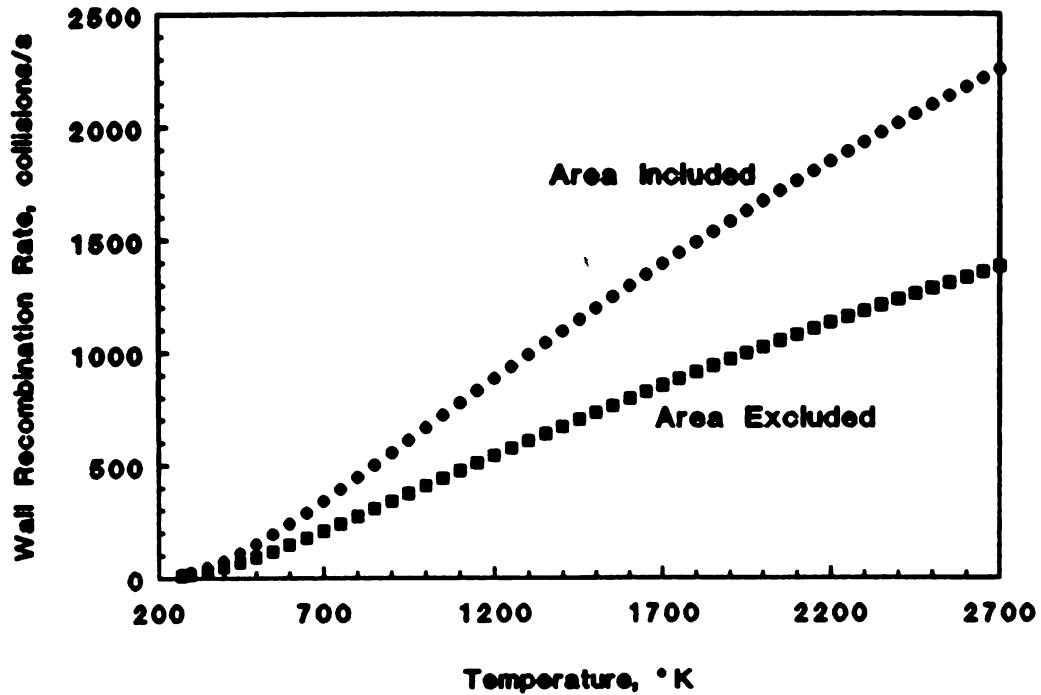


Figure 4.5 Comparison of Wall Recombination Rate Equations for a Helium Plasma as a Function of Gas and Wall Temperatures



for a helium plasma as a function of temperature. The curve marked "area included" incorporates Equation 4.3 and assumes a constant pressure and corresponding plasma area ( $A_p = 20 \text{ cm}^2$ ). The other curve, marked "area excluded", utilized Equation 4.6 where plasma area was irrelevant. This figure reveals that the quantities do converge at lower temperatures. The experimental gas temperatures are estimated to be approximately  $1000^\circ\text{K}$  where the figure shows only a 25% separation difference.

## CHAPTER 5

---

### *Calorimetric Investigations*

#### 5.1 Macroscopic Energy Balance

As mentioned earlier, calorimetric evaluations are conducted to describe the energy absorption and distribution of the system. There are two systems used in this evaluation. Macroscopically, the thermodynamic system is the microwave resonant cavity found in Figure 2.1 which encompasses the quartz containment. This system is used to quantify the energy distribution from the microwave power source. Approximately 80% of the total microwave energy is actually coupled into the plasma since a portion of the energy is reflected back to the source and a portion is lost to the cavity walls through radiation.

The differential form of the general energy balance is<sup>15</sup>

$$\frac{d}{dt} \left[ U + M \left( \frac{v^2}{2} + \psi \right) \right] = \sum_k \dot{M}_k \left( \hat{H} + \frac{v^2}{2} + \psi \right)_k + \dot{Q} + \dot{W} \quad (5.1)$$

For an open steady-state system and ignoring the kinetic and potential terms since the gas velocity is much less than sonic, the energy balance becomes

$$\sum \dot{M}_k \hat{H}_k + \dot{Q} + \dot{W} = 0 \quad (5.2)$$

Since no work is done to or from the system, the total heat is defined as

$$\sum \dot{M}_k \hat{H}_k = -\dot{Q} \quad (5.3)$$

and upon rearranging yields the energy balance around the resonant cavity system

$$E_{source} = E_{gas} + E_{air} + E_{water} + E_{radiation} \quad (5.4)$$

where:

$$E_{source} = P_i + P_r$$

$$E_{air} = \int_{T_0}^T C_{p,air} \dot{M}_{air} dT_{air}$$

$$E_{water} = \int_{T_0}^T C_{p,water} \dot{M}_{water} dT_{water}$$

$P_i$  and  $P_r$  are the power incident and reflected, respectively, measured by power meters. The reflected power is the power lost due to improper resonant modes that literally reflect a portion of the power back to the source. The incident power is the net power that is transferred to the cavity. The air flows through an annulus surrounding the inner quartz tubing and serves as a coolant to prevent high temperatures from melting the discharge tube. The water circulates around the resonant cavity and accounts for the energy lost to the

cavity wall. The flow rates of the air and water are controlled through calibrated flow meters and their temperature changes are determined by thermocouples positioned at the inlets and outlets.

The flow rates have incorporated density corrections into their calculations to account for changes in temperature<sup>29</sup>. For air this gives

$$\dot{M}_{air} = 0.01627 F_{air} \rho_{air} \quad (5.5)$$

where:

$$\rho_{air} = 1.2929 \left( \frac{273.13}{T} \right) \left( \frac{B - .3783e}{760} \right), \frac{g}{L}$$

with T, B, and e representing the temperature (°K), atmospheric pressure (mm Hg), and moisture vapor pressure in air (mm Hg), respectively.

For water this gives

$$\dot{M}_{water} = 0.0555 F_{water} \rho_{water} \quad (5.6)$$

where:

$$\rho_{water} = 1.001826 - 0.00017 T, \frac{g}{cm^3}$$

with the temperature in degrees Celsius. Combining Equations 5.4 - 5.6 give the following single-variable expression for the calculation of the amount of energy actually transferred to the plasma:

$$E_{gas} = P_i - P_r - \int_{T_0}^T C_{p,air} \dot{M}_{air} dT_{air} - \int_{T_0}^T C_{p,water} \dot{M}_{water} dT_{water} \quad (5.7)$$

## 5.2 Energy Distribution

These experimental results represent the energy coupled to the plasma region combined with the energy that was absorbed by the air coolant. Since the air is moisture-free and thus, completely transparent to incident radiation, all energy absorbed by the air can be taken as convective losses from the plasma. The cavity system was polished with steelwool and the quartz containment was replaced thereby improving the efficiencies by approximately 20% over previous experiments.

As with the dimensional investigations, the binary mixtures were mixed prior to interacting with the microwave power since the well-defined boundaries of the plasma allow little energy transport into or out of the system. The maintained parameters for these investigations are summarized in Table 5.1.

**Table 5.1 Calorimetric Conditions**

<b>Net Power Input</b>	<b>= 275-300 W</b>
<b>Gas Flow Rate</b>	<b>= 500 sccm</b>
<b>Equilibration Time</b>	<b>= 30 min</b>
<b>Air Coolant Flow</b>	<b>= 2 scfm</b>
<b>Water Coolant</b>	<b>= 5.75 mL/s</b>
<b>Resonance Mode</b>	<b>= TM<sub>012</sub></b>

### 5.2.1 Pressure Dependence

The energy distribution was determined as a function of pressure from 20 - 700 Torr for pure helium and nitrogen and their 50/50 mixture. These results are found in Figure 5.1.

Pure nitrogen increases slightly with pressure due to the additional energy modes which incorporates a "heat sink" effect into the plasma once it is initiated. The inverse relationship between energy absorption and volume indicates that the available surface area is not the primary means of energy transfer as once thought. Helium absorbs greater power at lower pressures. At higher pressures, the decrease in ionization causes instabilities within the plasma. The helium actually seems to become "saturated" with power at the higher pressures as opposed to the nitrogen which continues to absorb energy.

The binary mixture again exhibited similar properties as each of its pure components. The energy absorbed decreases at lower pressures and begins to increase towards that of nitrogen at higher pressures.

### 5.2.2 Gas Flow Rate Dependence

The calorimetric dependence of gas flow rate was evaluated at 400 Torr under the conditions in Table 5.1. As illustrated in Figure 5.2, similar trends were obtained with variations of the flow rate as with the pressure but much

### Plasma Energy Absorption Function of Pressure

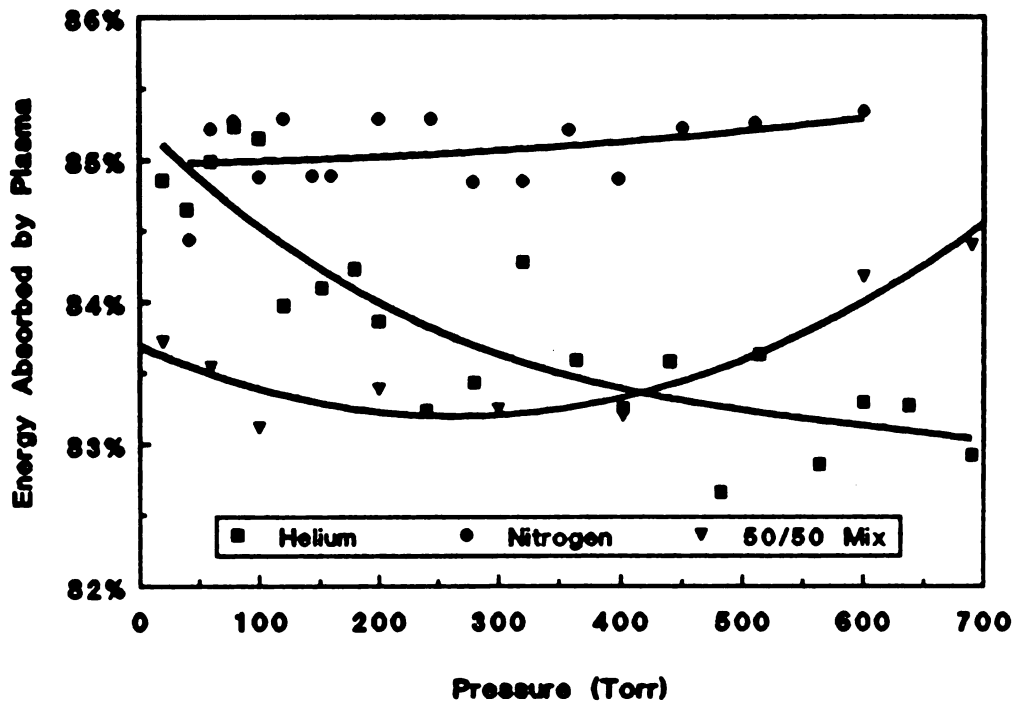


Figure 5.1 Plasma Energy Absorption for Helium, Nitrogen, and Mixture as a Function of Pressure

### Plasma Energy Absorption Function of Gas Flow Rate

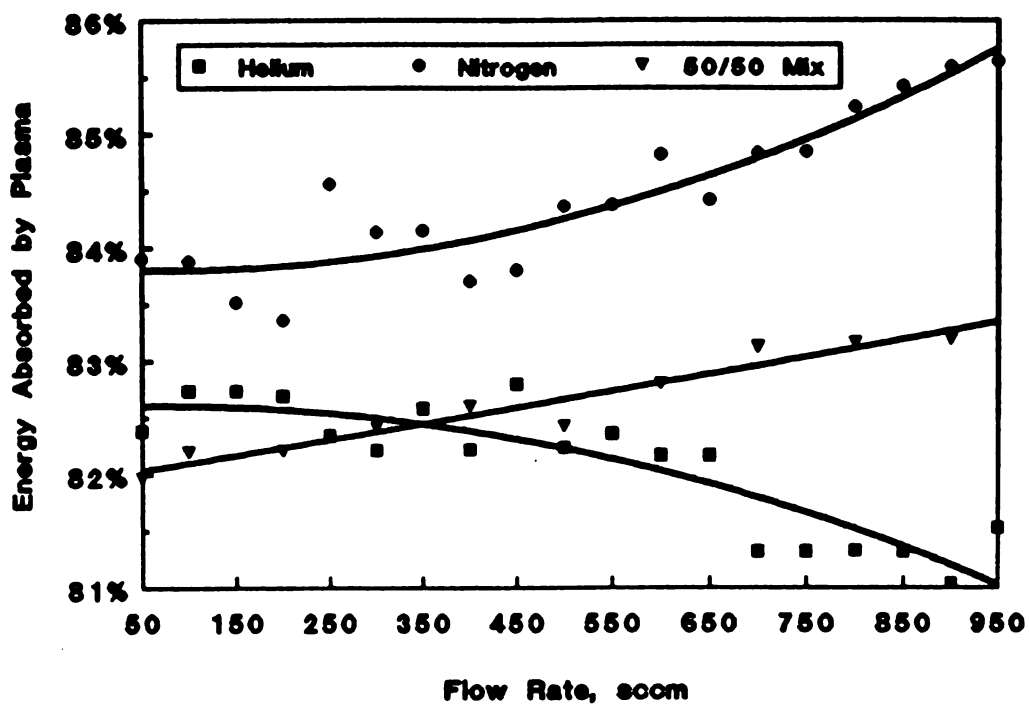


Figure 5.2 Plasma Energy Absorption for Helium, Nitrogen, and Mixture as a Function of Gas Flow Rate

more dramatically. These results differ from previous researchers work for helium who only took into account energy absorbed by the plasma and not its convective/radiative losses into the air<sup>19,25</sup>. The helium plasma again becomes saturated with energy at higher flow rates but the nitrogen continues to absorb energy.

### 5.2.3 Composition Dependence

Cubic splines, opposed to simple polynomials, were used to represent the trends found in Figure 5.3 to draw attention to the various inflections that arose. The argon/helium mixture exhibited an inverse relationship at 30% compared to that of the helium/nitrogen mixture. This inflection was thought to have occurred due to the diatomic/monatomic species.

### Plasma Energy Absorption Function of Composition (by % volume)

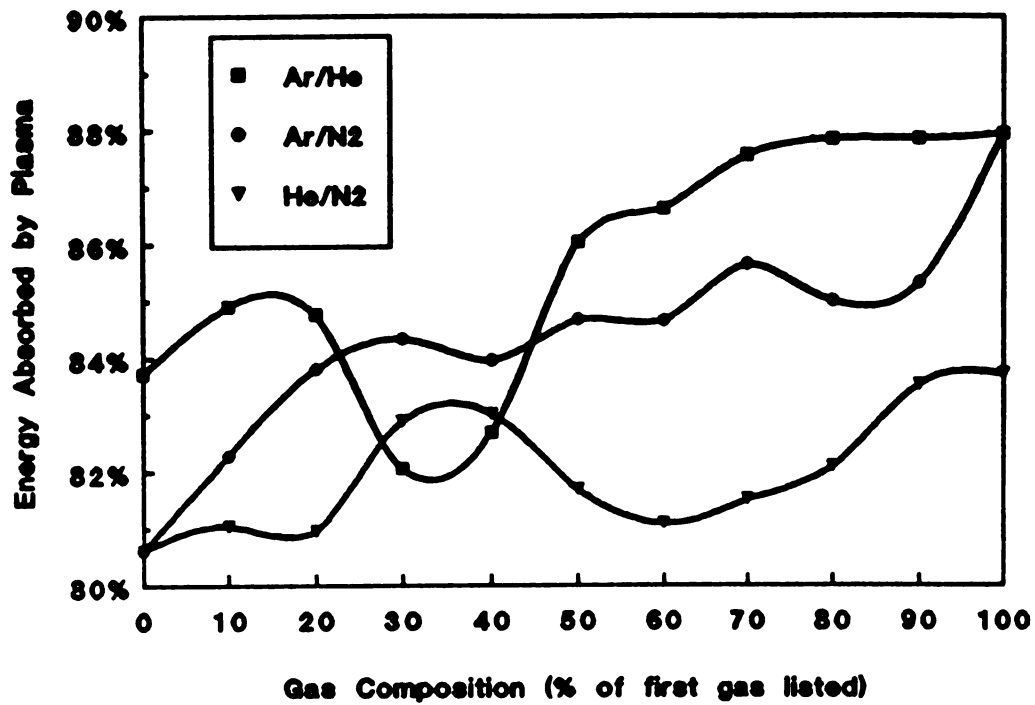


Figure 5.3 Plasma Energy Absorption as a Function of Composition (by volume)

## CHAPTER 6

---

### *Spectroscopic Investigations*

#### 6.1 Introduction

In order to optimize the thrust and improve nozzle designs and modeling, a better working understanding of the plasma processes must be acquired. Quantitative spectroscopic techniques are one of many diagnostic tools used to explain fundamental behavior within the plasma<sup>30</sup>. Spectroscopy is a prime technique, since it is nonintrusive to the plasma medium and can be applied for the measurements of species temperature, species populations, and even species velocities. Most of the spectroscopic techniques are conceptually simple, reasonably accurate, and require little peripheral instrumentation. However, when high degrees of sensitivity and spatial resolution are desired, more sophisticated techniques, such as laser-induced fluorescence, must be introduced.

The goal of these investigations is to use emission spectroscopy to obtain temperatures and concentrations of pure gases. Several methods exist

for converting emission line intensities into more useful quantities, such as temperatures and densities. These methods will be introduced along with the general theory behind spectroscopy.

## 6.2 Theory

A hot solid or melt produces a continuous emission spectrum whose simple characteristics are an attribute of the strong atomic coupling. A hot gas or plasma contains weakly coupled particles and hence many more independent degrees of freedom than does the solid or liquid. Consequently, the emission spectrum of a hot gas is more complex consisting of a few spectral lines, many lines arranged in band systems, continua, or combinations of lines, bands, and continua.

### 6.2.1 Spectroscopic Temperature Measurements

Temperature measurements obtained from spectroscopic analysis can be grouped into radiometric and spectrometric methods. Radiometric methods typically apply to "optically-thick" gases where radiation is strongly absorbed such as large flames and exhaust gases. These methods are primarily thermodynamically based and involve little reference to the mechanisms of radiation. Spectrometric methods apply to weakly absorbing or "optically-thin"

gases and entail explicit use of the quantum theory of optical spectroscopy. Spectrometric methods are commonly used for plasma diagnostics but Herzberg has shown that these two methods are equivalent in the limit as the radiative absorption goes to zero<sup>31</sup>.

A plasma contains ions and electrons in addition to the monatomic, diatomic, and polyatomic molecules that normally exists in a gas. Plasmas with temperatures up to approximately 8000°K are composed mainly of atoms and diatomic molecules, plus a few percent of ions (atomic and molecular) and electrons. Most polyatomic molecules have been completely dissociated at these temperatures.

The kinetic and internal degrees of freedom for a plasma can be regarded as a thermodynamic system, and each such system has a temperature. The kinetic or translational temperature is a measure of the mean kinetic energy of the particles. The kinetic theory of gases states that each of these particles has a velocity distribution given by the Maxwellian law, which assumes the only interactions that occur among particles are elastic collisions. In practice this condition only holds at low pressures<sup>32</sup>. The Maxwellian law is given by

$$N_v \propto v^2 e^{-\frac{1}{2}mv^2/kT} \quad (6.1)$$

The kinetic energy is related to the temperature by

$$\bar{E} = \frac{1}{2} m \overline{v^2} = \left( \frac{3}{2} \right) kT \quad (6.2)$$

and the kinetic temperature is that temperature which satisfies Equation 6.2.

Statistical physics is used to define the internal degrees of freedom of gas particles and the distribution of gas particles with respect to available internal energy states is given by the Maxwell-Boltzmann formula<sup>33</sup>

$$N_j = \frac{N g_j e^{-\frac{E_j}{kT}}}{\sum_j g_j e^{-\frac{E_j}{kT}}} \quad (6.3)$$

Since the internal degrees of freedom are nearly independent, there may be one Maxwell-Boltzmann distribution for each one. That is, one  $E_j$  may represent the energy due to internal vibration, another for rotation, and another for the energy of orbital electrons. Consequently, there may be a corresponding temperature for each energy distribution, such as vibrational temperature, rotational temperature, or electronic temperature. These temperatures are equivalent when the gas is in thermal equilibrium and are equal to the kinetic temperature.

Penner and others question the importance of non-equilibrium in spectroscopic temperature measurements<sup>34</sup>. A spectroscopic errancy that may be thought to have occurred due to non-equilibrium may turn out to be caused by self-absorption, temperature gradients, or the use of incorrect spectroscopic constants in calculating a temperature.

### 6.2.2 Degrees of Freedom

It is the internal degrees of freedom that give rise to the various kinds of spectra observed. Equations 6.1 and 6.3 are used to characterize the equilibrium state of each degree of freedom and each degree of freedom that produces observable spectroscopic radiation provides a parameter to measure temperature. The major internal degrees of freedom for an atom (or ion) with a single orbital electron is illustrated in Figure 6.1. The optical behavior is determined by the orbital electron which can be found in the ground energy level or in one of the excited levels. Each of these energy levels contains a cluster of atoms whose temperature-dependent distribution is given by Equation 6.3.

The energy of an atom or ion is continually being changed by radiation and by collisions with other particles. The absorption of radiation into an atom forces its orbital electron to make a transition to a higher energy level. Conversely, when an atom emits radiation, its orbital electron makes a transition to a lower energy level. The "excitation" transition refers to the occurrence of radiant emission or radiant absorption at a particular spectral wavelength. Combining all such transitions occurring in a gas produces the observed line spectrum of the atomic species.

The transition labeled "ionization" occurs when the energy imparted to an orbital electron by a collision or by absorption of radiation causes its total

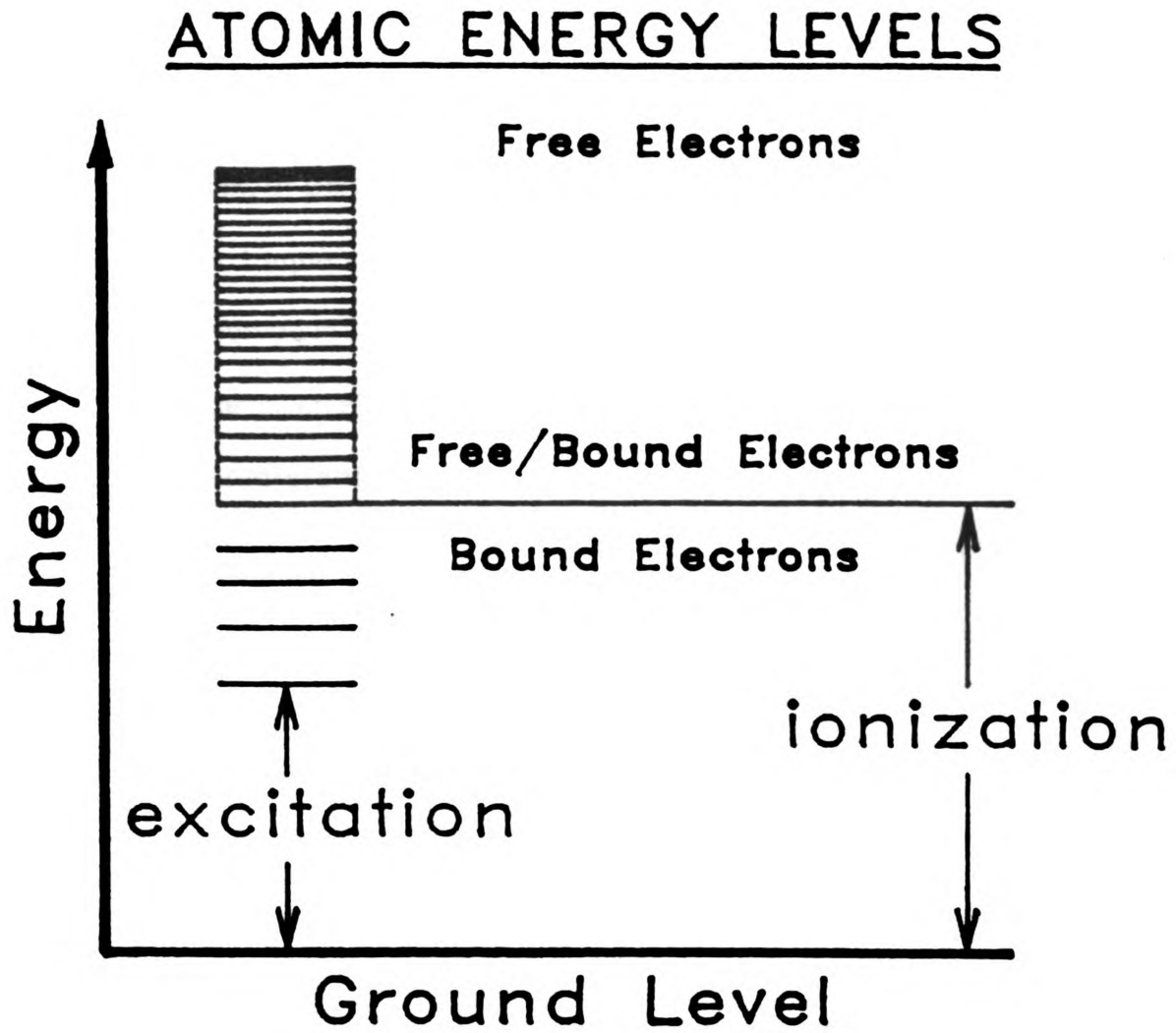


Figure 6.1 Atomic Energy Levels

energy to exceed the ionization potential of the atom. The excess energy completely removes the electron from the atom, leaving behind an ion, which has a different set of energy levels, and hence a different line spectrum, from the neutral atom. The stripped electrons may recombine with the ions to form neutral species, or they may remain free in the gas. The recombination causes a continuous frequency band in the emission spectrum to be observed<sup>33</sup>. Radiation observed in the uv-visible region is the result of electronic transitions.

The energy levels of a diatomic molecule are complicated by a potential energy curve representing the electronic state for each configuration instead of a constant energy as for the atom<sup>9</sup>. As two molecules approach each other they first attract and then repel. In discussing molecular interactions it is convenient to use plots of potential energy,  $V$ , versus intermolecular distance,  $r$ . The interaction energy is zero when the molecules are infinitely far apart. As they approach, the potential energy becomes negative because the system has a lower energy than if the molecules were completely independent. At very close distances molecules repel each other and the potential energy increases rapidly. Potential energy curves for various diatomic gases are illustrated in Figure 6.2. These curves were generated using the Lennard-Jones 6-12 equation and show that a minimum intermolecular distance exists where  $dV/dr = 0$ . These potential energy "wells" are more dependent on the size of the molecule than the collisional process.

The complexities of the energy levels of a diatomic molecule are detailed

## Typical Potential Energy Curves for Diatomic Species

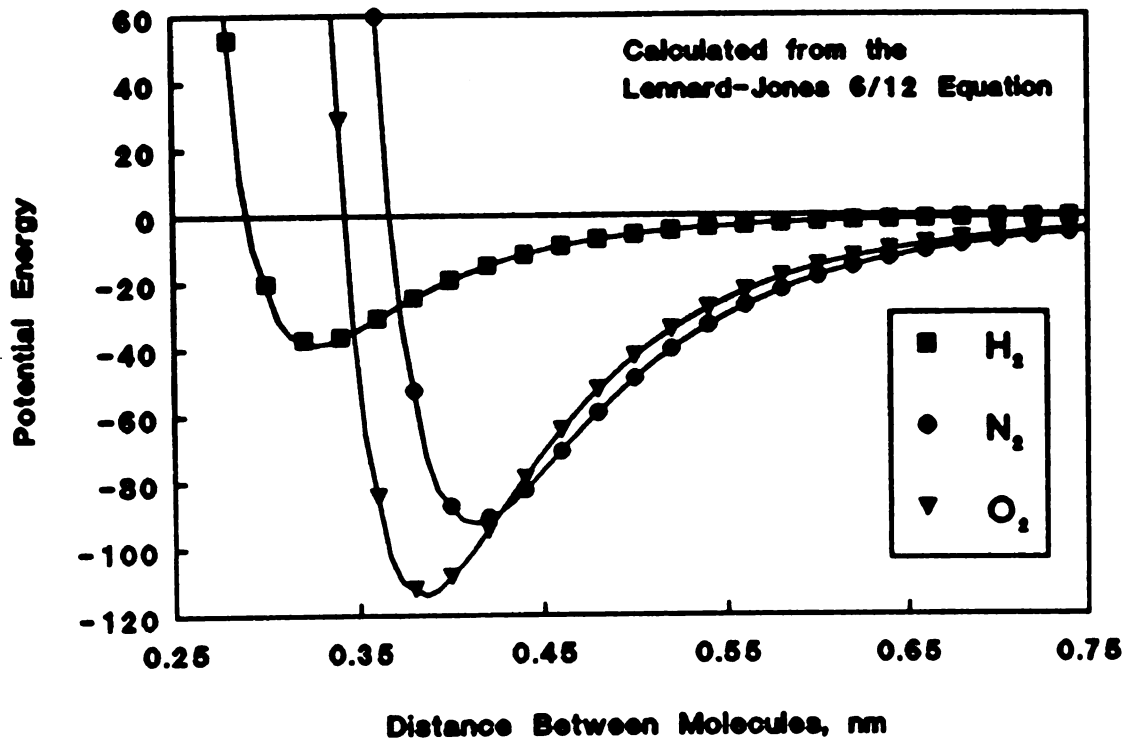


Figure 6.2 Potential Energy Curves for Diatomic Species

in Figure 6.3. The molecule has a vibrational degree of freedom along the internuclear axis, and the vibrational potential energy varies with the separation between the nuclei. In any electronic state, the molecule can vibrate along the internuclear axis and rotate about an axis perpendicular to the internuclear axis. A different set of energy states corresponds to each of these degrees of freedom.

The observed spectra for the rotational, vibrational, and electronic states are found in widely different regions. This is the result of the relative spacings between the states, with vibrational states more closely spaced than electronic states, and rotational states even more closely spaced. The energy difference between the states in a transition is proportional to the frequency of radiation. Consequently, the rotational spectra is found at the longer wavelengths of the far infrared and microwave regions, vibrational spectra in the near infrared, and the electronic in the visible and ultraviolet regions.

The kinetic degrees of freedom contributes directly to the finite width of the spectral line. Indirectly, the kinetic energy affects the spectroscopic radiation by determining the gas temperature and thereby the populations of the different energy states<sup>33</sup>.

## Degrees of Freedom for Diatomic Species

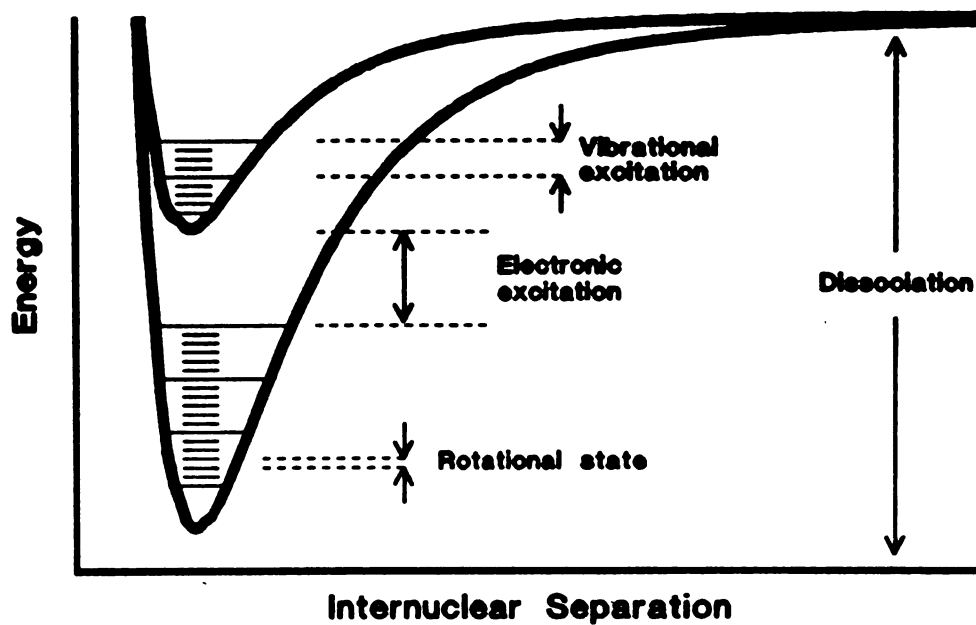


Figure 6.3 Degrees of Freedom for Diatomic Species

### 6.3 Methods of Analysis

A variety of methods exist for the spectroscopic determination of temperatures and populations within a plasma. These methods are based on kinetic theory and statistical physics using the Maxwell-Boltzmann formulas. Experimental investigations were conducted using the Single-line, Two-line ratio, and atomic Boltzmann methods to obtain electronic temperatures. These experimental temperatures were compared to those obtained from theory and used to estimate the constituent species within the plasma.

#### 6.3.1 Single Atomic Line Method

When self-absorption is negligible, that is, the reabsorption in one part of a hot gas of radiant energy emitted by another part, the integrated radiance of an atomic emission line is<sup>33</sup>

$$I_{nm} = \frac{C}{4\pi} l \rho^{(n)} A_{nm} h\nu_{nm} \quad (6.4)$$

The transition probability,  $A_{nm}$ , referred to as Einstein's coefficient, can be found in numerous references<sup>29, 35</sup>. The number density,  $\rho^{(n)}$ , is given by the Maxwell-Boltzmann relation

$$\rho^{(n)} = \rho_0 \frac{g_n}{Q} e^{-\frac{E_n}{kT}} \quad (6.5)$$

Combining Equations 6.4 - 6.5 and substituting  $\nu_{nm} = \lambda_{nm}^{-1}$ , gives the radiance of a single atomic line

$$I_{nm} = \frac{hc\rho_0 l g_n A_{nm}}{4\pi Q \lambda_{nm}} e^{-\frac{E_n}{kT}} \quad (6.6)$$

Once the line and wavelength have been identified, the values of  $g_n$ ,  $Q$ , and  $E_n$  can be found in published tables<sup>10, 29</sup>. Values of  $A_{nm}$  are known accurately for relatively few lines but the dependence of  $I_{nm}$  on  $T$  is much greater than its dependence on  $A_{nm}$ , so that only moderate accuracy in  $A_{nm}$  is needed. The empirical value  $l$  is the dimension along the optical path. This method is commonly applied by preparing a plot of  $I_{nm}$  vs.  $T$  for each line to be used. The actual temperature of a species is found by relating the measured  $I_{nm}$  value to the corresponding temperature on the plot.

The Single-line method is complicated by the number density of neutral atoms since it is a function of temperature. If a pure gas is used at relatively low pressures, the ideal gas law can be safely used to calculate  $\rho_0$  at temperatures where ionization is negligible. An iteration procedure is required where  $\rho_0$  is calculated from an assumed temperature and substituted back into Equation 6.6 to calculate the temperature. Because  $\rho_0$  varies much more slowly with  $T$  than does the exponential function in Equation 6.6 the iteration converges rather quickly.

Any non-overlapping spectral line or group of lines with relatively accurate values of  $\lambda_{nm}$ ,  $E_n$ , and  $A_{nm}$  can be used with Equation 6.6 for temperature measurement. A molecular band may be included in the group of lines so  $A_{nm}$  and  $E_n$  are band, rather than line, parameters, and perhaps even a system of many bands, all part of one electronic transition of a molecule. Due to the broadening of spectral lines caused by collisions between radiating particles, overlapping of neighboring lines is more pronounced at higher pressures. This overlap is harder to avoid for bands than for lines, because bands are spread over a broad spectral region. Therefore, a safe practice is to integrate the line radiance  $I_{nm}$  over the full width of the line to ensure Equations 6.4 and 6.6 to be valid.

The electronic partition function,  $Q$ , must be incorporated into any diagnostic used to determine particle density or temperature and is defined as<sup>18</sup>

$$Q = \sum_n g_n e^{-\frac{E_n}{kT}} \quad (6.7)$$

This function is very close to 1 for most gases, particularly those with high excitation energies, making the transition from the ground state under low to moderate temperatures<sup>10</sup>. This condition also holds rigorously for an ideal gas, but holds only at low pressures for real gases<sup>36</sup>.

### 6.3.2 Two-line Radiance Ratio Method

For a plasma in LTE, the internal degrees of freedom given by the Maxwell-Boltzmann distribution, Equation 6.3, can be used to determine the populations of different energy states. The temperature can be estimated by measuring the relative populations of two or more states, and determining the value of T for which Equation 6.3 fits the data best.

If  $\lambda_{nm}$ ,  $E_n$ ,  $g_n$ , and  $A_{nm}$  of each of two atomic lines are known, it follows from Equation 6.3 that<sup>33</sup>

$$\frac{I_1}{I_2} = \frac{g_1 A_1 \lambda_2}{g_2 A_2 \lambda_1} e^{-\frac{(E_1 - E_2)}{kT}} \quad (6.8)$$

where the subscripts 1 and 2 refer to the two spectral lines. Griem modifies Equation 6.8 by rearranging and introducing the absorption oscillator strength,  $f$ , to give<sup>37</sup>

$$kT = E_1 - E_2 \left[ \ln \frac{N_2 \lambda_2^3 g_1 f_1}{N_1 \lambda_1^3 g_2 f_2} \right]^{-1} \quad (6.9)$$

Griem also gives extensive tabulated values of the absorption oscillator strengths for various systems<sup>37</sup>.

The advantage of this method over the Single-line method is the elimination of the number density and path length. This method also allows relative, rather than absolute, transition probabilities to be used. The disadvantages of this method are the poor sensitivity for line intensities with

a small difference in upper energy states and its dependence on LTE.

When both lines are from the neutral atom, the two-line ratio method yields an atomic excitation temperature corresponding to the equilibrium population of neutral atom electronic energy levels. If both lines are from an ion, the ionic excitation temperature is obtained.

### 6.3.3 Atomic Boltzmann Plot Method

The atomic Boltzmann plot is an extension of the two-line method to many lines. Taking the natural logarithms of Equation 6.6 and making the electronic partition function,  $Q$ , equal to unity gives<sup>33</sup>

$$\ln \left[ \frac{I_{nm} \lambda_{nm}}{g_n A_{nm}} \right] = C - \frac{E_n}{kT} \quad (6.10)$$

where:

$$C = \ln \left[ \frac{l \rho_0 h c}{4 \pi} \right]$$

Equation 6.10 reveals that the intercept on the ordinate axis,  $C$ , can be used to determine the particle density  $\rho_0$  if the path  $l$  is known.

## 6.4 Species Concentrations

In LTE, the Saha-Eggert equation can be applied for the calculation of the particle distribution function for neutral particles and ions. The Saha-Eggert equation is defined as<sup>10</sup>

$$S(T) = \frac{\rho_1 \rho_e}{\rho_o} = \frac{\rho_1^2}{\rho_o} = \frac{2(2\pi m_e kT)^{\frac{3}{2}}}{h^3} \frac{Q_1}{Q_o} e^{-\frac{\Delta E}{kT}} \quad (6.11)$$

where  $Q_1$  and  $Q_o$  denote the partition functions for the ion and atom, respectively. Equation 6.11 assumes the reaction follows



where  $M$ ,  $M^+$ , and  $e^-$  represent the neutral atom, ion, and electron, respectively. Consequently, the number of ions in the plasma must be equal to the number of electrons, since each is responsible for the other. Equation 6.11 is most useful when the ionization is appreciable (> 5%) and  $\rho_o$  cannot be determined from the ideal gas law. The partition functions often deviate considerably from the statistical weight of the ground state, especially at high temperatures<sup>36</sup>.

Tabulated data is available for the "reduced" Saha-Eggert equation<sup>10</sup>

$$S(T) = \frac{2Q_1}{Q_o} S^*(T) \quad (6.13)$$

where:

$$S^*(T) = 2.4125 \times 10^{21} T^{\frac{3}{2}} e^{-\frac{AE}{kT}}, \quad m^{-3}$$

Drawin lists values for  $S^*(T)$ , as well as  $Q_1$  and  $Q_0$ , at various temperatures for different elements and ionization stages.

## 6.5 Advanced Methods of Analysis

Though much information has been gained by these investigations, many assumptions have also been made. In order to validate these assumptions, advanced experimental techniques, including LIF and actinometry, must be employed. Though current experimental equipment limitations, primarily failure to maintain low enough pressures, prevented the use of these methods, they are still introduced for the completion of this topic and for future research.

### 6.5.1 Laser-Induced Fluorescence Spectroscopy

Laser-induced fluorescence spectroscopy (LIF) can potentially provide species concentration and temperature trends and also validate the existence of the often assumed local thermal equilibrium. A recently acquired high-watt laser will enable experiments to be conducted using LIF spectroscopy.

LIF utilizes a tunable dye laser to excite a transition of a molecule of interest. The fluorescence emitted by the excited molecules can be sensitively

detected by photomultiplier tubes or optical multichannel detectors shielded with the appropriate interference filters. By observing the fluorescence from only a short length along the laser beam, good spatial resolution can be achieved. Variable fluorescence excitation scans can be recorded by tuning the monochromator to a particular emission wavelength of an atomic or molecular species of interest<sup>38</sup>.

LIF is a prime method of diagnostics because it can yield spatially resolved measurements with a high degree of sensitivity. This technique is particularly ideal for the detection of constituent light atomic species in plasmas where conventional optical detection is difficult<sup>39</sup>. Researchers at MSU will use LIF to obtain quantitative measurements of, among other things, radical and charged particle densities and velocity distributions, gas temperatures (including rotational and vibrational), and electric fields.

This versatile technique will accurately describe populations of various species, such as ions, neutrals, and free electrons, that have been previously described by methods where dubious assumptions have been made. One particular assumption that can be evaluated for its validity indirectly through LIF is that of LTE. Easily accessible models can be developed with the information obtained from LIF. There are only a handful of LIF experiments conducted with plasma mediums worldwide so the work at MSU will continue to be on the cutting edge of this technology.

### 6.5.2 Actinometry

Though LIF determinations can be obtained in most experiments, there are instances where this technique is not applicable or practical and the use of actinometry may be desirable. Inert-gas actinometry is a simpler technique than LIF and measures the concentrations of the reactive ground state atoms or molecules by comparison of their emissions with those originated by one or more inert gases added to the discharge mixture. The concentration of the inert gases or actinometers, which normally includes  $N_2$ , Ar, He, or their combinations, are held constant at 2-3% of the overall concentration. The mixtures of these reactive gases and various actinometers have been under study at MSU in order to better understand their behavioral effects in a plasma.

Since the noble gas density is known, the excitation efficiency of any of its levels is determined simply by dividing the emission intensity of that level by the noble gas density. If the excited state responsible for a noble gas emission matches closely in energy with the level responsible for an emission line from a reactive species, then the same group of electrons will be responsible for the excitation of both levels. The excitation efficiencies of these levels of the noble gas atom and the reactive particle will then have similar dependence on plasma parameters. Thus, the reactive particle density can be determined by combining its emission intensity with the excitation efficiency of the noble gas. Under certain conditions, a simple actinometric

equation of the form

$$\frac{I_X}{I_A} = \frac{[X]}{[A]} \times \text{constant} \quad (6.14)$$

where:

$I_X$  = emission intensity of molecule X  
 $I_A$  = emission intensity of actinometer  
 $[X]$  = concentration of molecule  
 $[A]$  = concentraion of actinometer  
 constant = proportionality constant

can be used to evaluate the concentration trends of [X] from the variation of  $I_X/I_A$ , since [A] is kept constant. In most cases, the constant used in the above equation will not be solved for analytically since it is independent of the discharge parameters and relative results can be easily generated.

Three conditions must be met in order to ensure that the emission intensity ratio is proportional to the concentration ratio<sup>40</sup>:

- The emission intensities,  $I_X$  and  $I_A$ , must be produced by electron impact excitation of the ground state species X and A.
- $I_X$  and  $I_A$ , must decay primarily by photon emission.
- The electron impact excitation cross sections for X and A must have a similar threshold and shape as a function of electron energy.

These criteria make the selection of the actinometer a crucial parameter. But even when the conditions are violated, in practice the emission intensity ratio may be proportional to the concentration ratio over some limited range of plasma parameters.

Actinometry experiments will provide information on the densities of ion and neutral species within the plasma. This technique could also be extended in the determination of gaseous temperatures within the plasma. Actinometry is a powerful nonintrusive diagnostic technique for understanding the role played by stable and unstable species which are produced in various discharges.

### 6.6 Electronic Temperatures

The electronic temperatures for a helium plasma were determined as a function of pressure and gas flow rate using the atomic Boltzmann, Single-line, Two-line methods. The experimental conditions are summarized in Table 6.1 below.

**Table 6.1 Spectroscopic Conditions**

Net Power Input	= 175 - 200 W
Spectrometer Scan Rate	= 0.5 Å/min
Entrance Slit Width	= 0.1 mm
Exit Slit Width	= 0.15 mm
PMT Power Supply	= 900 volts
Resonance Mode	= TM <sub>012</sub>

Helium was chosen as an experimental gas due to its simple atomic nature in which accurate atomic data are widely available and because of its chemical inertness. The Two-line method resulted in high standard deviations and

therefore was inconclusive. This was possibly due to the narrow range of wavelengths evaluated and consequently, the small energy differences between the transitions.

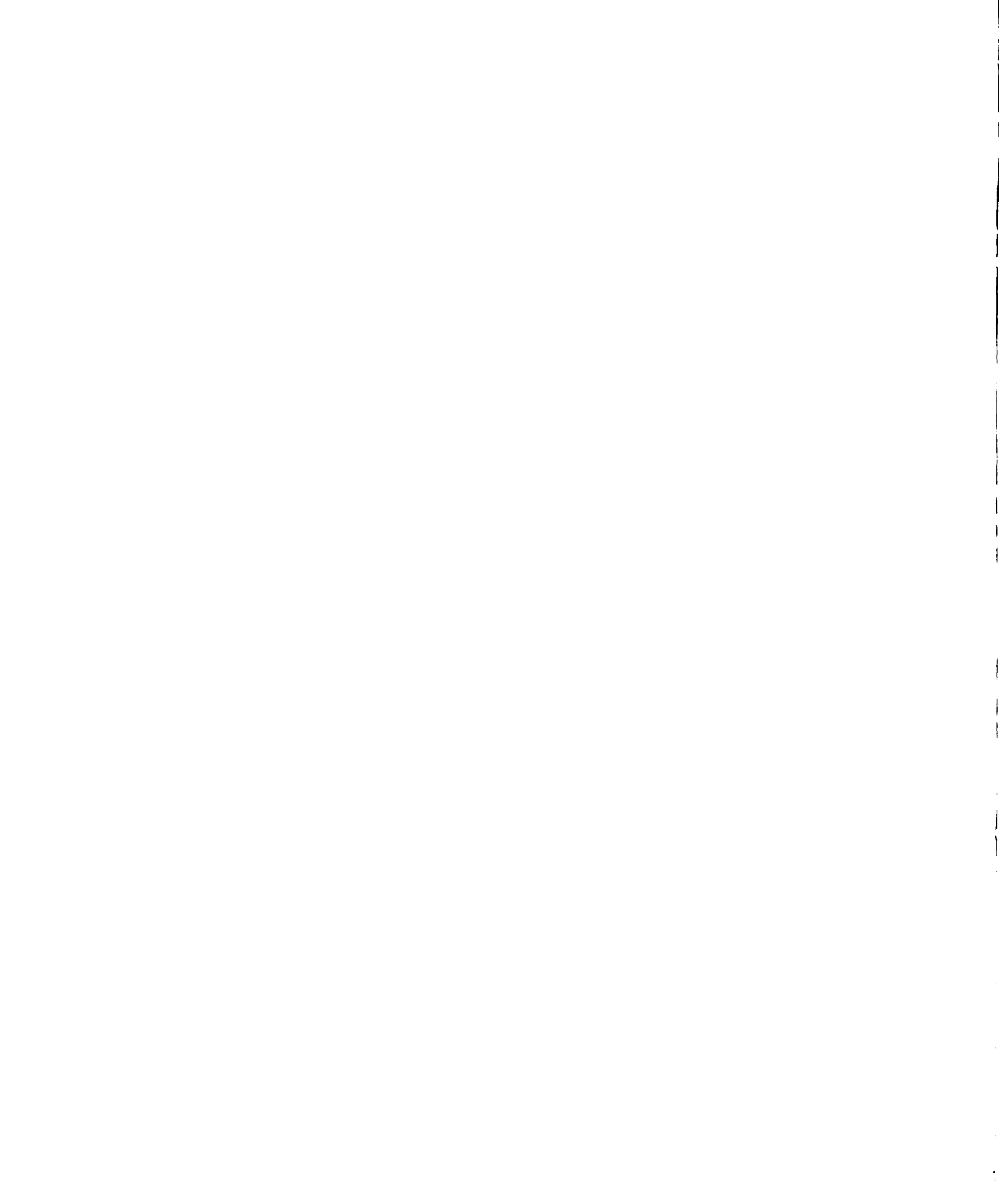
The atomic Boltzmann plot method resulted in electronic temperatures ranging from 3200 to 4600°K. A least-squares fit was used to determine the slope and intercept for each temperature. The reproducibility for these fits were all greater than 85% using 9-14 data points. Table 6.2 lists the most prevalent transitions used in these calculations and Figure 6.4 shows where these transitions appear on the helium energy diagram.

**Table 6.2 Observed Transitions**

$\lambda$ (Å)	Transition	$\lambda$ (Å)	Transition
5015.7	$2s^1S - 3p^1P^0$	4921.9	$2p^1P^0 - 4d^1D$
3964.7	$2s^1S - 4p^1P^0$	4387.9	$2p^1P^0 - 5d^1D$
3888.6	$2s^3S - 3p^3P^0$	5875.6	$2p^3P^0 - 3d^3D$
3187.7	$2s^3S - 4p^3P^0$	4471.5	$2p^3P^0 - 4d^3D$
5047.7	$2p^1P^0 - 4s^1S$	4026.2	$2p^3P^0 - 5d^3D$
4713.2	$2p^3P^0 - 4s^3S$		

The corresponding data for these lines necessary to apply the atomic Boltzmann method were taken from Striganov and the CRC Handbook<sup>29,35</sup>. A portion of these data points are summarized in Table 6.3.

These results match closely the electronic temperatures calculated by previous researchers<sup>25</sup>. A plot of  $T_e$ , calculated from the atomic Boltzmann



### Helium Energy Level Diagram

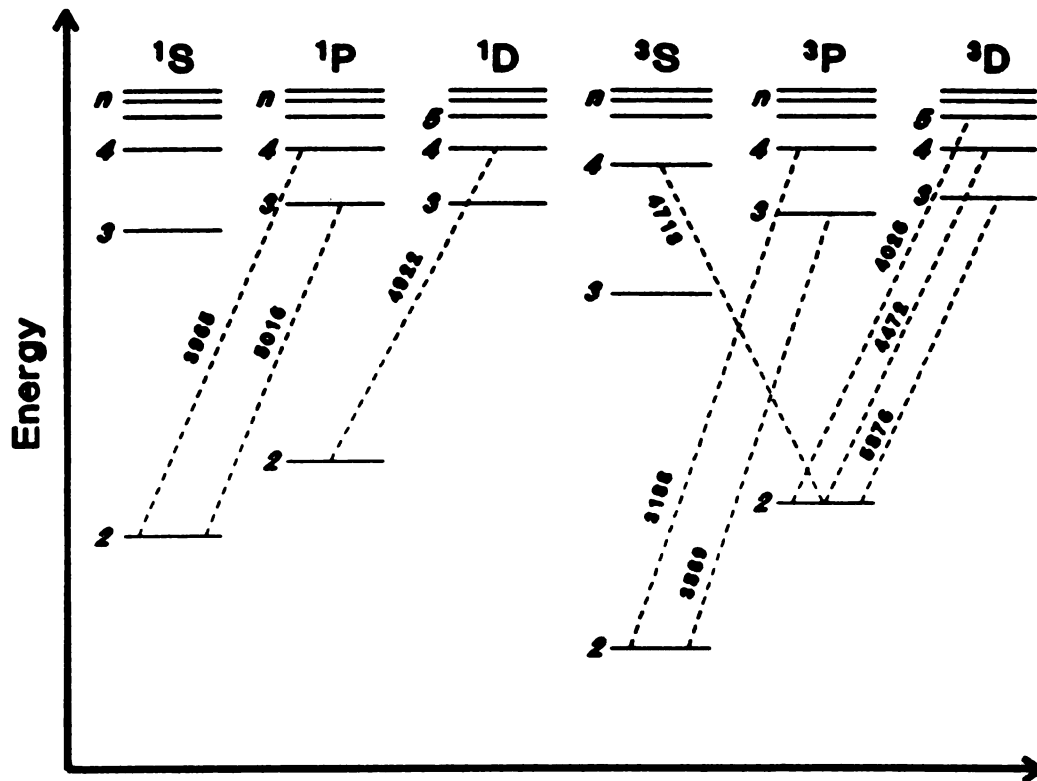
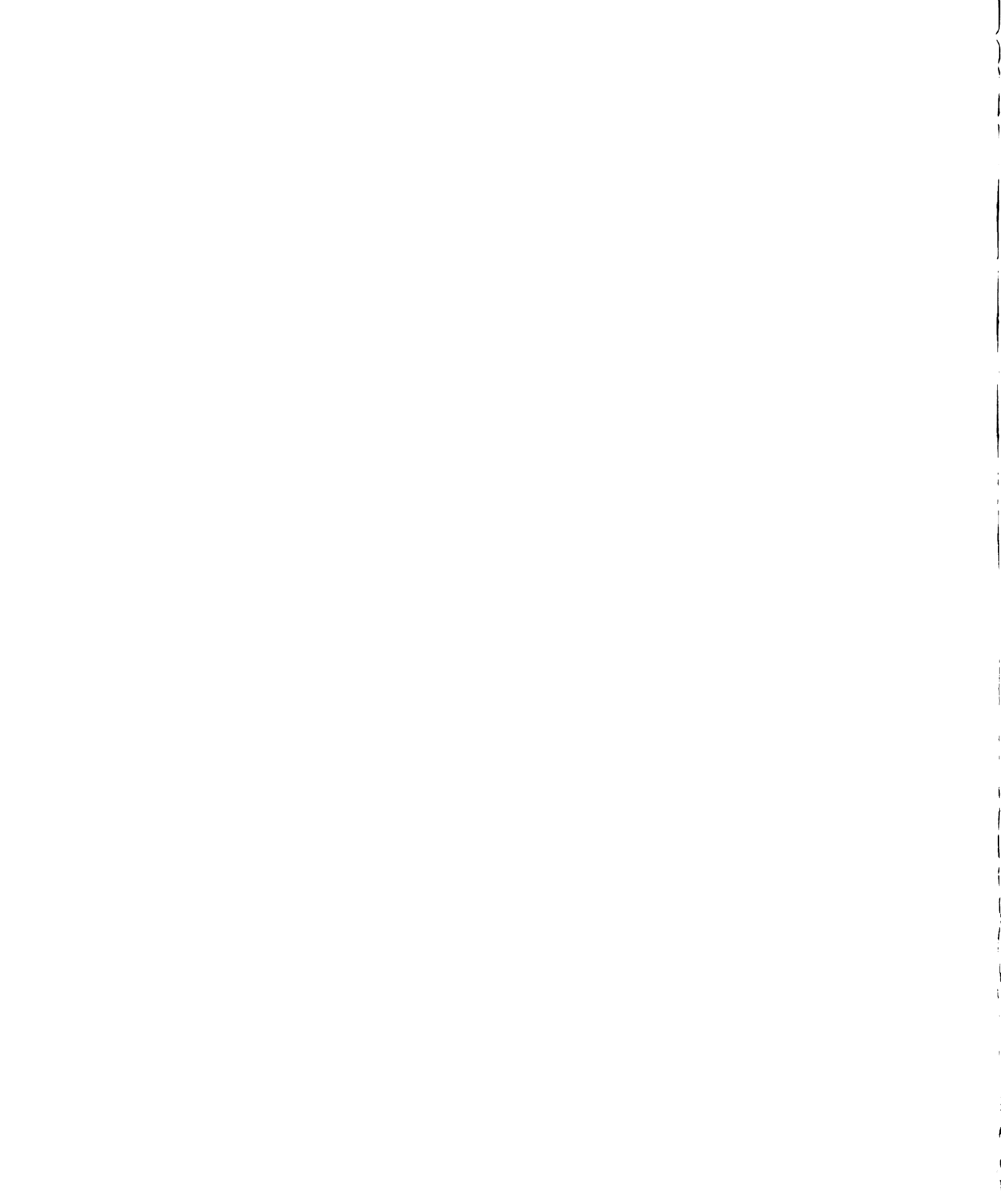


Figure 6.4 Energy Level Diagram for Helium



**Table 6.3 Spectroscopic Data for Helium**

$\lambda$	$E_n$	$g_n$	$A_{nm}$	$R_\lambda$
3187.7	191217	9	0.05639	0.2175
3354.6	196079	3	0.013	0.1843
3613.6	193943	3	0.039	0.1438
3819.6	195260	15	0.0636	0.1316
3888.7	185565	9	0.09478	0.1285
3964.7	191493	3	0.0719	0.1265
4026.2	193917	15	0.116	0.1257
4120.8	193347	3	0.0444	0.123
4387.9	193918	5	0.0894	0.1205
4471.5	191445	15	0.246	0.1239
4713.2	190298	3	0.0955	0.146
4921.9	191447	5	0.198	0.1697
5015.68	186210	3	0.1338	0.1852
5047.7	190940	1	0.0675	0.1904
5875.6	186102	15	0.7053	1.1414

where:

$$\lambda = \text{\AA}$$

$$E_n = \text{Upper energy level, cm}^{-1}$$

$$g_n = \text{Upper statistical weight}$$

$$A_{nm} = \text{Transition probability, } 10^8 \text{ s}^{-1}$$

$$R_\lambda = \text{Response Function}$$

method, as a function of pressure is given in the top of Figure 6.5. The gas flow rate was maintained at 500 sccm and the pressure was steadily increased from 5 Torr to 800 Torr.

The bottom curve of Figure 6.5 shows the electronic temperatures of the same emission line intensities used in the top, but calculated from the Single-line method. The results of these measurements produced considerably different temperatures than those obtained from the atomic Boltzmann Plots. These temperatures range from 10,000 to 14,000°K but the overall trend is maintained. Each data point represents an average of the temperatures obtained over all the measured transitions. The error in these measurements was  $\pm 500^{\circ}\text{K}$ . A sample graph used to obtain these results for the Single-line method is illustrated in Figure 6.6. Based on classical statistical mechanics, Lick and Emmons have estimated the electron temperatures for a helium plasma under these conditions to be approximately 11,000°K<sup>18</sup>.

Both plots in Figure 6.5 clearly show the temperature increases with pressure and slowly levels off at higher pressures. Experiments show that this leveling off is an attribute of microwave power limitations. The helium plasma becomes "saturated" with power and additional power input is reflected. Gases with additional degrees of freedom, such as nitrogen, are capable of absorbing greater amounts of power.

The electronic temperature calculated by the atomic Boltzmann method as a function of gas flow rate is illustrated in the top of Figure 6.7. The

## Helium Plasma Electronic Temperatures Function of Pressure

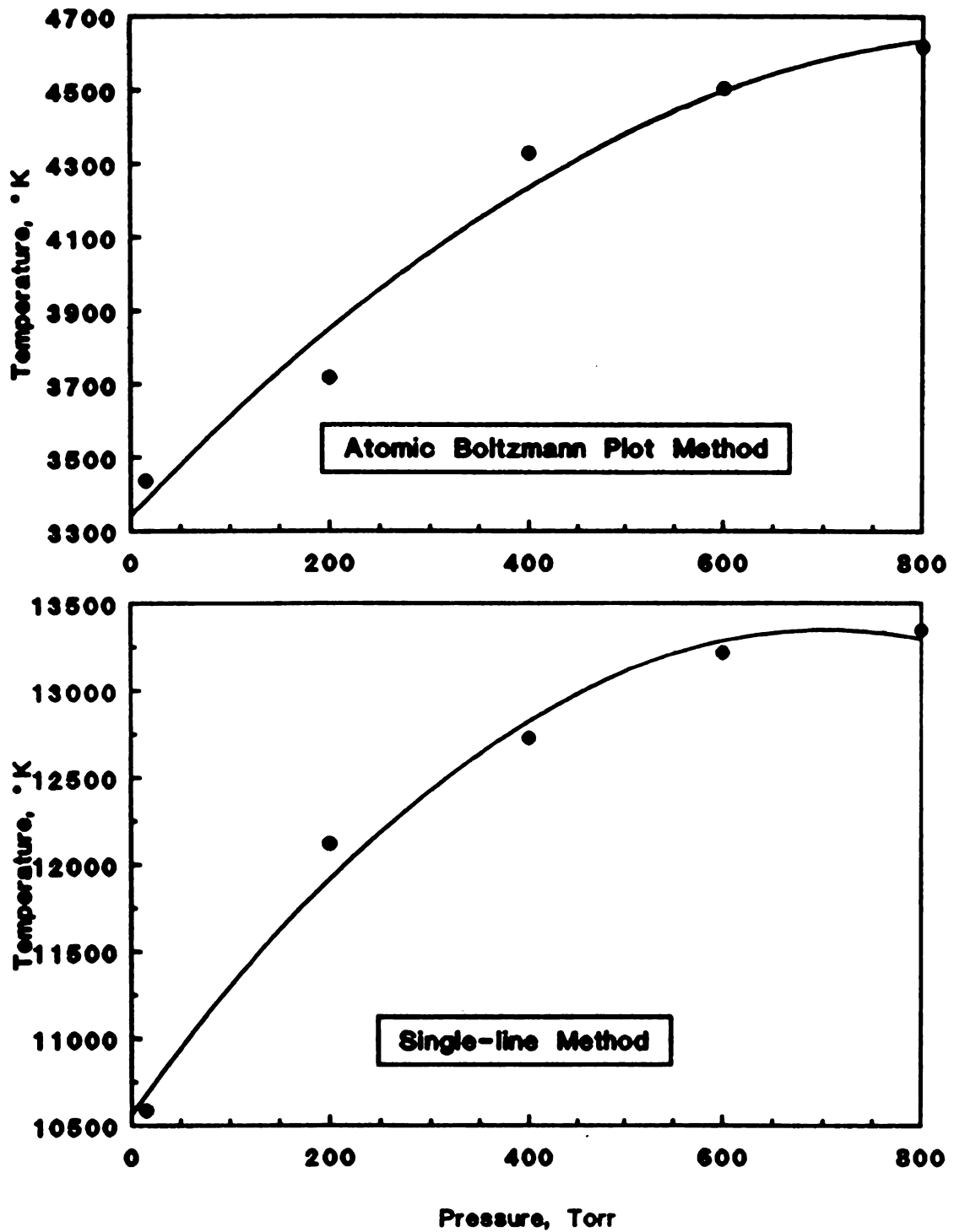


Figure 6.5 Helium Plasma  $T_e$  as a Function of Pressure

### Helium Plasma Electronic Temperatures Single-line Method

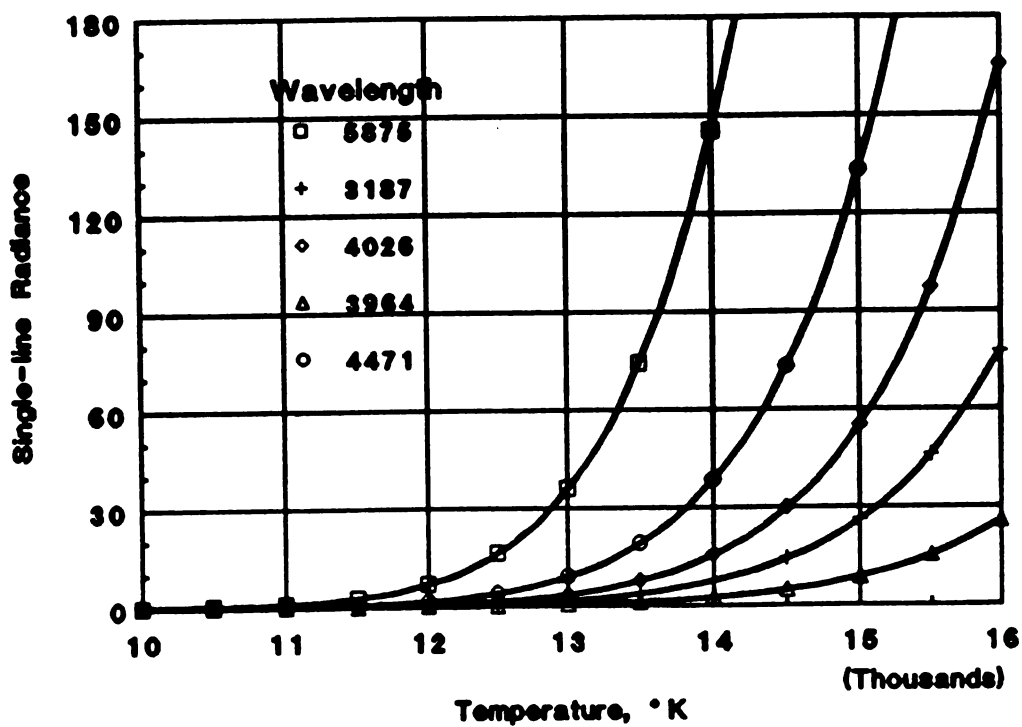


Figure 6.6 Typical Graph Generated for Single-line Method

### Helium Plasma Electronic Temperatures Function of Gas Flow Rate

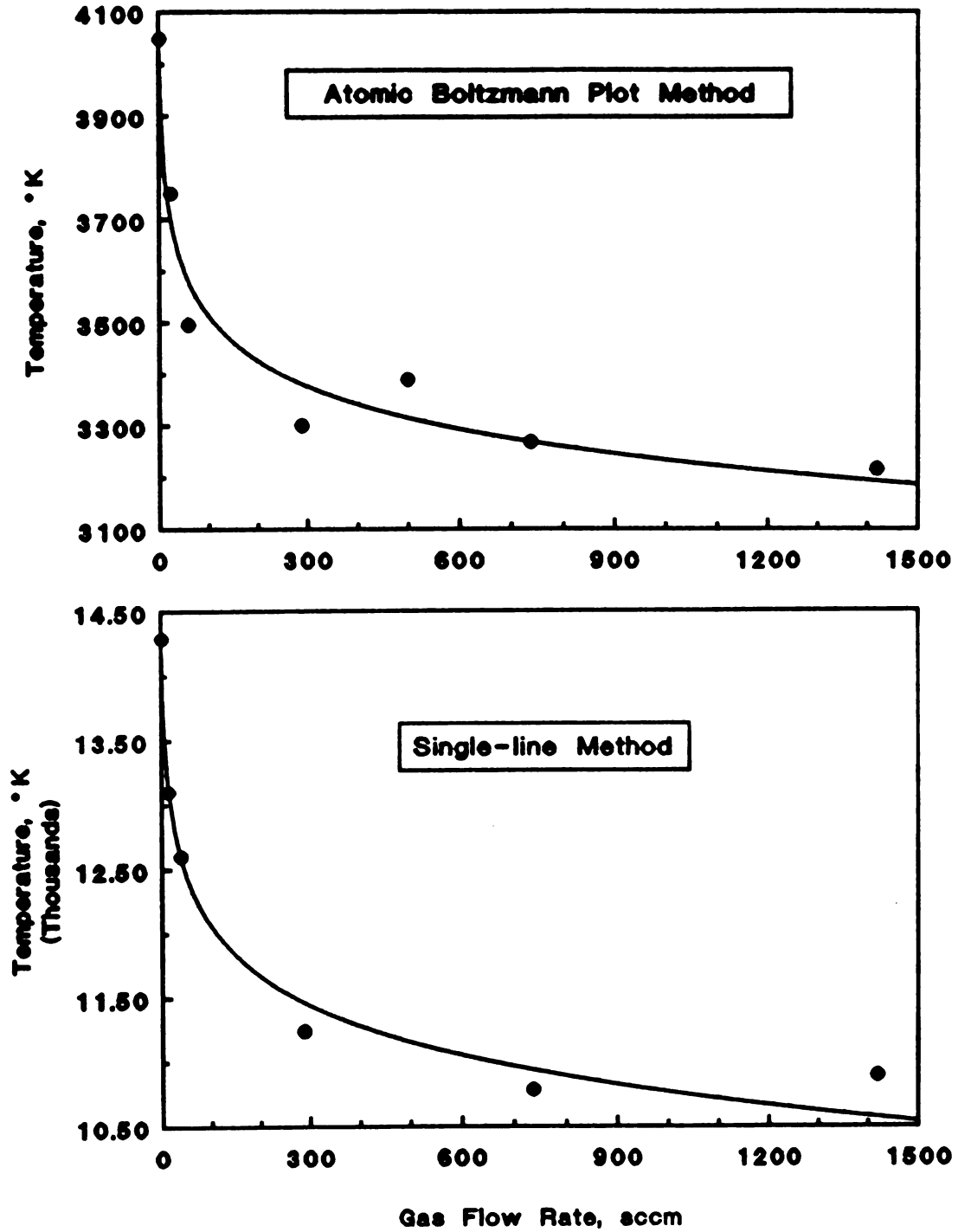


Figure 6.7 Helium Plasma  $T_e$  as a Function of Gas Flow Rate

pressure for these measurements was maintained at 20 Torr. Here the temperature suddenly drops off with an increase of gas flow and slowly levels off as the flow rate approaches 1500 sccm. This result concludes that the additional input of neutral species, at constant power, provides an obstruction for the collisional processes. The increased flow rates also allows for rapid energy transport within the plasma and the additional cold species dampen the temperature. Consequently, ionization, as well as  $T_e$ , is minimized. The corresponding electronic temperatures obtained using the Single-line method are found in the bottom curve of Figure 6.7.

The same techniques and conditions used above, with the exception of power (120 W) and pressure (0.5 Torr), were used on an argon plasma to verify the general trends. The results illustrate a consistent trend in temperature with gas flow rate. The results also confirm that the discrepancy between the two methods do exist by approximately the same order of magnitude as found for helium plasmas. The two curves in Figure 6.8 compares the atomic Boltzmann (top curve) to the Single-line method. Compared to the work of Eddy and others, the top and bottom curves seem to compare more closely to the temperatures of the gas and the electron, respectively<sup>41</sup>.

### Argon Plasma Electronic Temperatures Function of Gas Flow Rate

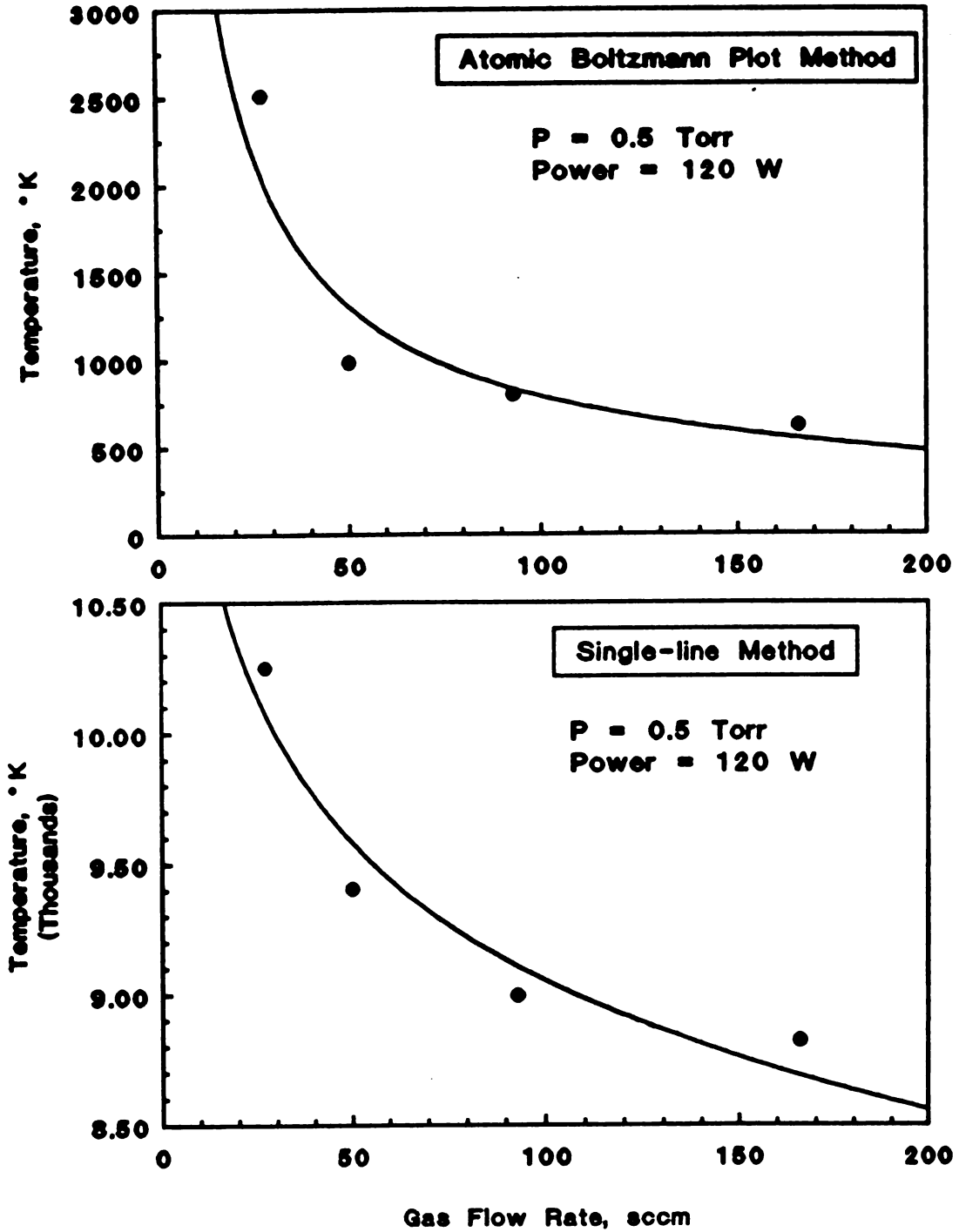


Figure 6.8 Argon Plasma  $T_e$  as a Function of Gas Flow Rate

## 6.7 Concentrations of Species

The concentrations of ions and electrons for the helium plasmas were predicted from the Saha-Eggert equations using the two different sets of temperatures obtained as a function of gas flow rate. The neutral atom densities were determined from the ideal gas law and from the atomic Boltzmann intercept. These two methods produced densities that were similar in magnitude but their corresponding trends were surprisingly different. The intercept method resulted in an initially rapid decay in neutral atom density with increasing gas flow rate but it leveled off at 300 sccm. Conversely, the ideal gas case steadily increased with increasing gas flow. These observations are illustrated in Figure 6.9.

This trend observed with the ideal gas case is easily understood since the electronic temperatures, which were assumed to be equal to the temperature of the gas, decrease with gas flow and the neutral atom density is inversely proportional to the gas temperature. A plausible explanation for this discrepancy lies in the question of whether the electronic temperatures actually do equal the temperatures of the gas, which would occur if the plasma was in local thermal equilibrium. Since the electrons are the driving force of the plasma, it is reasonable to expect their temperatures to be higher than the rest of the species in the plasma.

The degree of ionization was determined using a combination of the

### Helium Plasma Neutral Atom Density Function of Gas Flow Rate

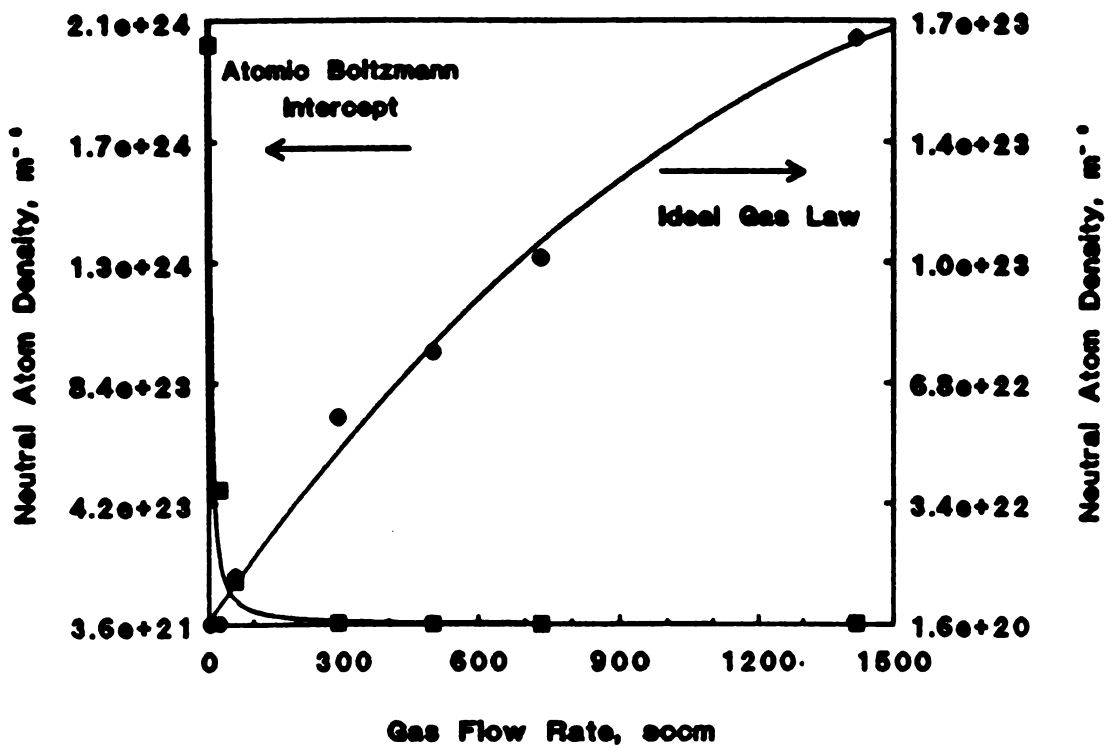


Figure 6.9 Helium Plasma Neutral Atom Density as a Function of Gas Flow Rate

Saha-Eggert equations and tabulated data of the "reduced" Saha-Eggert equations<sup>10</sup>. The tabulated data was fit to a power-law equation maintaining a 99.99% reproducibility value. As the degree of ionization approaches unity (100%), these two methods produce equal results as illustrated in Figure 6.10.

The temperatures used in Figure 6.10 were those obtained from the Single-line method, ranging from 10,000 to 14,000°K. The resulting degree of ionization rapidly drops from 46% to 0.1% with increasing gas flow.

When the ideal gas law, used to determine the neutral atom density, combined with temperatures obtained from the atomic Boltzmann plot are applied to the Saha-Eggert equations, the plot found in Figure 6.11 is produced. The overall trend remains the same as that found in Figure 6.10, but the degree of ionization falls to  $1.2 \times 10^{-4}\%$ . Since no consistently detectable  $\text{He}^+$  lines were observed in the spectrum under these conditions, this result seems perfectly plausible. Furthermore, alternative methods used by previous researchers and the data provided by Lick and Emmons suggests the degree of ionization under these conditions to be of the same order of magnitude as those in Figure 6.11<sup>18, 22</sup>.

## 6.8 Conclusions

The emission spectra of plasmas typically exhibit strong lines of gas atoms and ions, therefore, spectroscopic methods are a potentially invaluable

## Helium Plasma Degree of Ionization Function of Gas Flow Rate

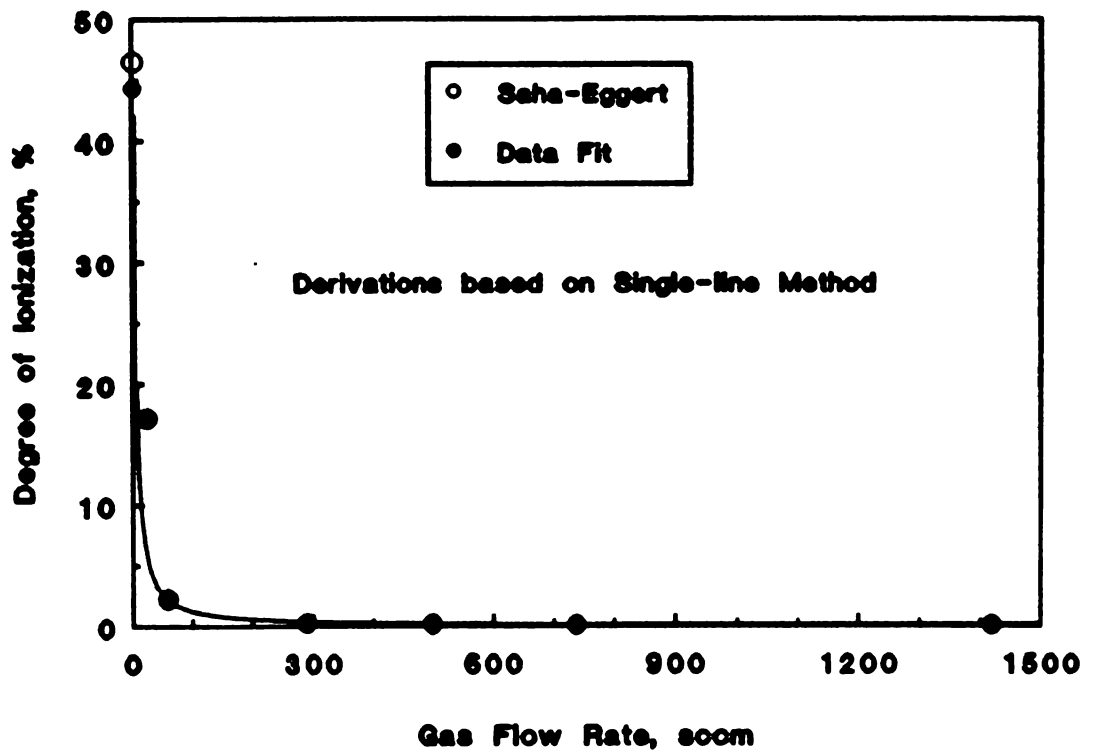


Figure 6.10 Helium Plasma Degree of Ionization as a Function of Gas Flow Rate - number 1

## Helium Plasma Degree of Ionization Function of Gas Flow Rate

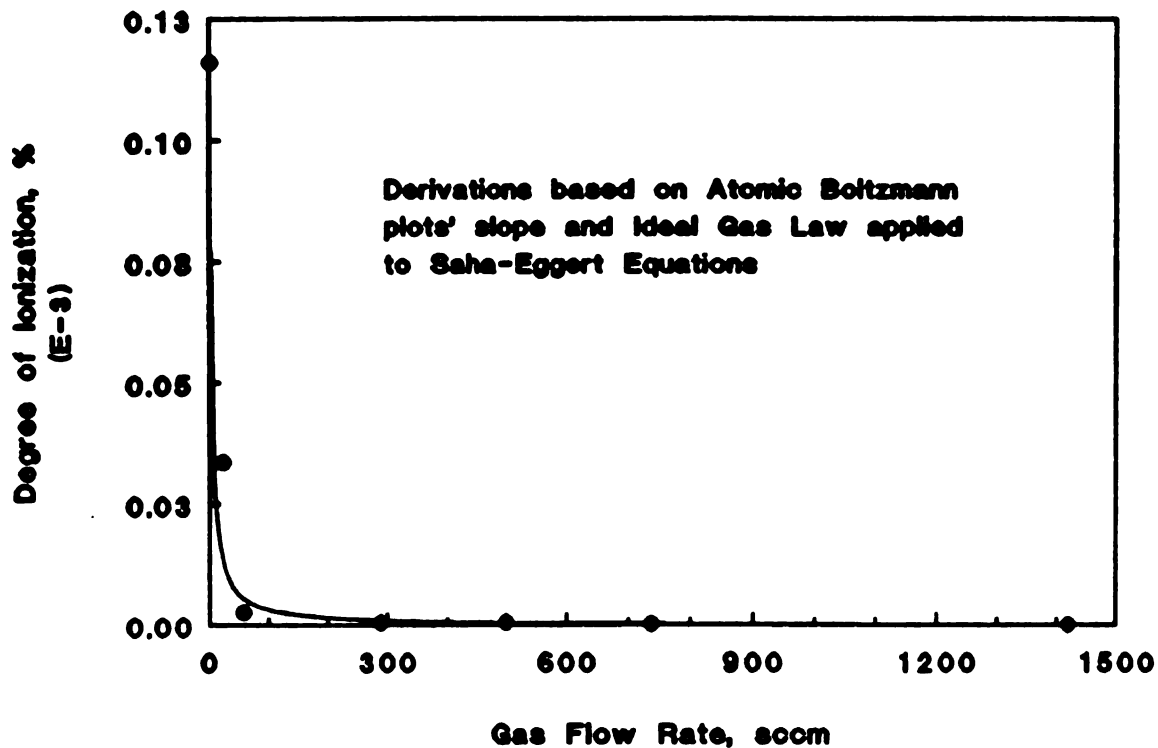


Figure 6.11 Helium Plasma Degree of Ionization as a Function of Gas Flow Rate - number 2

tool for the diagnostics of a plasma medium. The abundance of accurate supplementary data is readily available once the particular transitions have been identified. Though the methods are conceptually simple to apply, the reliability in experimental technique and instrumentation must be without question for these methods to be accurately used. It is also imperative that major assumptions, such as the existence of LTE, be understood and experimentally valid. An invalid assumption of LTE in these experiments provided the only plausible explanation for the anomalies that arose, primarily the difference in temperatures calculated from the atomic Boltzmann and Single-line methods.

The absence of LTE also explains the failure of the Two-line method, which requires the system to be in LTE. It is possible that the narrow range of threshold energies evaluated could have explained this failure, but previous work has concluded that the plasma particle velocities are not Maxwellian under these experimental conditions and that the electron densities range between  $10^{11}$  to  $10^{13}$   $\text{cm}^{-3}$  <sup>13, 22, 42</sup>. Eddy determined the electron (or ion) densities required for LTE to be about  $2 \times 10^{17}$   $\text{cm}^{-3}$ , far above those obtained in this investigation<sup>41</sup>. Pressures greater than 5 bar must be reached for these densities to be acquired. Another explanation for the non-LTE existence could lie in the particle relaxation times exceeding the particle residence times or the lack of a microreversibility between the collisional processes.

The discrepancy between the results obtained with the atomic Boltzmann plots and those obtained directly from the Single-line method proved to be

perplexing since each method has its valid points. Both methods are theoretically applicable for the determination of electron, not electronic, temperatures. However, the degree of ionizations obtained from the atomic Boltzmann plots, combined with the lack of observable ionized atom lines concludes that the atomic Boltzmann method produced the more reliable results for the electronic temperature. Since the electronic temperature includes the energy of the excited "bound" electrons, it is reasonable to assume this temperature to be equal to the temperature of the gas. Lick and Emmons have concluded that helium is composed primarily of neutral species at temperatures below 8000°K, even at pressures of  $10^{-4}$  atm<sup>18</sup>.

The results obtained from the Single-line method accurately reflect the electron temperatures of the plasma. Since the electrons are the driving force of the plasma, it is reasonable to expect their temperatures to be higher than the other species. These temperatures measured for the helium and argon plasmas correspond well to the theoretical and experimental electron temperatures obtained by others<sup>18, 25, 33, 41</sup>. Since the electronic (or gas) temperatures are considerably lower than the electron temperatures, it confirms that the plasmas in these investigations are not in LTE.

# CHAPTER 7

---

## *Model Formulation*

### 7.1 Introduction

The most concise method of consolidating the information acquired through this research effort was found to be through the modeling of various macroscopic quantities, namely the velocity and temperature distributions around the plasma region. These models could provide additional insight on the effects of convective and conductive energy losses from the plasma to the surrounding gas. This information could then be used to better postulate the diffusional processes and reactions that dominate the plasma, which has been the basis of previous models. The advantages of modeling macroscopic properties over microscopic phenomena is that the former can be experimentally confirmed.

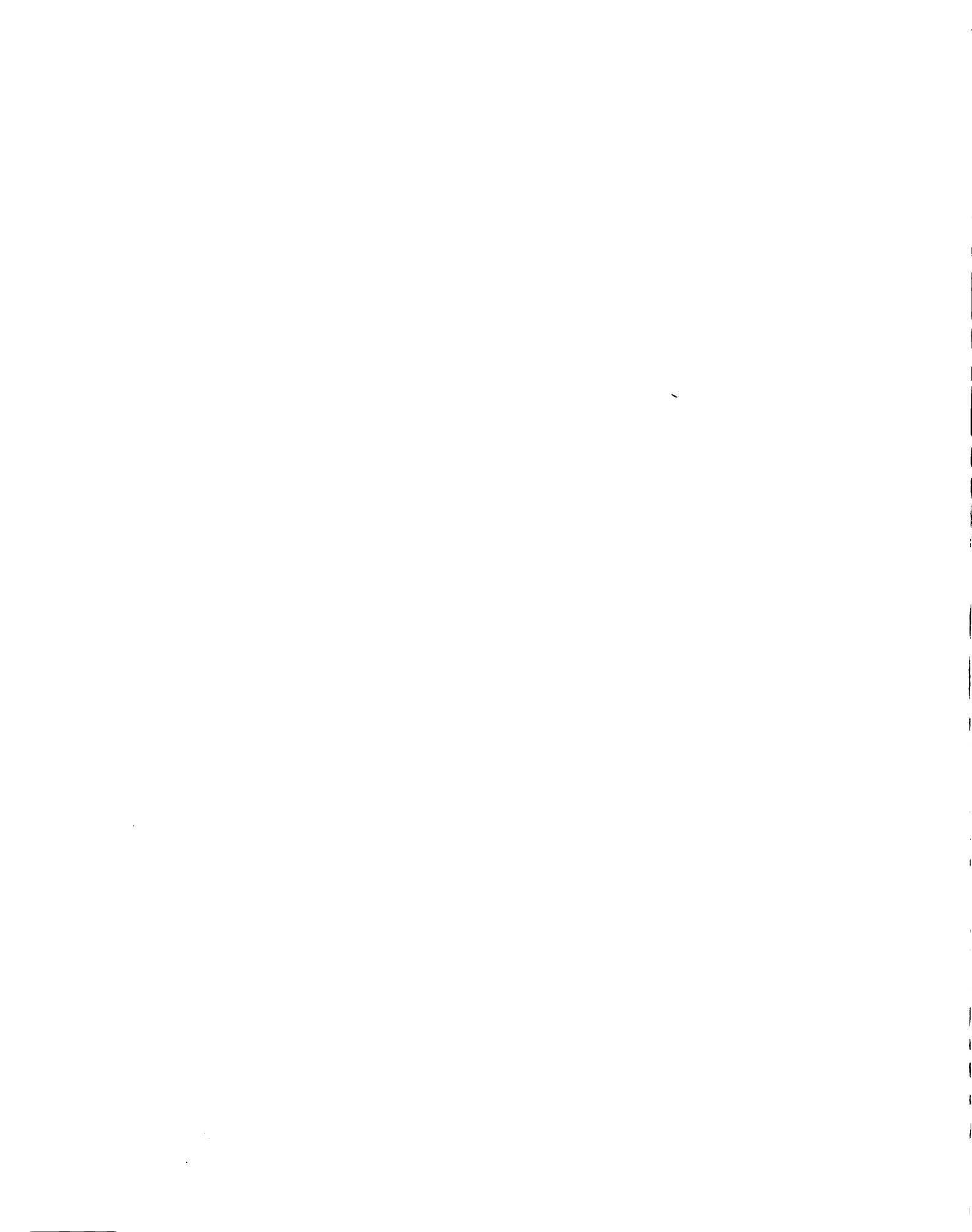
As described in Chapter 4, the influences of pressure on plasma dimension is significant. The effects of pressure on energy absorption and plasma temperatures was described in Chapters 5 and 6. Consequently, the

plasma size can be used to indirectly describe the energy absorption or efficiency of operation and the temperatures within the plasma. It is therefore critical that the proposed model be described as a strong function of plasma dimension. These parameters, primarily plasma width and length are summarized in Table 7.1. Since the helium plasma is complicated by a dumbbell shape, the width was obtained by taking the average over the two spheres and the connecting cylinder. This data is incorporated into the models as  $W_{avg} = 2R_i$  and  $L = \Delta z$ .

**Table 7.1 Helium Plasma Dimensions with Pressure**

P(Torr)	$W_{avg}$ (cm)	L(cm)	P(Torr)	$W_{avg}$ (cm)	L(cm)
0.5	2.97	5.19	400	2.47	3.67
1.0	2.91	4.74	500	2.43	3.52
10	2.69	4.29	600	2.40	3.41
50	2.63	4.04	700	2.38	3.27
100	2.61	3.97	800	2.36	3.18
200	2.57	3.81	900	2.36	3.09
300	2.52	3.77	1000	2.34	3.02

The goal of this summary is to formulate a realistic model using experimental observations that will describe the macroscopic properties of the flowing gas around the plasma. Solutions of these models, which will be sought by aid of a FORTRAN code at a later date, can then be coupled with previously acquired information on the dynamic processes within the plasma<sup>12</sup>.



**19. Portions of the models can also be used to estimate, a priori, critical properties of the plasma region. One significant contribution lies in the development of the theoretical pressure drop across the plasma. Since the assumptions made in finding  $\Delta P$  include that of an impenetrable plasma, the experimental  $\Delta P$  could be used to confirm or negate this assumption. It would even be possible to determine the degree of neutral particle flow into the plasma, which has been a widely debated topic. As described in Chapter 3, the current experimental apparatus can also measure the axial and radial temperature profiles downstream of the plasma. This data can be compared to the theoretical profiles to further evaluate the modeling assumptions. The various steps used to develop an accurate numerical representation for the velocity and temperature distributions are outlined below.**

## **7.2 Assumptions**

**Four models were considered to describe the velocity and temperature distributions around a helium plasma and immediately downstream of the discharge. The assumptions were initially oversimplified in order to grasp the physics of the problem. These assumptions were progressively enhanced until a final model, or combination of models, was developed that would accurately describe the gas flow over the plasma.**

**All of the models assume cylindrical geometries for the containment and**



the plasma region. Since the fluid is not highly viscous and the velocities are much less than sonic, the viscous dissipation term,  $\Phi$ , is neglected from the overall energy balance<sup>43</sup>. The models have also taken the thermal diffusivity,  $\alpha$ , and the gas viscosity,  $\mu$ , to be constant. A more realistic solution would have taken  $\alpha$  as a temperature-dependent variable since it is composed of  $k$  and  $\rho$ , which are strong functions of  $T$ . However, the Prandtl number, which compares the thermal diffusivity and the kinematic viscosity, appears to be constant over the conditions of this analysis as illustrated in Figure 7.1<sup>18</sup>.

The assumption that the specific heat,  $C_p$ , is constant and equal to  $2.5R$  at constant pressure is justifiable on the basis of the high excitation energies of helium and the negligible existence of excited populations. Under conditions where the degree of ionization was appreciably higher, the specific heat would vary considerably due to the formation of a mixture and the energy needed to ionize the neutral and singly-ionized species<sup>18</sup>. Uniform containment wall and plasma temperatures were assumed and wall recombination and subsequent reaction effects were ignored.

Model A begins the analysis with the assumption that the gas completely penetrates the plasma with a flat velocity profile or plugflow. Model B also assumes the complete penetration of the gas into the plasma but incorporates a parabolic velocity profile. Model C assumes an impenetratable plasma whereby the gas flows around the plasma with a parabolic velocity profile due to no slip conditions along the plasma and the containment wall. Model D also



## Prandtl Number of Modeling Fluid

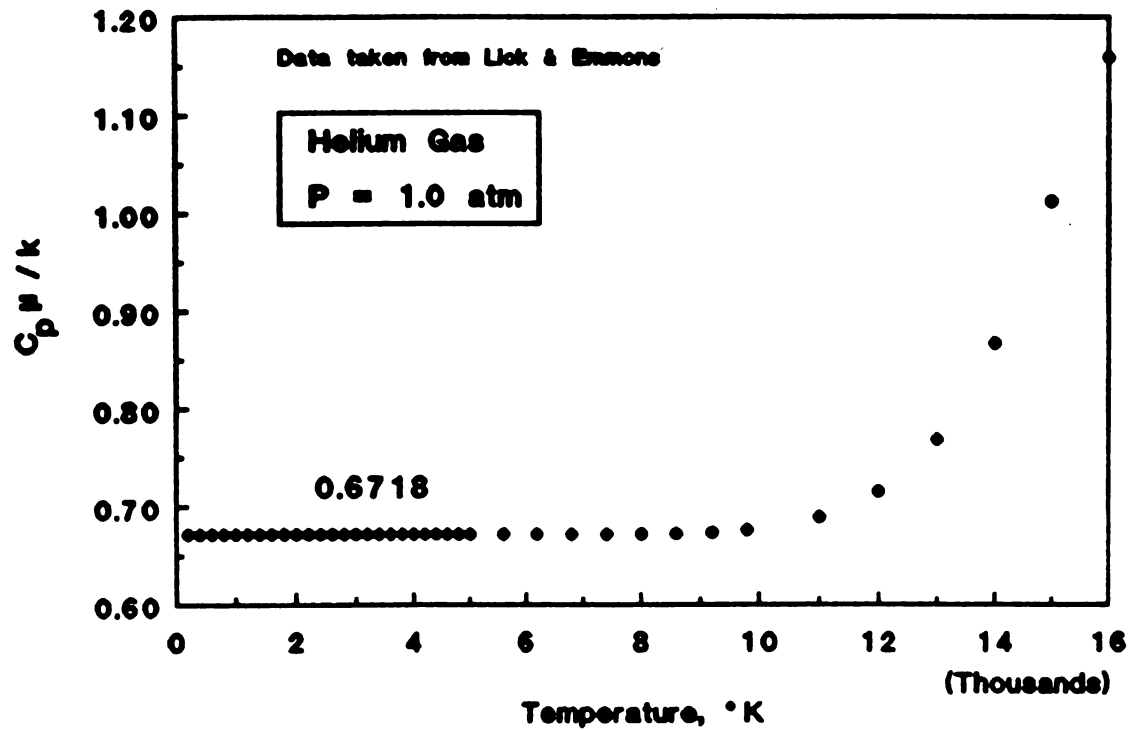


Figure 7.1 Prandtl Number of Helium with Temperature



assumes an impenetrable plasma but assumes the existence of molecular slip along the plasma boundary. Models C and D describe the effects of the plasma on the flowing gas. Using the solutions of these models for the boundary conditions of Models A or B would provide a suitable model for the distributions immediately downstream of the plasma.

### 7.3 Characterizing Dominant Forces

To begin the analysis, the Reynolds number was computed to determine the effects of inertial and viscous forces within the containment. Several extremes of the temperature and pressure were considered to obtain maximum and minimum limits.

$$Re = \frac{d_c \rho(T) V_b}{\mu(T)} = \frac{\text{Inertial terms}}{\text{Viscous terms}} \quad (7.1)$$

where:

$$d_c = 3.1 \text{ cm}$$

$$\rho_0 = 1.7859 \times 10^{-4} \text{ g/cm}^3$$

$$\rho = \frac{\rho_0 P T_0}{T P_0}$$

$$\mu_0 = 1.915 \times 10^{-4} \text{ g/cm s}$$

$$V_b = \left[ \frac{4(500 \text{ cm}^3/\text{min})}{\pi(3.1 \text{ cm})^2} \right] \frac{1 \text{ min}}{60 \text{ s}} = 1.104 \text{ cm/s}$$

The Reynolds number for the various cases considered are summarized in Table

7.2.



**Table 7.2 Reynolds Number at Varying Conditions**

CASE	P, Torr	T, K	$\mu(T), 10^{-4}$ g/cm s	$\rho(T), 10^{-8}$ g/cm <sup>3</sup>	Re
1	0.76	300	1.915	17.9	0.0032
2	0.76	10,000	26.34	.536	.000007
3	760	300	1.915	17.859	3.19
4	760	10,000	27.05	535.8	.0068

In all but the most extreme case (3), the Reynolds number is much less than one. This indicates that the viscous forces dominate and the inertial terms can be neglected. It is important to note that the apparent laminar nature of the flow may still exhibit turbulent characteristics due to mixing attributed to thermal mixing and density variation. In fact, this mixing may be desirable from the viewpoint that it generates a homogenous process that can be analyzed as a well-mixed or CSTR reactor<sup>28, 44, 45</sup>.

The derivations of each model are based on the combined influences of the differential momentum and energy balances. The general form of the equation of motion in cylindrical coordinates along the direction of flow (z) is

$$\frac{\partial v_z}{\partial t} + v_r \frac{\partial v_z}{\partial r} + \frac{v_\theta}{r} \frac{\partial v_z}{\partial \theta} + v_z \frac{\partial v_z}{\partial z} = g_c X_z - \frac{g_c}{\rho} \frac{\partial P}{\partial z} \quad (7.2)$$

$$+ v \left[ \frac{1}{r} \frac{\partial}{\partial r} \left( r \frac{\partial v_z}{\partial r} \right) + \frac{1}{r^2} \frac{\partial^2 v_z}{\partial \theta^2} + \frac{\partial^2 v_z}{\partial z^2} \right]$$

and the energy balance is

$$\begin{aligned} \frac{\partial T}{\partial t} + v_r \frac{\partial T}{\partial r} + \frac{v_\theta}{r} \frac{\partial T}{\partial \theta} + v_z \frac{\partial T}{\partial z} \\ = \alpha \left[ \frac{1}{r} \frac{\partial}{\partial r} \left( r \frac{\partial T}{\partial r} \right) + \frac{1}{r^2} \frac{\partial^2 T}{\partial \theta^2} + \frac{\partial^2 T}{\partial z^2} \right] \end{aligned} \quad (7.3)$$

where the thermal diffusivity is defined as

$$\alpha = \frac{k}{\rho C_p}$$

The equation of motion is solved for each model and incorporated into the corresponding reduced energy balance. Analytical solutions are obtainable for most of the models but complications resulting from Bessel functions would force these solutions to be further evaluated numerically.

#### 7.4 Model A - Penetratable Plasma with Plugflow

This model, whose boundary conditions are illustrated in Figure 7.2, assumes a penetratable plasma region and a flat velocity profile.

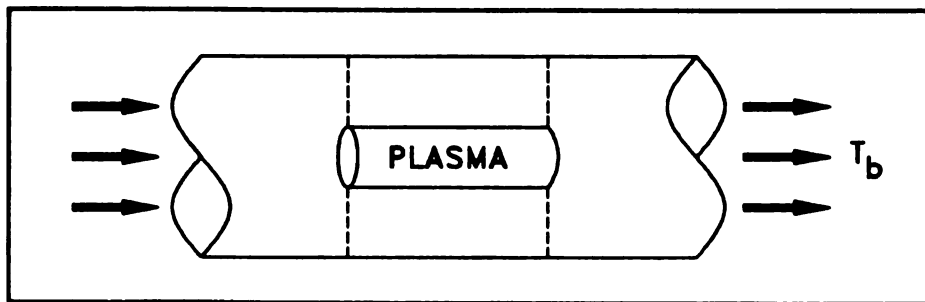


Figure 7.2 Plugflow through Plasma

The following assumptions, discussed in section 7.2, were made in the

analysis:

1. steady-state
2. laminar flow
3. fully developed flow
4. axisymmetric
5. negligible pressure drop across small reactor length ( $dP/dz = \text{constant}$ ) and negligible compression effects
6. negligible entrance effects
7.  $k$ ,  $C_p$ ,  $\rho$ , and  $\mu$  are individually constant
8. uniform wall temperature, inlet temperature
9. negligible body forces
10. Rodlike or plugflow,  $V_z = V_b$

The simplified form of the equation of motion becomes

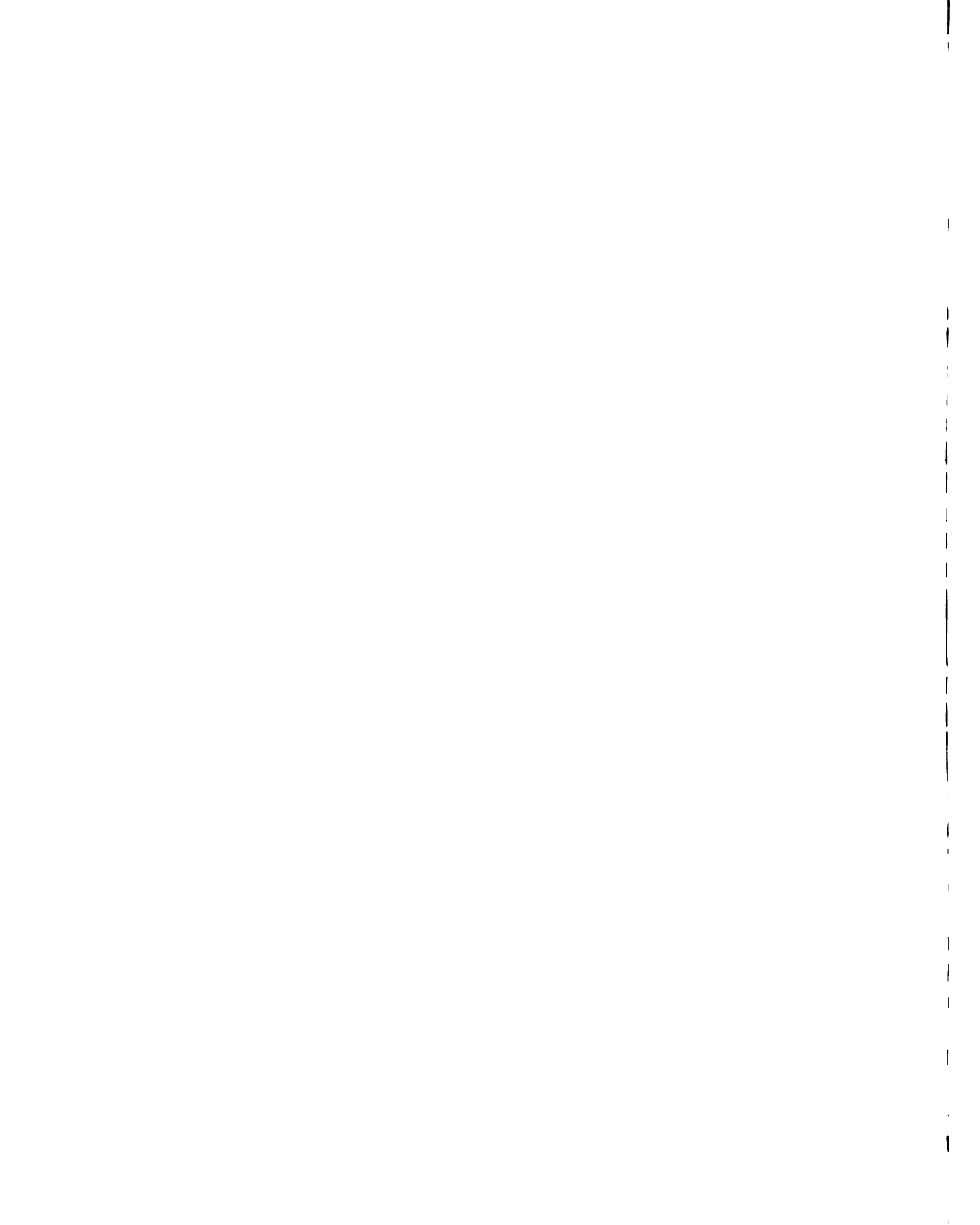
$$\frac{1}{r} \frac{\partial}{\partial r} \left( r \frac{\partial V_z}{\partial r} \right) = \frac{g_c}{\mu} \frac{\partial P}{\partial z} = \text{constant} \quad (7.4)$$

or

$$\frac{\partial^2 V_z}{\partial r^2} + \frac{1}{r} \frac{\partial V_z}{\partial r} = \frac{g_c}{\mu} \frac{\partial P}{\partial z} = \text{constant} \quad (7.5)$$

which is subject to the following boundary conditions:

$$\begin{aligned} \frac{dV_z}{dr} &= 0 & \text{at } r &= 0 \\ V_z &= 0 & \text{at } r &= R_0 \text{ (no slip on wall)} \end{aligned}$$



Integrating twice and applying the boundary conditions gives

$$V_z = -\frac{g_c}{4\mu} \frac{dP}{dz} (R_0^2 - r^2) \quad (7.6)$$

The maximum velocity,  $V_{\max}$ , occurs at  $r = 0$ , thus

$$V_{\max} = -\frac{g_c}{4\mu} \frac{dP}{dz} R_0^2 \quad (7.7)$$

and the velocity becomes

$$V_z = V_{\max} \left[ 1 - \left( \frac{r}{R_0} \right)^2 \right] \quad (7.8)$$

This model assumes a flat velocity profile so  $V_z = V_{\max} = V_b$ .

Since the temperature distribution in the axial direction will be much less curved than in the radial direction, the assumption can be made that

$$\frac{\partial^2 T}{\partial z^2} = 0$$

The simplified energy balance becomes

$$\frac{1}{r} \frac{\partial}{\partial r} \left( r \frac{\partial T}{\partial r} \right) = \frac{V_z}{\alpha} \frac{\partial T}{\partial z} = \frac{V_b}{\alpha} \frac{\partial T}{\partial z} \quad (7.9)$$

or

$$\frac{\partial^2 T}{\partial r^2} + \frac{1}{r} \frac{\partial T}{\partial r} = \frac{V_z}{\alpha} \frac{\partial T}{\partial z} = \frac{V_b}{\alpha} \frac{\partial T}{\partial z} \quad (7.10)$$

Upon separating variables, which is discussed below, this partial differential equation gives two ordinary differential equations which can be solved by

conventional methods. One solution involves a simple exponential equation while the other uses a Bessel function. The solution to this equation was first obtained by Graetz<sup>46</sup> and has since been verified by numerous other researchers<sup>47</sup>. The final solution to Equation 7.10, with the boundary conditions of uniform wall and inlet temperatures, is

$$\frac{T_s - T}{T_s - T_0} = \sum_{n=1}^{n=\infty} \frac{2}{a_n J_1(a_n)} J_0\left(\frac{a_n r}{R_0}\right) e^{-\frac{2a_n^2(z/R_0)}{Re Pr}} \quad (7.11)$$

where:

$T_s$  = temperature at surface of containment

$T_0$  = temperature at time=0

$T$  = temperature along tube

$J_0$  = Bessel function of zero order

$J_1$  = Bessel function of first order

$\lambda_n$  =  $n^{\text{th}}$  root of  $J_0(\lambda_n) = 0$

$R_0$  = tube radius

$z$  = distance along tube

$Re$  = Reynolds number =  $\frac{\rho d_T V_b}{\mu}$

$Pr$  = Prandtl number =  $\frac{\mu C_p}{k}$

The bulk temperature, which defines the temperature of the fluid at any axial position, can be obtained by combining the velocity and the temperature distributions to give

$$T_b = \frac{2}{R_0^2} \int_{r=0}^{r=R_0} T r dr \quad (7.12)$$

Since the temperature profile relies heavily on the temperature of the containment and not on the internal heat source (plasma), this model would be

more suited when combined with another model. In fact, this model would be ideal for the temperature distribution at any axial position downstream of the plasma, assuming a negligible radial profile. It is unlikely that the distribution is completely independent of the radial distance, therefore, an improvement over this model is described in Model B.

### 7.5 Model B - Penetratable Plasma with Parabolic Velocity Profile

This model goes one step further than Model A since it considers the contributions of varying velocity in the radial direction. Figure 7.3 depicts the modeled region.

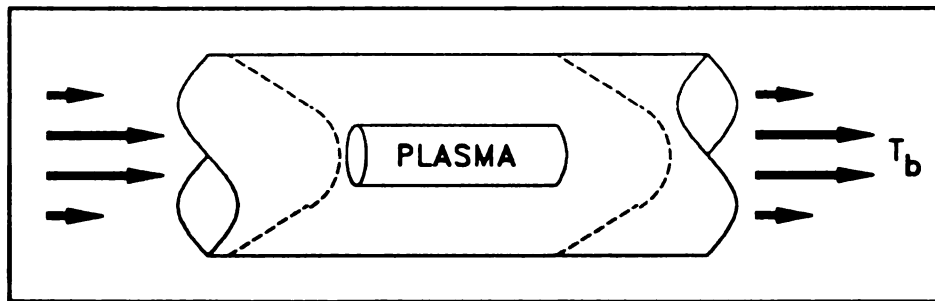


**Figure 7.3 Parabolic Velocity Distribution through Plasma**

Using the assumptions of Model A, but with a parabolic velocity profile gives

$$V_z = 2V_b \left[ 1 - \left( \frac{r}{R_0} \right)^2 \right] \quad (7.13)$$

Incorporating Equation 7.13 into the simplified energy balance, Equation 7.10,



becomes

$$\frac{\partial^2 T}{\partial r^2} + \frac{1}{r} \frac{\partial T}{\partial r} = \frac{2V_b}{\alpha} \left[ 1 - \left( \frac{r}{R_0} \right)^2 \right] \frac{\partial T}{\partial z} \quad (7.14)$$

Solving this equation requires the technique of separation of variables letting

$$T = \theta(r) \Theta(z) \quad (7.15)$$

that is,  $\theta$ , is a function of  $r$  and  $\Theta$  a function of  $z$ . Substituting these variables into Equation 7.14 and rearranging gives

$$\frac{2V_b}{\alpha \Theta} \cdot \frac{d\Theta}{dz} = \frac{\frac{d^2\theta}{dr^2} + \frac{1}{r} \frac{d\theta}{dr}}{\left[ 1 - \left( \frac{r}{R_0} \right)^2 \right] \theta} \quad (7.16)$$

Since Equation 7.15 must hold true for all values of  $r$  and  $z$ , each side can be taken equal to an arbitrary figure. Jakob suggests using  $-1/b^2$  as this figure transforming Equation 7.16 into the following<sup>48</sup>

$$\frac{d\Theta}{dz} = -\frac{\alpha \Theta}{2b^2 V_b} \quad (7.17)$$

and

$$\frac{d^2\theta}{dr^2} + \frac{1}{r} \frac{d\theta}{dr} + \frac{1}{b^2} \left[ 1 - \left( \frac{r}{R_0} \right)^2 \right] \theta = 0 \quad (7.18)$$

Equation 7.17 can be easily integrated to give

$$\Theta = C_1 e^{-\frac{z\alpha}{2b^2\nu_b}} \quad (7.19)$$

where  $C_1$  is a constant of integration. This expression for  $\Theta$  can be substituted back into Equation 7.15 giving

$$T = \theta \cdot C_1 e^{\left[\frac{z\alpha}{2b^2\nu_b}\right]} \quad (7.20)$$

The integral of Equation 7.18 can be obtained by first making the substitution

$$\frac{r}{b} = \Phi \quad \text{and} \quad \frac{R_0}{b} = \beta$$

to give

$$\frac{1}{b^2} \frac{d^2\theta}{d\Phi^2} + \frac{1}{b^2\Phi} \frac{d\theta}{d\Phi} + \frac{1}{b^2} \left[ 1 - \left( \frac{\Phi}{\beta} \right)^2 \right] \theta = 0 \quad (7.21)$$

or

$$\frac{d^2\theta}{d\Phi^2} + \frac{1}{\Phi} \frac{d\theta}{d\Phi} + \left( 1 - \frac{\Phi^2}{\beta^2} \right) \theta = 0 \quad (7.22)$$

It is worthy to note that Bessel's differential equation replaces the term  $\Phi^2/\beta^2$  with  $\beta^2/\Phi^2$ . Equation 7.22 can be integrated to obtain

$$R(\Phi) = \sum_{n=0}^{\infty} B_{2n} \Phi^{2n} \quad (7.23)$$

where:

$$B_0 = 1 \quad B_2 = -\frac{1}{2^2} \quad B_{2n} = \frac{1}{2n^2} \left( \frac{1}{\beta^2} B_{2n-4} - B_{2n-2} \right)$$

Combining Equations 7.20 and 7.23 and introducing the boundary conditions  $T = T_0$  at  $z = 0$  and  $T = T_s$  at  $r = R_0$  gives the final solution

$$\frac{T_s - T}{T_s - T_0} = \sum_{n=0}^{\infty} B_n C_n e^{\beta_n^2 (z/R_0) / Re \cdot Pr} \quad (7.24)$$

Tabulated data is available for the first 10 terms in the series for the eigenvalue  $\beta_n$  and other critical constants for the flow in a round tube<sup>47</sup>. Upon combining Equations 7.13 and 7.24, the bulk temperature of the fluid at any axial position can be found by

$$T_b = \frac{1}{\pi R_0^2 V_b C_p \rho} \int_{r=0}^{r=R_0} (\rho C_p T V_z) (2\pi r) dr = \frac{2}{R_0^2 V_b} \int_{r=0}^{r=R_0} T V_z r dr \quad (7.25)$$

## 7.6 Model C - Impenetrable Plasma with No-slip Boundary Conditions

The third model evaluated considers the plasma to be a completely impenetrable medium. As illustrated in Figure 7.4, the flow assumes a parabolic velocity profile around the annulus due to no slip conditions. The assumptions stated in Model A also hold for this analysis.

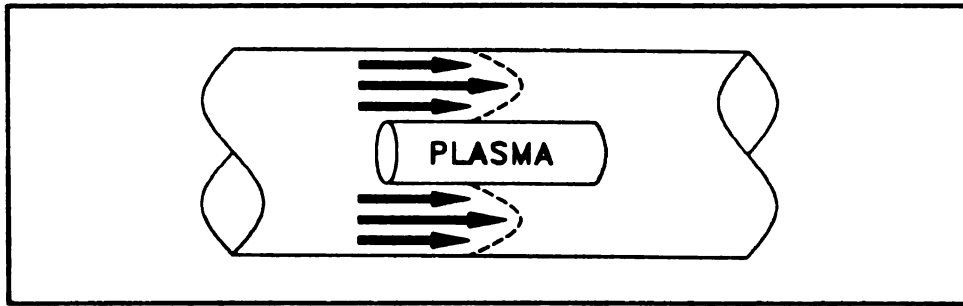


**Figure 7.4** Parabolic Velocity Profile around Annulus, No-slip Conditions at  $R_0$  and  $R_i$

The simplified equation of motion becomes

$$\frac{dP}{dz} = \mu \left[ \frac{1}{r} \frac{\partial}{\partial r} \left( r \frac{\partial v_z}{\partial r} \right) \right] \quad (7.26)$$

Integrating Equation 7.26 twice and applying the boundary conditions

$$v_z = 0 \quad \text{at} \quad \begin{array}{l} r = R_0 \text{ (quartz tube radius)} \\ r = R_i \text{ (plasma radius)} \end{array}$$

gives the velocity profile around the annulus

$$v_z = \frac{1}{4\mu} \frac{dP}{dz} \left[ (r^2 - R_0^2) + \left( \frac{R_0^2 - R_i^2}{\ln \frac{R_0}{R_i}} \right) \ln \frac{R_0}{r} \right] \quad (7.27)$$

If the flow of neutral species into the plasma were considered negligible, then the velocity profile given in Equation 7.27 would hold rigorously and the small pressure drop could be estimated under varying conditions. The pressure drop was evaluated based on the definition of flow rate or

$$\begin{aligned}
Q &= \langle V_s \rangle \cdot A_{\text{annulus}} \\
&= 2\pi \int_{R_i}^{R_o} r V_s(r) dr \\
&= 2\pi \int_{R_i}^{R_o} r \left[ \frac{1}{4\mu} \frac{dP}{dz} (r^2 - R_o^2) + \left( \frac{R_o^2 - R_i^2}{\ln \frac{R_o}{R_i}} \right) \ln \frac{R_o}{r} \right] dr
\end{aligned} \tag{7.28}$$

which reduces to

$$Q = \frac{\pi}{2\mu} \frac{dP}{dz} \left[ \int_{R_i}^{R_o} (r^3 - R_o^2 r) dr + \left( \frac{R_o^2 - R_i^2}{\ln \frac{R_o}{R_i}} \right) \int_{R_i}^{R_o} (r \ln R_o - r \ln r) dr \right] \tag{7.29}$$

Integrating Equation 7.29 yields

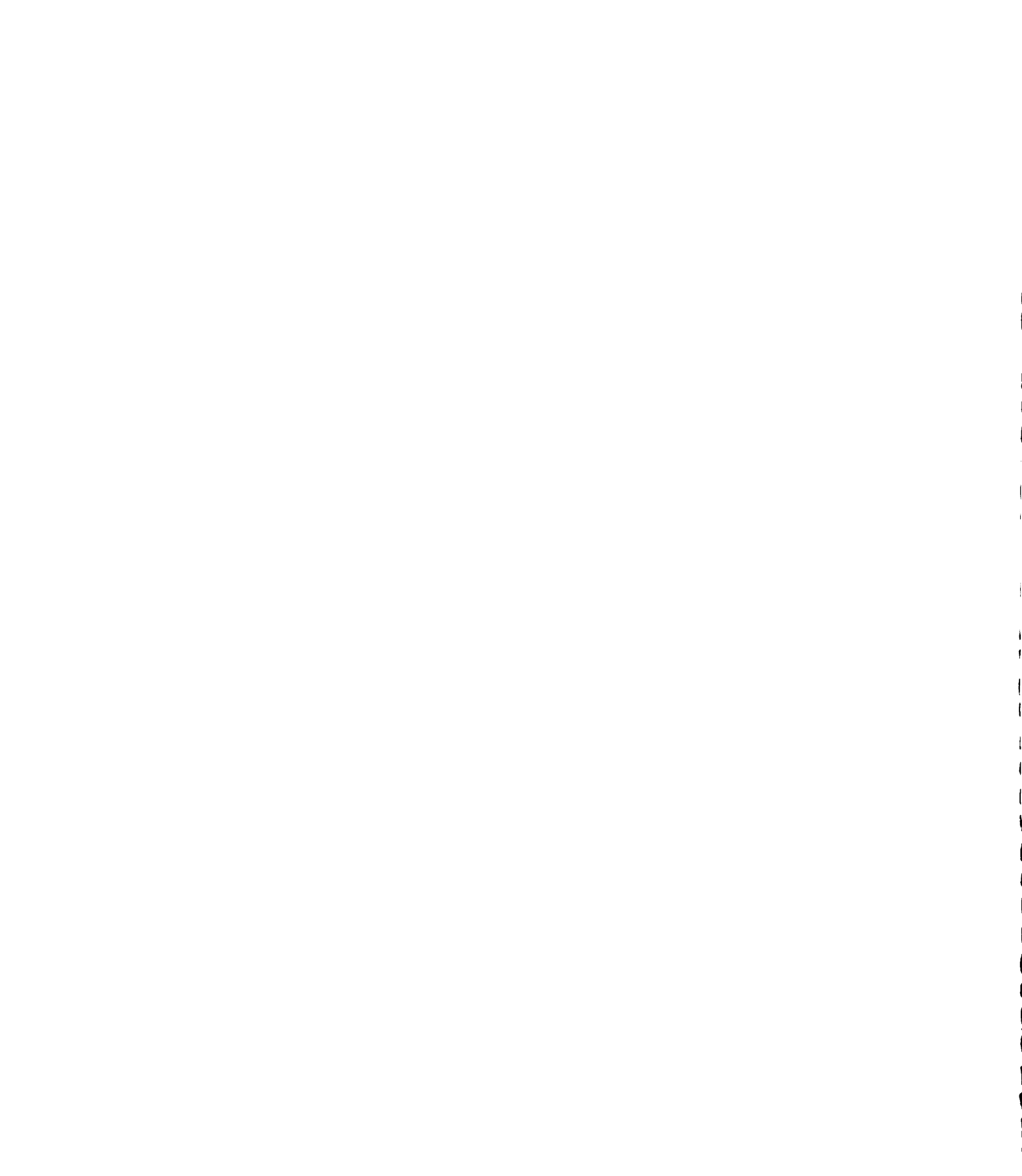
$$Q = \frac{\pi}{8\mu} (R_o^2 - R_i^2) \frac{dP}{dz} \left[ \frac{R_o^2 - R_i^2}{2 \ln \frac{R_o}{R_i}} \left( \ln R_i + \frac{1}{2} \right) - (R_o^2 + R_i^2) \right] \tag{7.30}$$

and the final expression for the pressure drop over the plasma discharge becomes

$$\Delta P = \frac{8\mu Q \Delta z}{\pi (R_o^2 - R_i^2)} \left[ \left( \frac{R_o^2 - R_i^2}{2 \ln \frac{R_o}{R_i}} \right) \left( \ln R_i + \frac{1}{2} \right) - (R_o^2 + R_i^2) \right]^{-1} \tag{7.31}$$

The influences of pressure on the radius of the plasma was experimentally measured and described in Chapter 4. Incorporating this data into the final expression of Equations 7.31 resulted in the distribution found in Figure 7.5.

The temperature distribution around the plasma discharge, assuming cylindrical geometry and uniformly heated surfaces, has been treated by Jakob and Rees<sup>49</sup>. The following differential equation was derived



### Theoretical Pressure Drop Over Plasma Impenetratable Plasma Model (C)

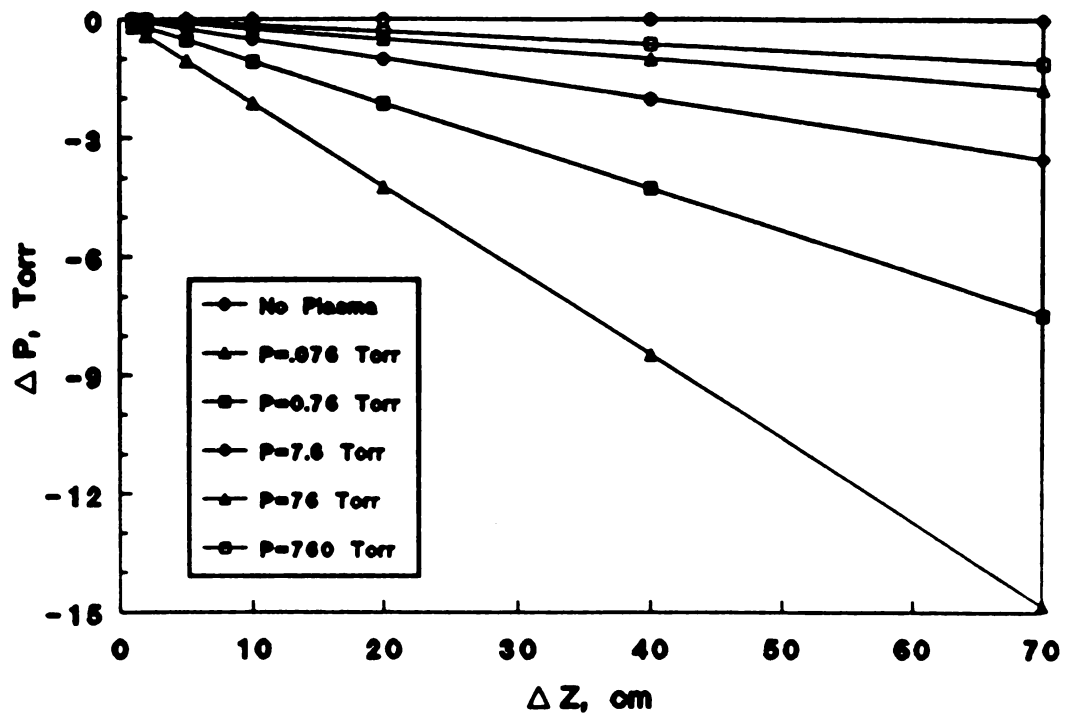


Figure 7.5 Theoretical Pressure Drop for Model C

$$\frac{\partial}{\partial r} \left( r \frac{\partial T}{\partial r} \right) = \frac{2Qr}{\pi \alpha M} \left[ R_i^2 - r^2 + B \ln \frac{r}{R_i} \right] \frac{\partial T}{\partial z} - r \frac{\partial^2 T}{\partial z^2} \quad (7.32)$$

where:

$$\begin{aligned} Q &= \text{rate of volume flow} \\ M &= (R_0^2 - R_i^2) (R_0^2 + R_i^2 - B) \\ B &= \text{logarithmic mean radius} \\ &= \left( \frac{R_0^2 - R_i^2}{\ln \frac{R_0}{R_i}} \right) \end{aligned}$$

Assuming the temperature change per unit length is constant at sufficiently great distance,  $z$ , from the beginning of the plasma, the following boundary conditions can be applied

$$\frac{\partial T}{\partial z} = \text{Constant} \quad \text{and} \quad \frac{\partial^2 T}{\partial z^2} = 0$$

Equation 7.32 can be reduced to the following conduction expression

$$\frac{d}{dr} \left( r \frac{dT}{dr} \right) = \frac{2QC}{\pi \alpha M} \left[ R_i^2 r - r^3 + Br \ln \frac{r}{R_i} \right] \quad (7.33)$$

Jakob has transformed this one-dimensional, second-order ordinary differential equation into the following<sup>48</sup>

$$\frac{T_0 - T_1}{\Delta T} = \frac{Q}{2\pi \alpha L} \chi \quad (7.34)$$

where:

$$\chi = \frac{1}{(1-y^2)(1+y^2-z)} \left\{ (1-y^2) \left[ \frac{3(1+y^2)}{4} - z \right] + y^2 \ln y (y^2-z) + \ln y [1-y^2(y^2-z) - z] P_1 \right\}$$

and

$$y = \frac{R_i}{R_o}$$

$$z = \frac{(y^2-1)}{\ln y}$$

$$P_1 = \frac{Q_i}{Q_i+Q_o}$$

$$Q_i = h_{i0} \Delta z \cdot 2\pi R_i (T_i - T_o)$$

$$Q_o = h_{o1} \Delta z \cdot 2\pi R_o (T_o - T_i)$$

The temperature change,  $\Delta T$ , is over the plasma length,  $l$ . The quantities  $q_i$  and  $q_o$  denote the rate of heat out of the plasma and the rate of heat into the quartz containment, respectively. Solutions of Equation 7.34 can be obtained numerically using calorimetry data obtained experimentally once the individual heat transfer coefficients have been found. The individual heat transfer coefficient for the plasma,  $h_{i0}$ , can be found through tabulated data obtained by Lick and Emmons<sup>18</sup>.

## 7.7 Model D - Impenetrable Plasma with Slip Conditions Around the Plasma

The final model evaluated considers an impenetrable plasma region but assumes slip along the plasma/flowing gas interface. This is a more reasonable approximation since friction losses arising along a two-fluid interface would be



negligible compared to those along a fluid/solid interface. The modeled region is illustrated in Figure 7.6.

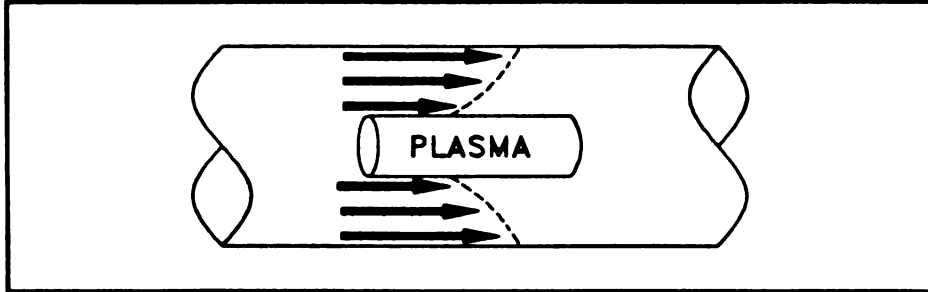


**Figure 7.6** No-slip along Containment Walls, Slip along Plasma

Incorporating the following boundary conditions

$$\begin{aligned} V_z &= 0 & \text{at} & \quad r = R_0 \text{ (quartz tube radius)} \\ \frac{dV_z}{dr} &= 0 & \text{at} & \quad r = R_i \text{ (plasma radius)} \end{aligned}$$

into Equation 7.26 and integrating twice gives the velocity profile

$$V_z = \frac{1}{4\mu} \frac{dP}{dz} \left[ r^2 - R_0^2 + 2R_i^2 \ln\left(\frac{R_0}{r}\right) \right] \quad (7.35)$$

The theoretical pressure drop was determined for this model to determine if the slip/no-slip assumptions made in Models C and D would significantly alter the pressure drop. Following the derivation outlined in Equations 7.28 - 7.31, the  $\Delta P$  was computed for this velocity profile to be

$$\Delta P = \frac{8\mu Q \Delta z}{\pi (R_0^2 - R_i^2)} \left[ R_0^2 - 4R_i^2 \ln\left(\frac{R_0}{R_0 - R_i}\right) - R_i^2 \right]^{-1} \quad (7.36)$$

The results of Equation 7.36, illustrated in Figure 7.7, closely resemble the distribution of those obtained for Model C. However, the significance of

### Theoretical Pressure Drop Over Plasma Impenetratable Plasma Model (D)

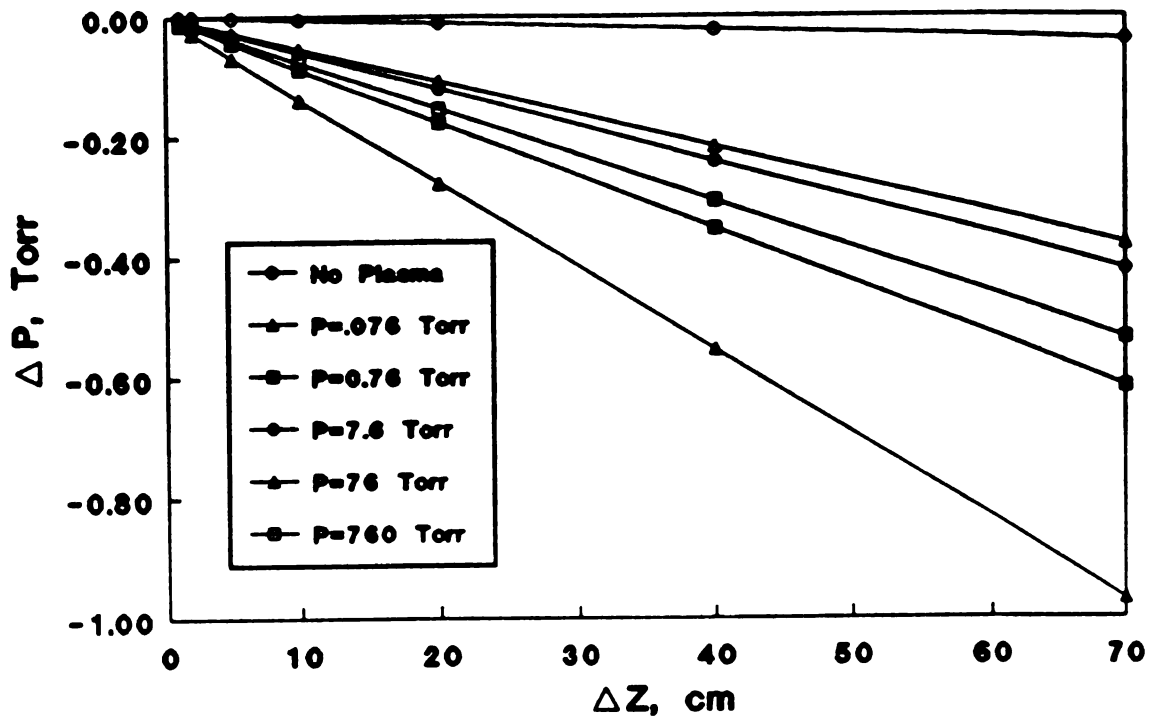


Figure 7.7 Theoretical Pressure Drop for Model D

pressure drop with distance has decreased by an order of magnitude for Model D due to the reduced friction losses associated with slip conditions.

A comparison of the  $\Delta P$ 's for Models C and D at various pressures, using identical parameters, is illustrated in Figure 7.8. The maximum difference between the two models occurs as the pressure approaches 0, which is where the plasma radius approaches the quartz tube radius. The order of magnitude difference is estimated to be beyond the experimental error in measuring the pressure drop so these two approximations can be regarded as virtually identical. Consequently, either models can be used to predict the amount of flowing neutral species that penetrate the plasma region. The temperature distribution for Model D can be derived from the same equations used for Model C.

## 7.8 Summary

The foregoing discussion has presented the development of several models that can be used to describe the velocity and temperature distributions around and downstream of the plasma. The assumptions used were initially oversimplified in order to quantitatively grasp the physics of the problem and to provide a foundation of models to build upon.

It can be concluded that the most realistic representation of the flowing gas around the plasma must consist of a combination of models; one model to



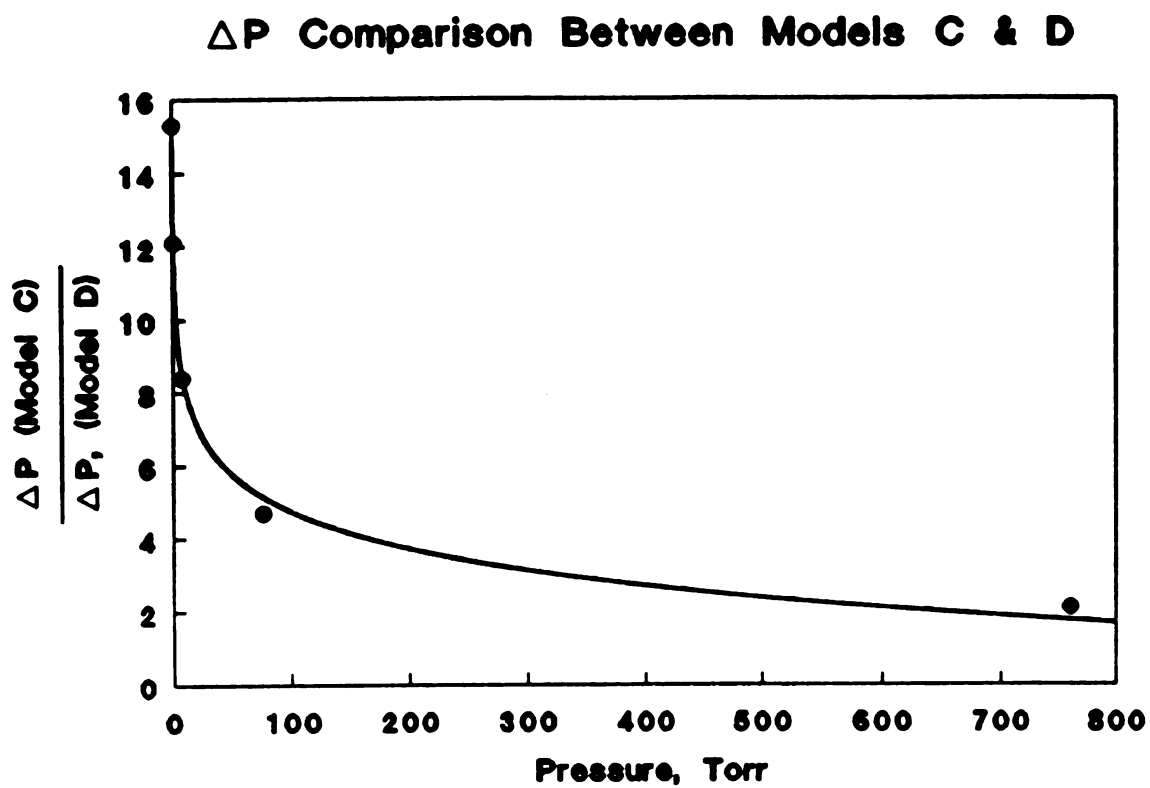


**Figure 7.8 Comparison of  $\Delta P$  Obtained for Models C and D**



describe the distributions immediately around the plasma and another to describe the distributions downstream. The final modeled region of the plasma is illustrated in Figure 7.9 below.

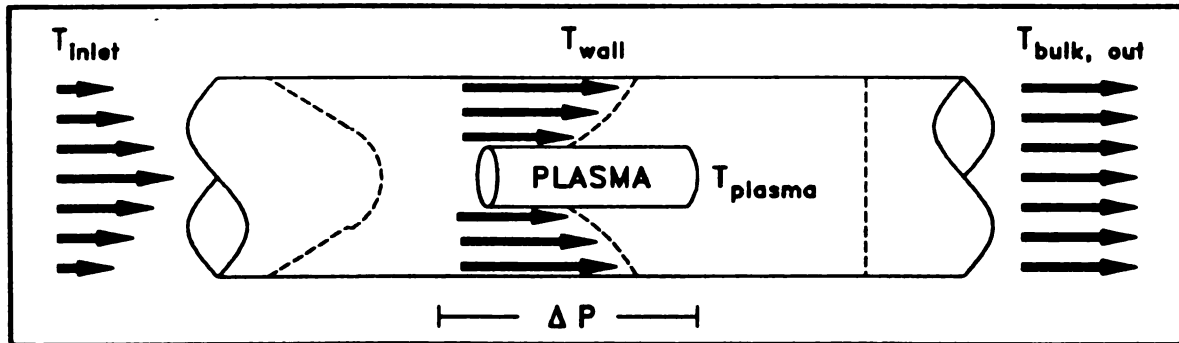


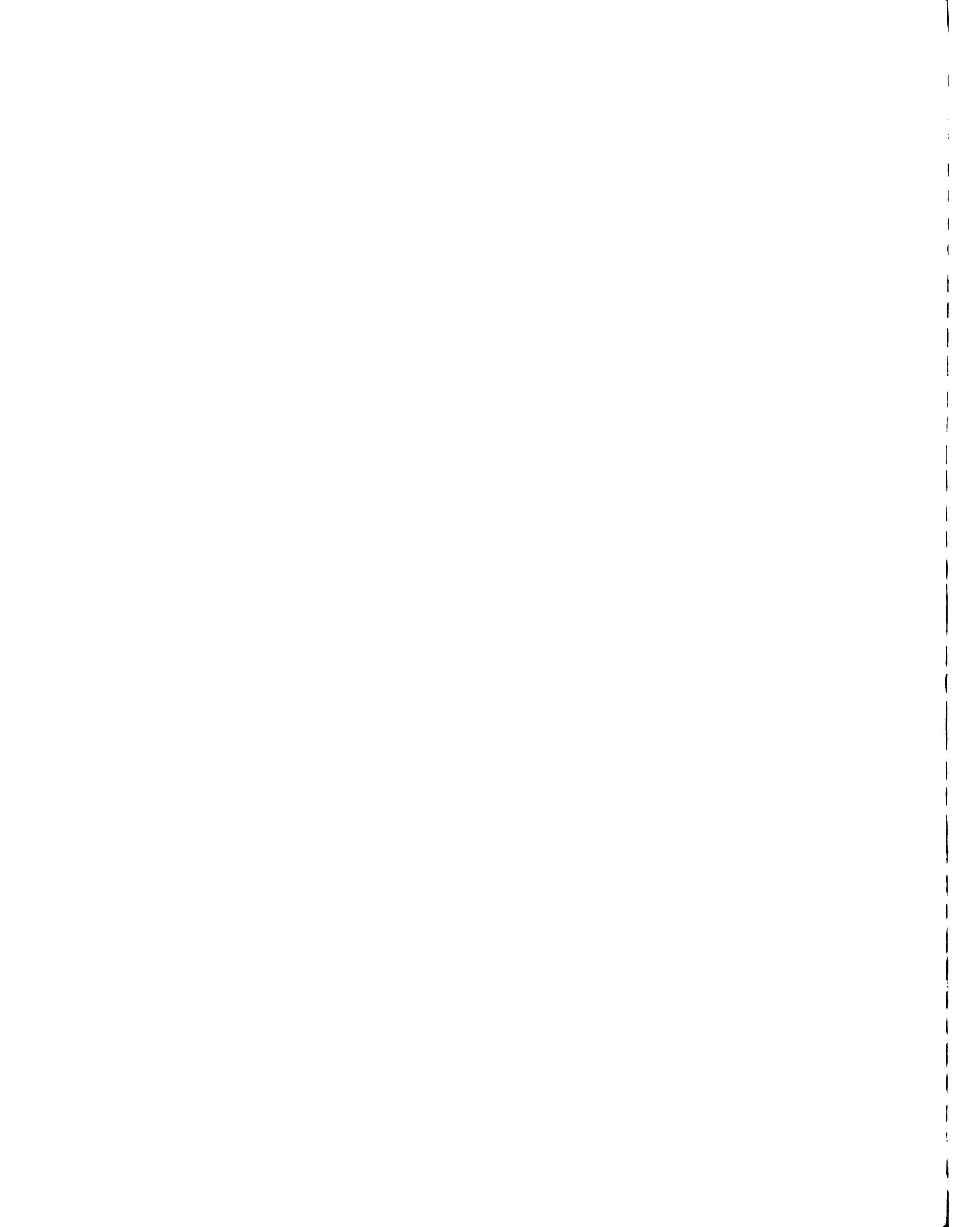
**Figure 7.9 Final Modeled Region**

Since Model D best describes the gas around the plasma, it would be beneficial to incorporate its solutions into Model B in order to describe the distributions downstream. This generates a complicated analysis, but one which could be numerically solved using finite elements in a supercomputing environment. It should be noted that these models exclude the effects of radiation and, more importantly, the diffusional effects of species out of the plasma. These two effects, which have been evaluated by previous researchers<sup>18</sup>, will be incorporated into the model at a later date.

The equations used to estimate the pressure drop over plasmas of varying dimensions (Equations 7.31 and 7.36) will play an important role in understanding the gas/plasma interactions. This theoretical pressure drop can be compared to the experimental pressure drops in order to better assess the degree to which the gas permeates the plasma surface. Improved models can



then be developed to describe the diffusion of species along the interface. The same procedure can be followed to experimentally evaluate the temperature distributions downstream of the plasma using thermocouple probes positioned at various radial and axial points. These temperature profiles or mixing cup temperatures can be used to evaluate nozzle performance and optimize the proximity of the plasma in relation to the expansion placement.



## CHAPTER 8

---

### *Summary and Conclusions*

The microwave electrothermal thruster has been demonstrated to be a viable substitute over systems involving electrodes and this work has contributed to its development and realization. The diagnostic techniques used in this investigation have provided significant insight towards the macroscopic influences a microwave generated plasma has on its surroundings and vice versa. This data is critical for the design and optimization of an efficient thruster system.

The effects of various gases, mixture ratios, gas flow rates, pressure, discharge power, and containment geometry on the plasma size, energy absorption, and temperature has been evaluated in order to better assess these macroscopic properties. The phenomenon occurring within the plasma has also been better explained through these investigations, though much less quantitatively than the macroscopic phenomenon. The physical and theoretical effects that the above parameters have on the atomic processes, interactions, and reactions have provided useful hypotheses on plasma formation and



sustainment. These effects have also better identified the dominating interactions that occur within the plasma and how these interactions influence plasma shape, size, energy absorption, and temperature.

The experimental configuration has been significantly modified to accommodate these diagnostics by the most accurate and efficient means, which includes computer-aided data acquisition and control techniques. The configuration also possesses the flexibility for future alterations, which includes increased power capacity, additional cooling, improved temperature measurements, swirling flows, and cavity maintenance.

The analysis of plasma dimensions and quality has been conducted on individual gases and their mixtures to better understand the transport mechanisms and trends with parameter changes. Mixtures were emphasized in this investigation in order to better understand the effects of contamination and to determine relationships between monatomic and diatomic molecular interaction. The detailed microscopic explanation of these results can be found in Chapter 4, but in general it was observed that

- helium plasmas exhibit a "dumbbell" shape while nitrogen and argon plasmas exhibit an ellipsoidal shape
- argon plasmas are transformed into a mass of elongated filaments at pressures in excess of 100 Torr
- plasma volume decreased exponentially with increasing pressure
- helium plasma volume decreased with decreasing flow rate at low power

levels but decreased with increasing flow rate at high power levels due to "saturation"

- nitrogen plasma volume decreased with decreasing flow rates
- plasma volume decreased with decreasing power
- maximum volumes for mixtures were obtained at the pure component extremes

Energy distribution investigations provided information on general trends with individual gases and their mixtures at various conditions. They also demonstrated the importance of a well maintained cavity and containment system. It was observed that the energy losses due to convection and radiation could be significantly reduced if the cavity and containment walls were carefully cleaned, thus eliminating the absorption of energy by foreign molecules. Efficiencies in excess of 80% were obtained under contamination free conditions. Other trends observed in energy absorption include

- pure nitrogen continues to absorb energy with increasing pressure due to additional energy modes
- pure helium fails to absorb energy with increasing pressure due to the effects of "saturation"
- mixtures of helium and nitrogen absorb the greatest amounts of energy at their pure component extremes
- pure nitrogen continues to absorb energy with increasing flow rates

- pure helium fails to absorb energy with increasing flow rates
- variations in power input contributes insignificantly to energy absorption

The presence of local thermal equilibrium within the plasma was evaluated spectroscopically using several line-intensity conversion methods whose dependence on LTE varies. The high standard deviations generated using the Two-line Ratio method, which is strongly dependent on LTE, concluded that the plasma under these experimental conditions, summarized in Table 8.1, is not in LTE.

**Table 8.1 Experimental Conditions used to Evaluate LTE**

Gas Flow Rate	> 100 sccm
Pressure	> 100 Torr
Net Power Input	< 300 Watts
Containment Geometry	= cylindrical
Containment Diameter	= 31 mm
Resonance Mode	= TM <sub>012</sub>
Coolant	= Air
Coolant Rate	= 2 scfm
Gases	= He, Ar, N <sub>2</sub>

A possible explanation for the non-LTE existence lies in the particle relaxation times exceeding the particle residence times or the lack of a microreversibility between the collisional processes.

It was determined through the various spectroscopic methodologies that

the atomic Boltzmann plot method is most suited for the estimation of electronic temperatures, which includes the energy of the bound electrons. Conversely, the Single-line method provided approximations for the electron temperatures, which includes the energy associated with the free electrons. Since the electrons are the driving force of the plasma it is reasonable to expect their temperatures to be higher than the other species. The large deviations between the electronic and electron temperatures also confirm the absence of LTE. These temperature measurements were incorporated into the Saha-Eggert equations to estimate the degree of ionization under these experimental conditions. Other observations made through these experiments with helium plasmas include

- electronic and electron temperatures increase with increasing pressure but tend to level out at high pressures due to "saturation"
- electronic and electron temperatures decrease sharply with increasing gas flow rates (similar trends observed with argon)
- the degree of ionization decreases sharply with gas flow rate

Several models were formulated to describe the macroscopic influences the plasma has on a flowing gas, primarily velocity and temperature distributions and bulk temperature. The models are based on experimental data that consists of plasma dimension, plasma temperature, plasma heat transfer coefficients, gas flow rate, and containment geometry. It was concluded that



the combination of two models, one to describe the distributions immediately around the plasma and another to describe the distributions downstream, would most accurately represent the actual process. These models, however, make no attempt to describe the effects of species diffusion on the velocity and temperature distributions.

The pressure drop was also estimated from these models, assuming an impenetrable plasma. This theoretical pressure drop can be compared to experimental observations to determine the degree of neutral particle flow into the plasma. The temperature distributions downstream of the plasma can also be compared to experimental observations in order to better assess the validity of the modeling assumptions.

Significant progress has been made over the past decade in developing the fundamentals of microwave generated plasma behavior as applied towards spacecraft propulsion. Advanced research methods must now be employed to fill the gap between theory and experimental observation and to establish the validity of major, and often dubious, assumptions. It is imperative that these macroscopic investigations be coupled with the microscopic theory obtained through this and previous research in order to establish a complete picture of the overall plasma process and its role in spacecraft propulsion.

## CHAPTER 9

---

### *Recommendations for Future Research*

**"All things I thought I knew; but now confess  
the more I know I know, I know the less"**

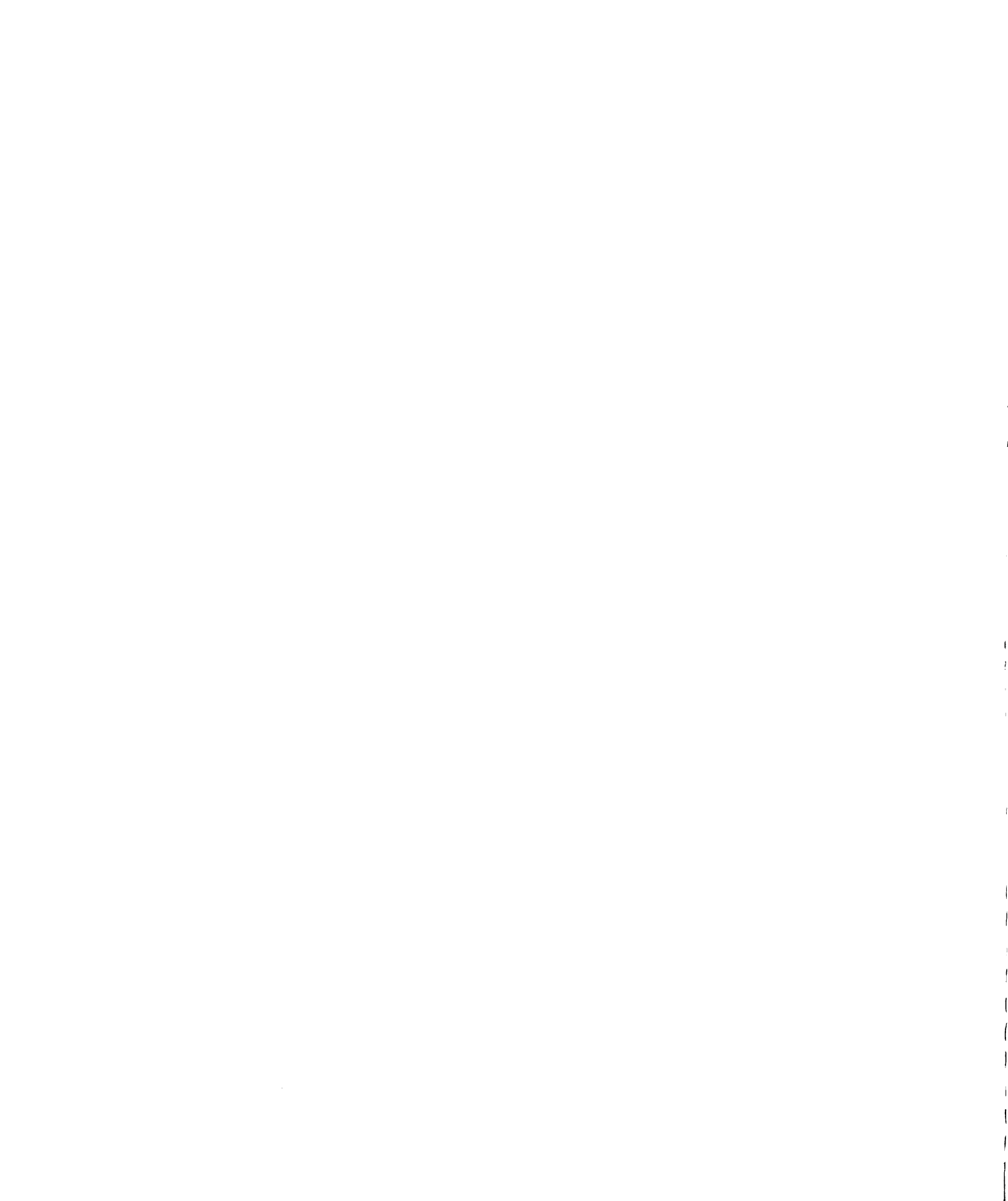
**[Owen - *Works*, Bk. VI]**

The old adage seems to have provided a central theme for this entire humbling investigation since every answered question brought about two more questions. Though it would be impossible to address every recommendation in detail, it would be beneficial towards the continued progression of the project to follow-up on a select few. Listed below are a few recommendations that should be considered for future research.

1. It is highly recommended that future experiments be conducted with pressures approaching 1 mTorr or less. This can only be accomplished by incorporating a diffusion/roughing pump system into the experimental apparatus. As discussed in Chapters 2 and 6, the degree of ionization becomes significantly greater at lower pressures. Consequently, low-

pressure experiments would produce much higher concentrations of singly-, possibly even doubly-, ionized species that could be spectroscopically analyzed with greater accuracy. As illustrated in Figure 2.5, higher degrees of ionization can be achieved with lower pressures at any given plasma temperature. These concentrations could also be achieved by higher power input levels, but this modification would be at the expense of higher plasma temperatures that could potentially melt the quartz containment. This low-pressure environment is also a criteria for LIF-based experiments.

2. Confirm the theoretical radial and axial temperature distributions downstream of the plasma using experimental methods. The modified collar system will allow the various placement of up to four subminiature thermocouple probe assemblies to measure these profiles. The collar system has been fabricated and the probes have been purchased to conduct these experiments, however it is suggested that the current data acquisition system be expanded to include temperature measurements.
3. Incorporate sensitive pressure transducers around the containment system to accurately measure the pressure drop over the plasma region. This experimental data can be compared to the theoretical pressure to



**measure the degree of neutral particle penetration into the plasma.**

- 4. Completely integrating the thermocouple wire and probes to the computer DAS would allow the exact time needed to reach thermal equilibrium within the containment to be measured.**
  
- 5. Generate and analyze the effects of swirling flows on plasma formation and sustainment. This addition of an angular component would also provide another means of measuring whether the gas flow penetrates or by-passes the plasma region. The modified collars contain radial inlet ports to provide the "helix" formation and point velocity measurements could be conducted with the aid of laser doppler velocimetry.**
  
- 6. Develop FORTRAN code to obtain solutions for the combination of models outline in Chapter 7. These models should be appended to models previously formulated to describe the microscopic processes and transport phenomenon within the plasma region. This final model would account for the transfer of individual species to and from the plasma region. This model would provide the most realistic description of the entire plasma process used to predict nozzle performance.**



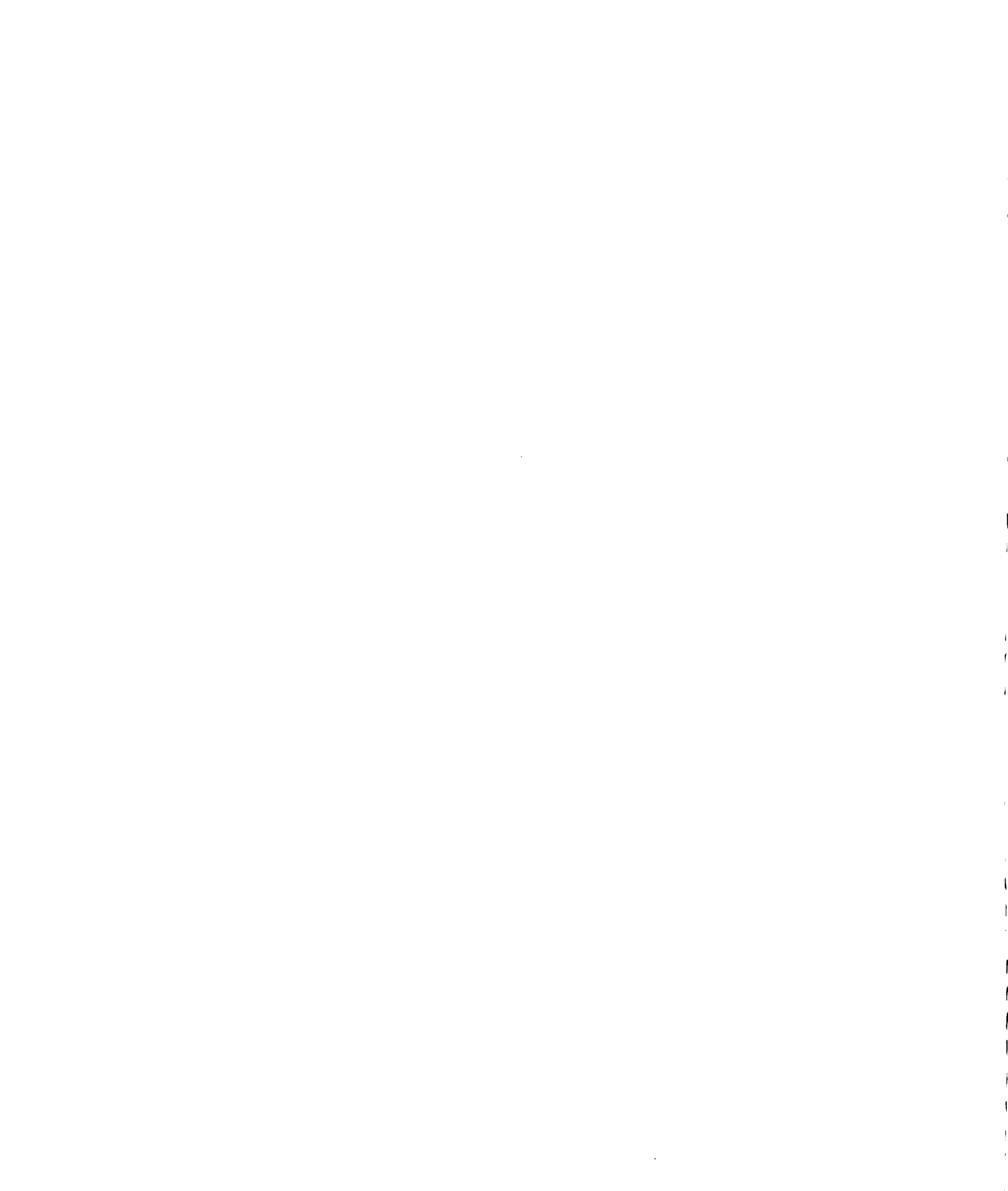
7. Relocate the current experimental system to within close proximity of the tunable dye laser and begin LIF experiments.
8. Incorporate a nozzle assembly onto the experimental apparatus to measure nozzle performance for varying plasma locations and conditions.
9. Address the nonequilibrium status of the plasma including the responsible element(s) and reasonable methods to place the plasma in LTE.
10. A final recommendation would be to address whether these low pressure diagnostics would apply to actual thruster performance operating at pressures in excess of 5 atmospheres (ie. Do the mechanisms change?).

## REFERENCES

1. Kunkel, Wulf B., Plasma Physics In Theory And Application, McGraw-Hill Book Company, New York, [1966].
2. National Research Council Panel on the Physics of Plasmas and Fluids, Plasmas and Fluids, Washington D.C., National Academy Press, [1986].
3. Hellund, E.J., The Plasma State, N.Y., Reinhold Publishing Corp., [1961].
4. Carr, M.B., "Life Support Systems", Military Posture - FY 1985, Joint Chiefs of Staff, [1985].
5. Welle, R.P., J.E. Pollard, S.W. Janson, M.W. Crofton, and R.B. Cohen, "One Kilowatt Hydrogen and Helium Arcjet Performance", The Aerospace Corporation, AIAA/SAE/ASME/ASEE 27<sup>th</sup> Joint Propulsion Conference, [1991].
6. Johnston, J.W., I.P. Shkarofsky, M.P. Bachynski, The Particle Kinetics Of Plasma, Addison-Wesley Publishing Co., Reading, MA, [1966].
7. Bittencourt, J.A., Fundamentals Of Plasma Physics, Pergamon Press, New York, [1986].
8. Lochte-Holtgreven, W., Plasma Diagnostics, North-Holland Pub. Co., Amsterdam, [1968].
9. Delcroix, J.L., Plasma Physics, vol. 1, John Wiley & Sons, Inc., New York, [1965].
10. Drawin, H.W., P. Felenbok, Data For Plasmas In Local Thermodynamic Equilibrium, Gauthier-Villars, Paris, [1965].
11. Wisniewski, S., R. Szymanik, and B. Staniszewski, Thermodynamics of Nonequilibrium Processes, D. Reidel Pub. Co., Hingham, MA, [1973].
12. Samaras, D.G., Theory Of Ion Flow Dynamics, Prentice-Hall, Inc.,

Englewood Cliffs, N.J., [1962].

13. Morin, T.J., "Theory and Modeling Of Nonequilibrium Electron-Molecule Interaction In Hydrogen," M.S. Thesis, Michigan State University, [1982].
14. Brown, S.C., Basic Data Of Plasma Physics, John Wiley & Sons, Inc., New York, [1959].
15. Sandler, S.I., Chemical and Engineering Thermodynamics, John Wiley and Sons, N.Y., [1989].
16. Micci, M., S. Venkateswaran, C. Merkle, "Analytical Modeling Of Microwave Absorption In A Flowing Gas", Pennsylvania State University, Dept. Of Mechanical Engineering, University Park, PA, [1990].
17. Zube, D.M., R.M. Myers, "Nonequilibrium in a Low Power Arcjet Nozzle", NASA Lewis Research Center, AIAA/SAE/ASME/ASEE 27<sup>th</sup> Joint Propulsion Conference, [1991].
18. Lick, W.J. and H. Emmons, Thermodynamic Properties Of Helium To 50,000 K, Harvard University Press, Cambridge, MA, [1962].
19. Haraburda, S.S., "Transport Properties of Plasmas in Microwave Electrothermal Thrusters," M.S. Thesis, Michigan State University, East Lansing, MI, [1990].
20. Panofsky, W.K.H. and M. Phillips, Classical Electricity and Magnetism, 2<sup>nd</sup> ed., Addison-Wesley Pub. Co., Reading, MA, 1962.
21. Balaam, P. and M. Micci, "The Stabilization and Spectroscopic Study of Microwave Generated Resonant Cavity Plasmas", Pennsylvania State University, Dept. Of Aerospace Engineering, University Park, PA, [1990].
22. Chapman, R., "Energy Distribution and Transfer In Flowing Hydrogen Microwave Plasmas," PhD. Thesis, Michigan State University, East Lansing, MI, [1986].
23. Haraburda, S., D. Dinkel, and M. Hawley, "Diagnostic Evaluations of Microwave Generated Helium and Nitrogen Plasma Mixtures", AIAA/DGLR/JSASS 21<sup>st</sup> International Electric Propulsion Conference, [1990].
24. Huddleston, R. and S. Leonard, Plasma Diagnostic Techniques,

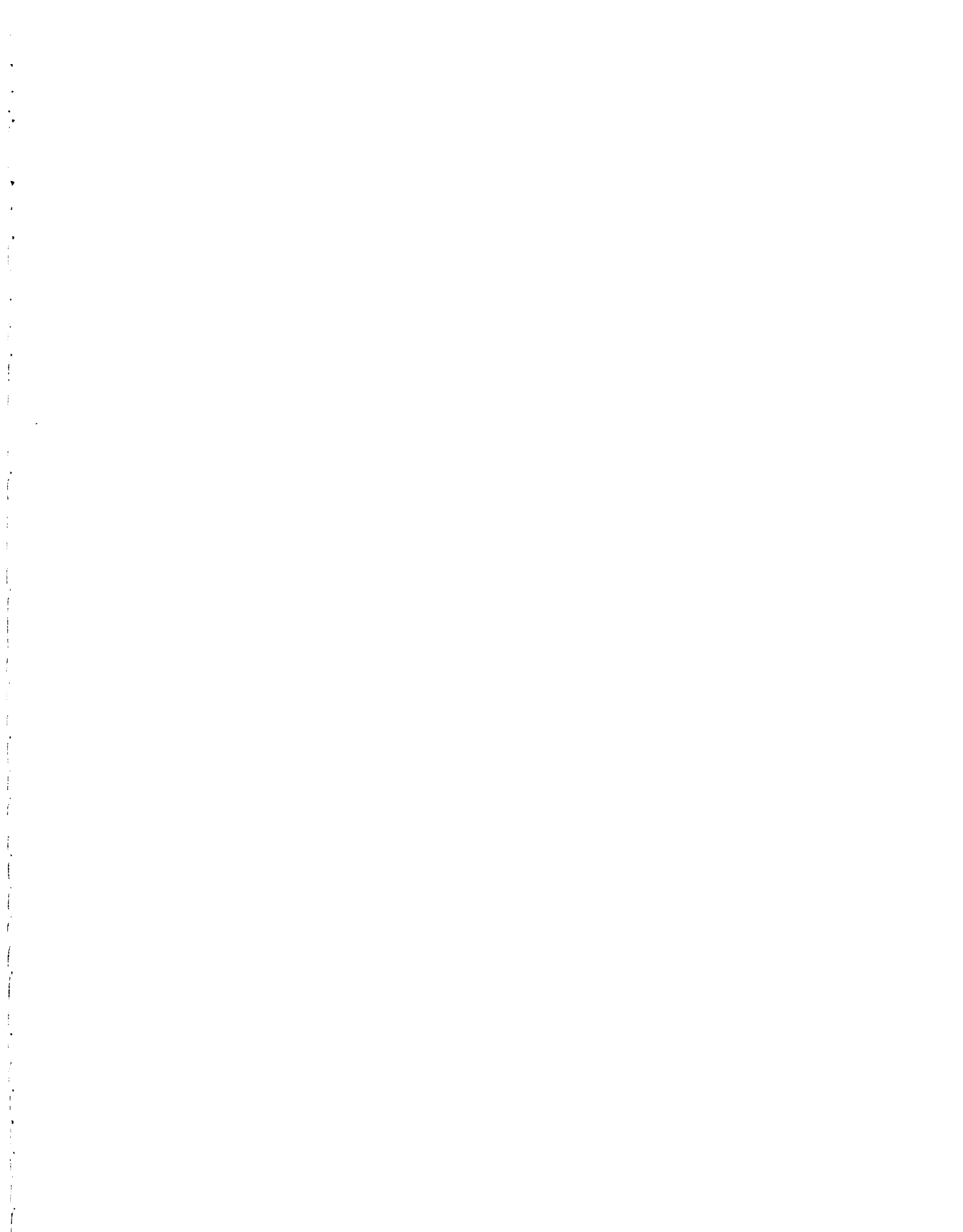


Academic Press, New York, [1965].

25. Hoekstra, C.F., "Investigations Of Energy Transport Properties In High Pressure Microwave Plasmas," M.S. Thesis, Michigan State University, East Lansing, MI, [1988].
26. Chapman, R., J. Filpus, T. Morin, R. Snellenberger, J. Asmussen, M. Hawley, and R. Kerber, "Microwave Plasma Generation of Hydrogen Atoms for Rocket Propulsion," Michigan State University, AIAA/JSASS/DGLR 15<sup>th</sup> Joint Propulsion Conference, [1982].
27. Chapman, R., M. Finzel, and M. Hawley, "Measurements of Energy Distribution and Wall Temperature in Flowing Hydrogen Microwave Plasma Systems," Michigan State University, [1985].
28. Wareck, J.S., "An Experimental Design and Model for the Dissociation of Oxygen in a Microwave Discharge," M.S. Thesis, Michigan State University, East Lansing, MI, [1980].
29. Handbook Of Chemistry And Physics, 69<sup>th</sup> Ed., CRC Press, [1988].
30. Dinkel, D.W., M.C. Hawley, and S.S. Haraburda, "Spectroscopic Investigations Of Microwave Generated Plasmas", 27<sup>th</sup> AIAA/SAE/ASME Joint Propulsion Conference, [1991].
31. Herzberg, G., Atomic Spectra and Atomic Structure, Prentice-Hall, Inc., New York, [1937].
32. Bird, R.B., W. Stewart, E. Lightfoot, Transport Phenomena, John Wiley & Sons, Inc., New York, [1960].
33. Tourin, R.H., Spectroscopic Gas Temperature Measurement, Elsevier Pub. Co., New York, [1966].
34. Penner, S.S., Quantitative Molecular Spectroscopy and Gas Emissivities, Addison-Wesley, Reading, MA., [1959].
35. Striganov, A.R., N.Sventitskii, Tables Of Spectral Lines Of Neutral And Ionized Atoms, IFI/Plenum, Washington D.C., [1968].
36. Herzberg, G., Spectra Of Diatomic Molecules, D. Van Nostrand Co., Inc., New York, [1950].
37. Griem, H.R., Plasma Spectroscopy, McGraw-Hill Co., New York, [1964].



38. DiMauro, L., R.A. Gottscho, T.A. Miller, *Journal Of Applied Physics*, "Two-Photon Laser-Induced Fluorescence Monitoring of O Atoms in a Plasma Etching Environment", 57:7, [1984].
39. Hartog, E.A., H. Persing, R. Woods, "Laser-Induced Fluorescence Measurements of Transverse Ion Temperature in an Electron Cyclotron Resonance Plasma", Univ. Of Wisconsin-Madison, submitted to *Applied Physics Letters*, March, [1990].
40. d'Agostino, F. Cramarossa, S. De Benedictis, F. Fracassi, *Plasma Chemistry and Plasma Processing*, "Optical Emission Spectroscopy and Actinometry in CCl<sub>4</sub>-Cl<sub>2</sub> Radiofrequency Discharges", vol. 4, No. 3, [1984].
41. Eddy, T.L., A. Sedghinasab, *IEE Transactions On Plasma Science*, "The Type and Extent of Non-LTE in Argon Arcs at 0.1-10 Bar", vol. 16, No. 4, August, [1988].
42. Hopwood, J.A., "Macroscopic Properties of a Multipolar Electron Cyclotron Resonance Microwave-Cavity Plasma Source for Anisotropic Silicon Etching", PhD. Thesis, Michigan State University, East Lansing, MI, [1990].
43. Bennett, C.O., J.E. Myers, Momentum, Heat, and Mass Transfer, 3<sup>rd</sup> ed., McGraw-Hill, Inc., New York, [1982].
44. Snellenberger, R.W., "Hydrogen Atom Generation and Energy Balance - Literature Review, Modeling, and Experimental Apparatus Design", M.S Thesis, Michigan State University, East Lansing, MI, [1980].
45. Mertz, S.F., "A Kinetic Model For the Reactions Of CO and H<sub>2</sub> To CH<sub>4</sub> and C<sub>2</sub>H<sub>2</sub> In A Flow Microwave Plasma Reactor", M.S Thesis, Michigan State University, East Lansing, MI, [1975].
46. Graetz, L., *Ann. Phys., N.F.*, 18:79, [1883] and 25:737, [1885].
47. Sellars, J.R., M. Tribus, and J.S. Klein, *American Society Of Mechanical Engineers Transactions*, 78:441, [1956].
48. Jakob, M., Heat Transfer, vol. 1, John Wiley & Sons, New York, [1949].
49. Jakob, M. and K.A. Rees, *American Institute Of Chemical Engineers Transactions*, 37:619, [1941].



MICHIGAN STATE UNIV. LIBRARIES



31293015894656